Search for Supersymmetry in final states with multiple bottom quarks with the ATLAS detector

by

Meisam Ghasemi Bostanabad

B.Sc., University of Tehran, 2012

M.Sc., Sharif University of Technology, 2014

A Dissertation Submitted in Partial Fulfillment of the
Requirements for the Degree of

DOCTOR OF PHILOSOPHY

in the Department of Physics and Astronomy

University of Victoria

Search for Supersymmetry in final states with multiple bottom quarks with the ATLAS detector

by

Meisam Ghasemi Bostanabad

B.Sc., University of Tehran, 2012

M.Sc., Sharif University of Technology, 2014

Supervisory Committee

Dr. Justin Albert, Supervisor
(Department of Physics and Astronomy)

Dr. Richard Keeler, Member
(Department of Physics and Astronomy)

Dr. Michel Lefebvre, Member
(Department of Physics and Astronomy)

Dr. Heath Emerson, Outside Member
(Department of Mathematics and Statistics)

Abstract

The theoretical development of the Standard Model in the 1960s and 1970s has led to the discovery of its missing piece, the Higgs boson, at the ATLAS experiment (together with its sister experiment, CMS) at the Large Hadron Collider at CERN in 2012. In order to solve the problem of large quantum corrections to the leading expansion of the Higgs boson mass, additional symmetries need to be added to the Standard Model. A possible solution to this problem of Higgs mass quantum corrections is the theory of Supersymmetry, which includes partners to each Standard Model particle, such as gluinos, squarks, and the lightest supersymmetric particle. This dissertation describes a search for pair-produced gluinos, where each gluino decays via a top squark or a bottom squark to the lightest supersymmetric particle (a neutralino). Events which contain a large jet multiplicity in the final state (i.e. at least four jets of which at least three must be b-jets), and large amounts of missing transverse energy, are obtained for further studies. The dataset used for this search includes 139 fb^{-1} of integrated luminosity recorded by the ATLAS experiment between 2015 and 2018 at a center-of-mass energy $\sqrt{s} = 13$ TeV. No significant excess is observed in data above the Standard Model backgrounds, and gluino masses up to 2.3 TeV for both the Gtt and the Gbb models are excluded at a 95% confidence level. This dissertation also contains an overview of, and the author's work on, the data quality monitoring of the ATLAS liquid argon calorimeter during 2017 data taking.

Contents

List of Figures

List of Tables

Acknowledgement

During my PhD at the University of Victoria I have had opportunity to work with some brilliant and amazing people who inspired me to pursue my studies. my thanks and appreciation to all of them for being part of this journey and making this thesis possible.

First of all, I would like to express my deepest gratitude to my PhD supervisor, Dr. Justin Albert, for giving me the opportunity to do graduate program and providing invaluable guidance throughout this research; he has been supportive all the time and let me free to try different analysis groups. It was a great privilege and honour to work and study under his guidance! Special thanks to Prof. Michel Lefebvre to lead UVic ATLAS group and all the people who are part of this great working environment. I am particularly grateful to the post-docs in the group such as Emma Kuwertz, Manuela Venturi, Kenji Hamano, and Monica Trovatelli who have helped me and without their precious support it would not be possible to conduct this research. At UVic, my fellow graduate students: Tony Kwan, Ewan Hill, Alison Elliot, Kayla McLean, Danika MacDonell, Mathias Le dall, and Kossivi Denanyoh were helpful resources while going through scientific discussions and learning about the ATLAS detector. I owe a large debt of thanks to all of you.

The ATLAS multi-b analysis group was an amazing group with professional people and I am so proud to work with. Chiara Rizzi was very helpful source of opinions and helped me to gain independence in my study. I am particularly grateful to Maximilian Swiatlowski, who is an excellent coordinator and wisely lead the team in face of obstacles by keeping people motivated. I am extending my thanks to Giordon Stark and Louis-Guillaume Gagnon, who have always helped me with coding challenges and rapid-debugging support.

My eighteen months at CERN were great opportunity to connect with experts in Liquid Argon calorimeter and HistFitter teams. I would like to thank the people working in Liquid Argon calorimeter data quality group, and I am

especially grateful to Emma Kuwertz, Adriana Milic, and Pavol Strizenec for their patience and great ideas. I also would like to thank the HistFitter experts, particularly Jeanette Lorenz for her advice and quick response.

Finally, my sincere gratitude to my family for their continuous and unparalleled love, help and support. I am forever indebted to my Mom and Dad, for giving me the opportunities and experiences that have made me who I am. They selflessly encouraged me to explore different situations and seek my own destiny. I would not have even been able to start this work without the love of my family.

Declaration of Contributions

Analysis contributions

- Explored simplified SUSY signatures in the strong and electroweak multi-b analyses
- Editor for internal supporting documentation for full Run2 analysis paper
- Developed QCD estimation method and further validation processes
- Worked on pileup efficiencies and Z+jets validation regions
- Developed Higgs reconstruction technique for electroweak multi-b analysis
- Studied M_{T2} variable to discriminate electroweak signal and backgrounds
- Worked on theory systematics for $t\bar{t}$ and single-top backgrounds
- Did data and MC studies-plotting for signal models (both Gtt and Gbb)
- Provided analysis group dataset (ntuples) for both analyses
- Extended group statistical package for background likelihood fits

Detector and data quality contributions

- Developed LAr offline data quality monitoring framework to analyse conditionally and unconditionally masked channels
- Contributions to the development of the LAr online trigger tower noise killer
- Online shifts for the LAr and Tile calorimeter during 2017 data-taking

Chapter 1

Introduction

Particle physics encompasses the study of all subatomic particles, as well as their electromagnetic, weak, and strong fundamental interactions. The behaviour of these particles and interactions is well-described by the theory known as the Standard Model [1–3] that was formulated during the latter half of the 20th century. Many of the basic predictions of the Standard Model have been tested, and the discovery of the Higgs boson in 2012 was a great success for the theory. There are several open questions which are not addressed in the Standard Model, such as a number of parameters that appear to be unusually fine-tuned, and the microphysical natures of dark matter and dark energy. Supersymmetry encompasses a set of the most promising extensions of the Standard Model, which would help to resolve some of the open questions. In R-parity conserving Supersymmetry, partners of each Standard Model particle are predicted, and the lightest supersymmetric particle is a good candidate for dark matter. Chapter 2 introduces the theories of the Standard Model and Supersymmetry in particle physics.

To search for violations of the Standard Model, and for Supersymmetry, proton-proton (pp) collisions at high energies are produced at the Large Hadron Collider (LHC). The ATLAS and CMS detectors are the two general purpose experiments at the LHC at CERN[1] which collect and store data resulting from pp collisions. Chapter 3 describes the Large Hadron Collider complex and the ATLAS subdetectors. The ATLAS event recording strategy and Monte Carlo simulation for pp interactions are described in Chapter 4. After an event is recorded by the ATLAS trigger systems, all physics objects such as jets, leptons, and missing transverse energy need to be reconstructed to be used in

[1]The European Organization for Nuclear Research

the analysis (see Chapter 5). Chapter 6 presents the ATLAS search for pair-produced gluinos that decay to Standard Model top or bottom quarks, as well as neutralinos (which are the lightest supersymmetric particles in these models). Different sources of detector-related and theoretical systematics are discussed in Chapter 6. In this dissertation, ATLAS data collected between 2015 and 2018, at a center-of-mass energy 13 TeV, is used to probe for Supersymmetric models. Chapter 7 presents the results for a background-only fit, the exclusion limits for gluino-neutralino masses, and a comparison of similar signal models probed by the ATLAS and CMS collaborations. Finally, the concluding remarks about this multi-b analysis are discussed in Chapter 8.

Chapter 2

Standard Model (SM) and Supersymmetry

The Standard Model (SM) of particle physics is the theory that successfully predicts experimental results concerning fundamental particles and the interactions among them. It combines both quantum chromodynamics (the theory of the strong interaction) and the electroweak model (the unified theory of electromagnetic, weak, and Higgs interactions) to encompass all fundamental interactions, with the exception of gravity. Many particle physics experiments, both during the 30 years prior to the construction of, and at the Large Hadron Collider (LHC), have performed many precision measurements, and the results show good agreement with the predictions of the SM. This chapter presents an introduction to the SM of particle physics, as well as to a large class of extensions to the SM which are categorized under the heading of Supersymmetry (SUSY). Section 2.1 will provide a general overview of the SM. Some of the most famous puzzles of the SM and the theory of SUSY will be discussed in Sections 2.2 and 2.3.

2.1 The Standard Model

The SM is a gauge quantum field theory combining three different Lie groups into the product group $\mathrm{SU_C}(3) \times \mathrm{SU_L}(2) \times \mathrm{U_Y}(1)$: the Glashow-Weinberg-Salam theory of electroweak interactions (subsection 2.1.3), $\mathrm{SU_L}(2) \times \mathrm{U_Y}(1)$, and the theory of QCD $\mathrm{SU_C}(3)$ (subsection 2.1.4). The Standard Model has predicted the existence of several elementary particles, including a number of both fermions with half-integral spin and gauge bosons with integer spin. All of these

particles have been discovered by different experiments around the world, including the observation of the Higgs boson at LHC in 2012 [4–6], which resulted in the awarding of the 2013 Nobel Prize in Physics to Peter Higgs and François Englert for their development of the theory of the Higgs mechanism in 1964.

2.1.1 Standard Model particles

All particles in the SM can be categorised as fermions or bosons (see Fig. 2.1). **Fermions** are half-integer spin particles, thus they obey Fermi-Dirac statistics and comprise all non-dark matter in our universe [7]. They can be divided into leptons and quarks:

Leptons: includes electrons, muons and taus, as well as each of their associated neutrinos. Charged leptons can undergo electromagnetic as well as weak interactions; however neutral leptons (i.e., neutrinos) can only undergo weak interactions.

Quarks: includes six flavours of strongly interacting particles. The top quark is the heaviest one, and was discovered in the CDF and the D0 experiments at Fermilab [8, 9]. Quarks experience the electroweak force in addition to the strong force.

Both the leptons and the quarks have left-handed doublets ψ^L (which denotes left chirality) within which the two particles in each pair differ in electric charge. For example, charged leptons have an electric charge of -1 while the neutral leptons (neutrinos) have no electric charge. Right handed singlet states ψ^R exist for charged leptons and for all flavors of quarks; however they do not exist in the Standard Model for neutral leptons (i.e., there are no right-handed neutrinos). Another difference between leptons and quarks is the confinement property of the strong interaction. It is possible to observe free leptons, whereas quarks are bound into hadrons. Hadrons are formed by three quarks, called baryons, or one quark and one anti-quark called mesons.

Bosons are integer spin particles, so they obey Bose-Einstein statistics. All forces in the SM are carried by gauge bosons exchanged [10] between fundamental particles. For example, the electromagnetic interaction between two charged fermions is due to photon exchange. All types of SM interactions are listed in Table 2.1.

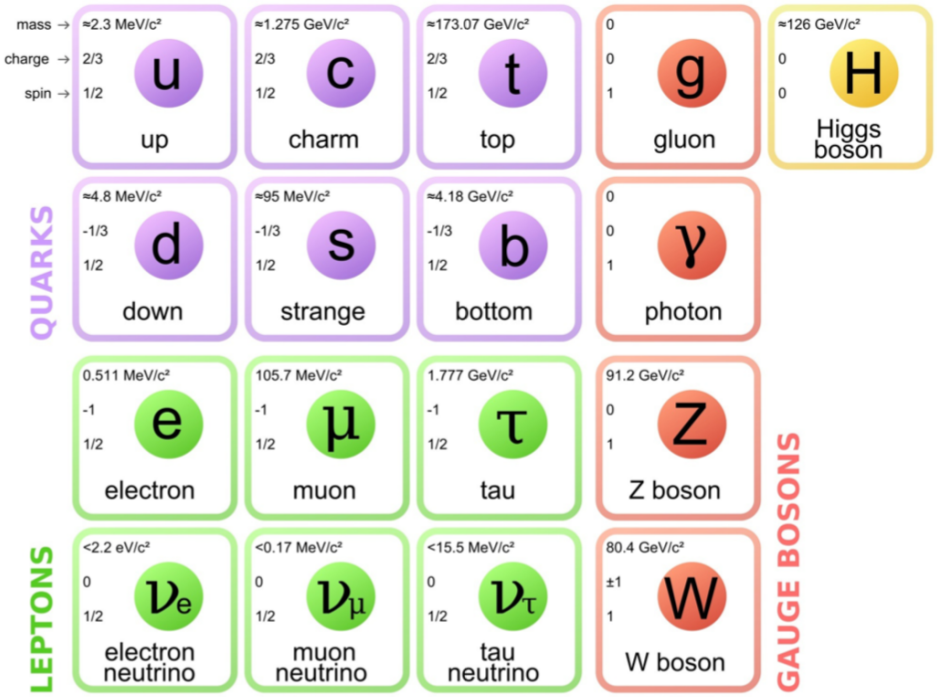

Figure 2.1: Particles of the Standard Model: Shown are twelve fermions (quarks and leptons) with spin $\frac{1}{2}$ and five bosons: photon, W/Z bosons, gluon and the Higgs boson. All fundamental bosons have spin 1 except the Higgs boson which has spin zero. Gravitational interactions and the gravitational force carrier (graviton) are not included in the Standard Model. The information included in this plot, such as the masses and charges, is provided by the Particle Data Group [11].

	Force			
Particles	Electromagnetic	Weak	Strong	Gravity
Leptons	✓	✓	✗	✓
Quarks	✓	✓	✓	✓
Gauge Bosons	Photons	W/Z	Gluons	Graviton (not yet discovered)

Table 2.1: All SM interactions (forces) among fundamental particles. The third row shows the gauge mediators for different interactions.

2.1.2 Gauge invariance

The SM is a renormalizable gauge field theory in which all the interactions are described by a Lagrangian. In natural units ($\hbar = c = 1$) the free Lagrangian for fermions and the massless electromagnetic vector A^μ are given by:

$$\mathcal{L}_{\text{fermion}}(x) = \bar{\psi}(x)(i\gamma^\mu\partial_\mu - m)\psi(x) \quad , \tag{2.1}$$

$$\mathcal{L}_{\text{vector}}(x) = -\frac{1}{4}F_{\mu\nu}F^{\mu\nu} \quad , \tag{2.2}$$

where $F^j_{\mu\nu} = \partial_\mu A^j_\nu - \partial_\nu A^j_\mu + g f^{jkl} A^k_\mu A^l_\nu$. In these equations ψ is the fermion field, γ are 4×4 Dirac matrices, ∂_μ is the four-vector derivative, and f_{ijk} is the structure constant of the group which is zero for Abelian groups like $U(1)$.

Both Lagrangians 2.1 and 2.2 need to be invariant under global and local gauge transformations [12,13]. Global transformations are described by a phase change of the fermion field:

$$\psi'(x) = e^{-ig\tau^j\theta^j}\psi(x) = U_\theta\psi(x) \quad , \tag{2.3}$$

where g is the coupling constant and τ^j is the group's generator (Pauli matrices in $SU(2)$ and Gell-Mann matrices in $SU(3)$) [14]. The Lagrangian 2.1 is invariant under this phase transformation when θ is constant everywhere in space-time. The local gauge transformations are defined with an x-dependent phase parameter $\theta^j(x)$ which varies locally from point-to-point in space-time:

$$\psi'(x) = e^{-ig\tau^j\theta^j(x)}\psi(x) = U_\theta(x)\psi(x) \quad . \tag{2.4}$$

The kinetic energy term in the fermion Lagrangian is not invariant under local transformations ($\partial_\mu\theta^j(x) \neq 0$). This implies adding a covariant derivative to the theory:

- The covariant derivative D_μ that must replace ∂_μ in Lagrangian 2.1:

$$D_\mu = \partial_\mu - ig\Sigma_j\tau^j A^j_\mu$$

- A^i_μ are massless vector gauge fields, and transform under local transformations as:

$$A^{j'}_\mu = A^j_\mu - \tfrac{1}{g}\partial_\mu\theta^j + f_{jkl}\theta^k A^l_\mu$$

By substituting both the covariant derivative and the transformed vector gauge field in 2.1 and 2.2, one can see that both Lagrangians are invariant under local transformations.

In summary, the SM is locally invariant under $\mathrm{SU_C}(3) \times \mathrm{SU_L}(2) \times \mathrm{U_Y}(1)$. The invariance under $\mathrm{SU_L}(2) \times \mathrm{U_Y}(1)$ leads to the theory of electroweak interactions, while the theory of strong interactions follows from invariance under $\mathrm{SU_C}(3)$. Based on Noether's theorem, a symmetry of the Lagrangian under a field transformation always implies a conservation law [15]. As the result, local invariance in the SM implies the conservation of weak hypercharge, isospin and colour charge.

2.1.3 Quantum electrodynamics

Quantum Electrodynamics (QED) [16] is a local gauge theory, meaning in this case that all Lagrangians in QED are invariant under continuous U(1) symmetry transformations. QED describes the interaction between electrically charged particles through the exchange of photons. QED Lagrangians are given by:

$$\begin{aligned} \mathcal{L}_{\mathrm{QED}} &= \mathcal{L}_{\mathrm{fermion}} + \mathcal{L}_{\mathrm{boson}} \\ \mathcal{L}_{\mathrm{fermion}} &= \bar{\psi}(x)(i\gamma^{\mu}\partial_{\mu} - m)\psi(x) + q\bar{\psi}\gamma^{\mu}A_{\mu}\psi \\ \mathcal{L}_{\mathrm{boson}} &= -\frac{1}{4}F_{\mu\nu}F^{\mu\nu}, \end{aligned} \tag{2.5}$$

where ψ is a Dirac spinor (fermion field), $\bar{\psi}$ is defined as $\bar{\psi} \equiv \psi^{\dagger}\gamma^{0}$, and A_{μ} is a vector field. The first and second terms in the fermion Lagrangian represent the kinetic energy and mass terms for spin $\frac{1}{2}$ particles. The last term describes the interactions between a fermion and a vector field. $\mathcal{L}_{\mathrm{boson}}$ in 2.5 describes the kinetic energy of the electromagnetic field (photon). The local gauge invariance leads to massless photons because the mass term $\frac{m^2}{2}A_{\mu}A^{\mu}$ violates the local gauge invariance unless $m = 0$.

An example of the simplest or *leading order* Feynman diagram of QED is shown in Figure 2.2a. The two vertices in this diagram represent the lowest-order QED process between charged fermions (leptons or quarks) by exchanging a Z boson. Initial or final state particles can emit and/or absorb a photon and make more complex QED diagrams. These types of radiation are known as *initial* or *final state radiation* and are shown in Figure 2.2b. Feynman diagrams like 2.2 can be used to calculate the amplitude $\mathscr{M}$ of the process. Eventually, other observables like production cross-sections can be derived directly by using amplitudes.

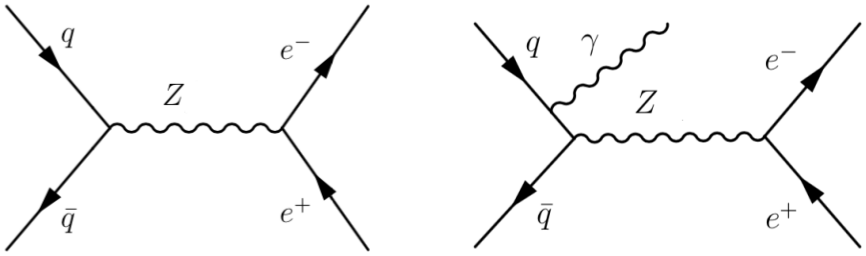

(a) (b)

Figure 2.2: Examples of leading order (2.2a), and next-to-leading order (2.2b), QED processes.

2.1.4 Quantum chromodynamics

Quantum chromodynamics (QCD) [17] is the theory which describes the strong interaction between colour-charged particles (quarks and gluons), through the exchange of gluons. There are three types of colour charge: red, blue, and green. Each quark carries one of the three colour charges. Quarks combine to make observable states, known as hadrons. For example three quarks can combine to make a baryon (qqq) or a quark and an anti-quark can can make a meson ($q\bar{q}$). QCD is based on the non-Abelian symmetry group $SU_C(3)$, where the C refers to the colour. There are eight gauge bosons (gluons) in QCD which carry colour charge, and therefore interact with both quarks and themselves (unlike the photon). Gluons are massless and have no electric charge (like the photon). Figure 2.3 shows a leading order QCD process with gluon as mediator.

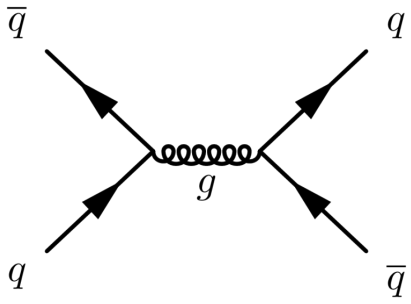

Figure 2.3: Example of leading order strong interaction.

The QCD Lagrangian describes the interaction between quarks q and gluons

$A^i_\mu (i = 1, 2, ..., 8)$, and is given by:

$$\mathcal{L}_{QCD} = \sum_q \bar{q}(i\gamma^\mu D_\mu - m)q - \frac{1}{4} G^j_{\mu\nu} G^{j\mu\nu} \quad , \tag{2.6}$$

where the summation is over all quark flavours. As explained in subsection. 2.1.2, in order to have a gauge-invariant $\mathcal{L}_{QCD}$, the covariant derivative should be defined as:

$$D_\mu = \partial_\mu - i g_s \frac{\lambda^j}{2} A^j_\mu \quad , \tag{2.7}$$

where g_s is the strong coupling constant and λ^i are the 3×3 Gell-Mann matrices. $G^i_{\mu\nu}$ are the field strength tensors for gluon fields A^i_μ, and are given by:

$$G^j_{\mu\nu} = \partial_\mu A^j_\nu - \partial_\nu A^j_\mu + g f^j_{kl} A^k_\mu A^l_\nu \quad , \tag{2.8}$$

where the structure constants f_{jkl} are defined as: $[\lambda^k, \lambda^l] = i f^{kl}_j \lambda^j$. Unlike $\mathrm{U_Y}(1)$, $\mathrm{SU_C}(3)$ is not an Abelian group ($f^{jkl} \not\equiv 0$), which means gluon self-interactions such as three- or four-gluon coupling are allowed in QCD.

The strength of strong interactions depends logarithmically on the momentum transfer between the interacting particles, and this can greatly affect gluon-loop and quark-loop corrections at leading and higher orders. The energy scale Q dependence of the strong coupling constant is given by:

$$\alpha_\mathrm{s}(\mathrm{Q}^2) = \frac{12\pi}{(33 - 2\mathrm{n_f}) \log \frac{\mathrm{Q}^2}{\Lambda^2_\mathrm{QCD}}} \quad , \tag{2.9}$$

where $\mathrm{n_f}$ is the number of quark flavors in nature and Λ_QCD is the cutoff scale with properties explained below. Setting $\mathrm{n_f} = 6$ we see that the running coupling constant $\alpha_\mathrm{s}(\mathrm{Q}^2)$ decreases with the increase of the energy scale and vice-versa. The behaviour of $\alpha_\mathrm{s}(\mathrm{Q}^2)$ is shown in Figure 2.4. At sufficiently high momentum transfer Q^2 (small distance), the effective coupling between quarks and gluons is small, so the strong interaction can be mathematically treated perturbatively. Quarks and gluons behave as free particles in this region known as *asymptotic freedom* [18,19] . On the other hand, at low momentum transfer, the strong coupling increases and makes it impossible to find free quarks or gluons. Because of the large coupling constant in this region, all quarks and gluons are confined into hadrons and this phenomenon is known as *confinement*.

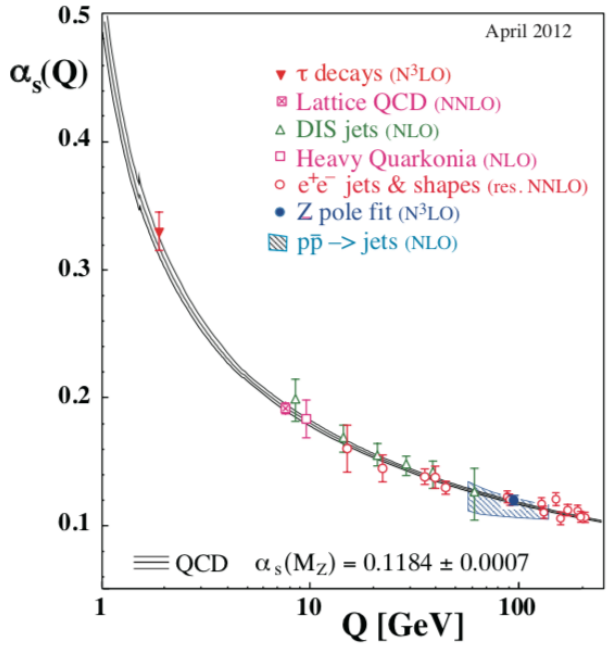

Figure 2.4: Running QCD coupling constant with the energy scale. Figure from [20].

2.1.5 Electroweak theory

In order to unify the electromagnetic and weak (but not the strong, or gravitational) forces, Glashow-Weinberg-Salam (GWS) introduced a model of *electroweak* interaction. The theory of electroweak interaction is a non-Abelian gauge theory based on $\mathrm{SU_L}(2) \times \mathrm{U_Y}(1)$ gauge symmetry. In GWS, the weak interaction is governed by $\mathrm{SU_L}(2)$ and the subscript L represents the left-handed fermions. As mentioned in subsection 2.1.3, the electromagnetic interaction is defined by $\mathrm{SU_L}(2) \times \mathrm{U_Y}(1)$ where the Y indicates the weak hypercharge.

In GWS, leptons are either in left-handed doublets L or right-handed singlets R of the SU(2) group, which are respectively represented as:

$$L = \begin{pmatrix} \nu_L \\ \ell_L \end{pmatrix}, \qquad R = \ell_R, \quad (\ell = 1, 2, 3) \ , \tag{2.10}$$

where L consists of left-handed neutrinos and charged leptons. Based on experiment, right-handed neutrinos have not been observed, so right-handed leptons R are singlet. For quarks this is the same and right-handed fields are singlet:

$$Q_{L_i} = \begin{pmatrix} U_i \\ D_i \end{pmatrix}, \qquad R = U_{Ri}, \quad D_{Ri}, \quad (i = 1, 2, 3) \ , \tag{2.11}$$

where U and D represent up- and down-type quarks respectively. The covariant derivative for the $\mathrm{SU_L}(2) \times \mathrm{U_Y}(1)$ group is:

$$D_\mu = \partial_\mu - ig\frac{\vec{\tau}}{2}.\vec{A}_\mu - ig'\frac{Y}{2}B_\mu \quad , \tag{2.12}$$

$\vec{A}_\mu$ and B_μ are gauge boson fields associated with $\mathrm{SU_L}(2)$ and $\mathrm{U_Y}(1)$ respectively. g and g' are the gauge coupling constants; Y is the weak hypercharge and $\vec{\tau}$ is the weak isospin operator defined by Pauli matrices. The component of the weak isospin and the weak hypercharge are related to the electric charge via Gell-Mann Nishijima formula, $Q = T^3 + \frac{Y}{2}$. The gauge-invariant Lagrangian for GWS is constructed as:

$$\mathcal{L}_\mathrm{F} = \bar{L}i\gamma^\mu D_\mu L + \bar{R}i\gamma^\mu D_\mu R \quad , \tag{2.13}$$

where L and R are left- and right-handed fermion fields (both leptons and quarks). The kinetic term of the gauge fields is given by:

$$\mathcal{L}_\mathrm{G} = -\frac{1}{4}F^i_{\mu\nu}F^{i\mu\nu} - \frac{1}{4}B_{\mu\nu}B^{\mu\nu} \quad , \tag{2.14}$$

where $F^i_{\mu\nu}$ and $B_{\mu\nu}$ are the gauge field strength tensors, corresponding to $\mathrm{SU_L}(2)$ and $\mathrm{U_Y}(1)$ respectively, and defined in subsection 2.1.2. There are no fermion and gauge boson mass terms in $\mathcal{L}_\mathrm{F}$ and $\mathcal{L}_\mathrm{G}$, which contradicts experiment. In order to make fermions and gauge bosons massive, the *Higgs mechanism* is needed to generate spontaneous symmetry breaking [21, 22].

The Higgs mechanism introduces two scalar fields in the form of a complex doublet format:

$$\phi = \begin{pmatrix} \varphi^+ \\ \varphi^0 \end{pmatrix} \quad , \tag{2.15}$$

φ^+ and φ^0 are positively charged and neutral complex scalar fields with hypercharge $Y = 1$. The Lagrangian for these scalars is given by:

$$\mathcal{L}_\mathrm{s} = (D_\mu\phi)^\dagger(D^\mu\phi) - V(\phi^\dagger\phi) \quad , \tag{2.16}$$

where $\phi^\dagger$ is the Hermitian conjugate and the explicit form of the covariant derivative is defined in Eq. 2.12. The potential term $V(\phi^\dagger\phi)$ is given by:

$$V(\phi^\dagger\phi) = m^2\phi^\dagger\phi + \lambda(\phi^\dagger\phi)^2 \quad , \tag{2.17}$$

where m^2 and λ are real constant parameters. The value of these parameters determines the shape of the potential. For example if $\lambda > 0$ and $m^2 > 0$, the potential has only one minimum corresponding to $\phi = 0$. The case where the vacuum is unique is known as the *Wigner phase*. On the other hand, if $\lambda > 0$ and $m^2 = -\mu^2(\mu^2 > 0)$, all points on a circle with radius $v = \sqrt{\mu^2/\lambda}$ in the (φ_1, φ_2) plane correspond to the minimum of the V. This allows for spontaneous symmetry breaking (SSB) since the symmetry of the vacuum will be broken by the arbitrary choice of complex phase as the field falls into a position that is chosen randomly on the circle of minimum potential. Both options are shown in Figure 2.5. As explained before, SSB occurs when the scalar doublet ϕ, defined in Eq. 2.15, gets a vacuum expectation value (VEV)

$$\phi_0 = \begin{pmatrix} 0 \\ v/\sqrt{2} \end{pmatrix} \quad . \tag{2.18}$$

Now we can parametrize the scalar doublet in terms of the fields relative to the vacuum state ϕ_0

$$\phi = e^{\frac{i\vec{\tau}.\vec{\xi}}{2v}} \begin{pmatrix} 0 \\ (v + H(x))/\sqrt{2} \end{pmatrix} \quad . \tag{2.19}$$

Here two complex scalar fields φ^+ and φ^0 are replaced by 4 real fields, $\xi_i (i = 1, 2, 3)$, known as Goldstone bosons, which are absorbed into the longitudinal components of $W^\pm$ and Z^0 bosons, and H is a Higgs boson.

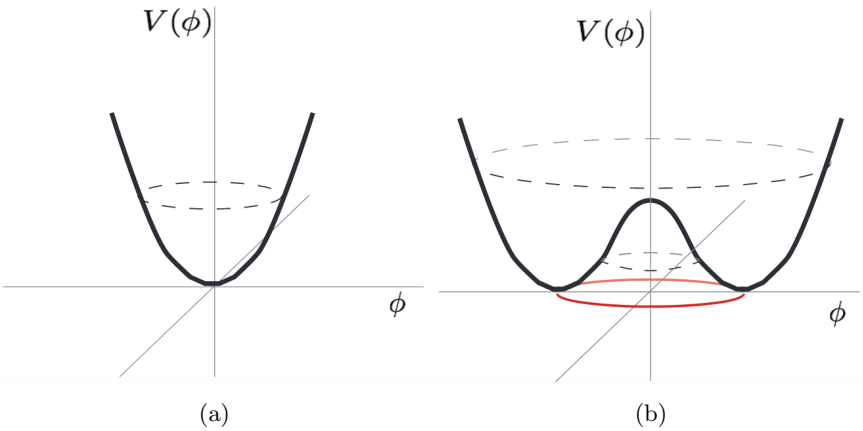

(a) (b)

Figure 2.5: Higgs potential shape for 2.5a Wigner phase and 2.5b SSB.

Substituting scalar fields defined in Eq. 2.19 into the scalar Lagrangian

defined in Eq. 2.16 yields:

$$\mathcal{L}_{\text{mass}} = \frac{v^2}{8}(g^2 A^1_\mu A^{1\mu} + g^2 A^2_\mu A^{2\mu} + (gA^3_\mu - g'B_\mu)^2) \quad . \tag{2.20}$$

To make this Lagrangian simpler, we can introduce charged boson fields $W^\pm$:

$$W^\pm \equiv \frac{A^1_\mu \mp iA^2_\mu}{\sqrt{2}} \quad . \tag{2.21}$$

Then the sum of the first and second terms of Eq. 2.20 can be written as $\frac{1}{4}g^2v^2W^+_\mu W^-_\mu$ which implies that the charged gauge bosons are massive with $M_W = \frac{1}{2}gv$. The third term in Eq. 2.20 which contains neutral fields can be written as $\frac{v^2}{8}(g^2 + g'^2)Z_\mu Z^\mu + 0.A_\mu A^\mu$ if we use the following orthogonal transformation:

$$\begin{pmatrix} Z_\mu \\ A_\mu \end{pmatrix} = \begin{pmatrix} \cos\theta_{\text{W}} & -\sin\theta_{\text{W}} \\ \sin\theta_{\text{W}} & \cos\theta_{\text{W}} \end{pmatrix} \begin{pmatrix} A^3_\mu \\ B_\mu \end{pmatrix} \quad , \tag{2.22}$$

where θ_{W} is called the weak mixing angle and is dependent on the coupling constants by $\tan\theta_{\text{W}} \equiv \frac{g'}{g}$. From the third term, we can see that the neutral Z boson, which is the mediator of the weak force, becomes massive with the mass:

$$M_Z = \frac{1}{2}v\sqrt{g^2 + g'^2} \quad . \tag{2.23}$$

and the other neutral boson A_μ is the massless photon of the electromagnetic force. The last part of the GWS is the Yukawa interaction which represents the coupling of fermions to the Higgs field. The Yukawa Lagrangian for e^-e^+ is:

$$\begin{aligned} \mathcal{L}_{\text{Y}} &= -G_e(\bar{L}\phi R + \bar{R}\phi^\dagger L) \\ &= -G_e(\bar{e}_L \frac{1}{\sqrt{2}}(v+H)e_R + \bar{e}_R \frac{1}{\sqrt{2}}(v+H)e_L) \\ &= -\frac{G_e v}{\sqrt{2}}\bar{e}e - \frac{G_e}{\sqrt{2}}H\bar{e}e \quad . \end{aligned} \tag{2.24}$$

The first term in this equation represents the fermion mass $m_e = \frac{G_e}{\sqrt{2}}v$ and the second term corresponds to the fermion coupling to the Higgs boson. We can easily identify that the fermion mass depends on the vacuum expectation value v of the Higgs boson and the coupling is proportional to the fermion mass by $\frac{G_e}{\sqrt{2}} = \frac{m_e}{v}$.

2.2 Open questions in the Standard Model

The SM is the most successful theory in particle physics, describing all known particles and interactions. However, in particle physics there are still some open questions that imply the SM needs to be extended to describe physics at higher energies. A few of the open questions are listed below:

Hierarchy Problem

The Higgs boson mass is measured by considering the tree-level and loop corrections. At tree-level, the mass of the Higgs boson is given directly by inserting Eq. 2.19 in Eq. 2.17 ($m_{\mathrm{H}} = \sqrt{2\mu^2}$). Then, the fermion Yukawa coupling ($-G_f \bar{f} H f$) will make a mass correction to the Higgs boson mass. The Feynman diagram corresponding to the fermion loop correction is shown in Figure 2.6, and this diagram yields a mass correction:

$$\Delta m_{\mathrm{H}}^2 = -\frac{|G_f|^2}{8\pi^2}\Lambda_{\mathrm{UV}}^2 + \ldots \quad , \tag{2.25}$$

Λ_{UV} is an ultraviolet momentum cutoff scale. It identities the energy scale at which new physics enters to alter the high-energy behaviour of the theory. If Λ_{UV} is of the order of the Planck scale $M_P = 2.4 \times 10^{18}$ GeV, then the fermion loop correction to m_{H}^2 is vastly larger that what is computed from the theory [23]. (This issue is also known as quadratic divergence).

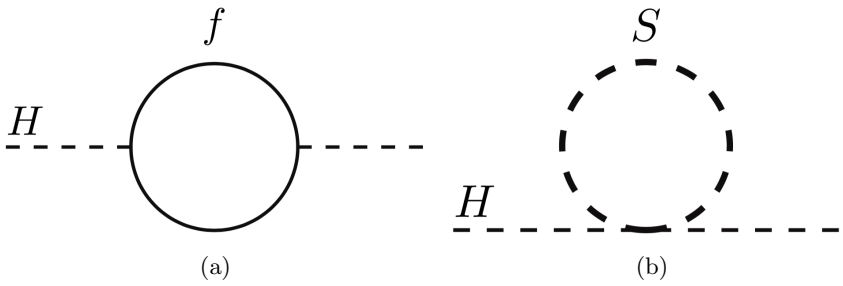

Figure 2.6: First-order loop corrections to the Higgs squared mass m_{H}^2 due to 2.6a a fermion coupling f, and 2.6b a scalar coupling S. Figure from [24].

One way to solve this divergence is to suppose there exists a heavy complex scalar particle S that couples to the the Higgs boson through $-G_s|H|^2|S|^2$ as shown in Figure 2.6b. This scalar field results in a Higgs mass correction:

$$\Delta m_{\mathrm{H}}^2 = \frac{G_{\mathrm{S}}}{16\pi^2}\left[\Lambda_{\mathrm{UV}}^2 - 2m_{\mathrm{S}}^2 \ln(\Lambda_{\mathrm{UV}}/m_{\mathrm{S}}) + \ldots\right] \quad . \tag{2.26}$$

Considering the opposite sign between contributions to $\Delta m_{\rm H}^2$ from fermion loops (in Eq. 2.25), and boson loops (in Eq. 2.26), this indicates that this hierarchy problem could be resolved via a new symmetry related to fermions and bosons (called *supersymmetry*). If a complex scalar field is associated to each of the quarks and leptons in the SM with $G_{\rm S} = |G_f|^2$, the quadratic divergence ($\Lambda_{\rm UV}^2$) will be cancelled.

Neutrino Oscillations and Masses

In the SM, neutrinos are massless particles. However neutrinos are known to have mass and they may be ordinary Dirac masses and possibly Majorana mass terms:

$$\mathcal{L}_{\rm m} = -\frac{1}{2} m_R (\bar{\nu_R^c}) \nu_R - \frac{1}{2} m_R (\bar{\nu_L^c}) \nu_L - m_D \bar{\nu_R} \nu_L \quad , \tag{2.27}$$

where ν_L^c is a left-handed antineutrino produced by charge conjugation operator. The first two terms correspond to Majorana mass and the third term corresponds Dirac mass. Phenomena such as $\nu_e \to \nu_\mu$ where a neutrino is transformed into another neutrino with different flavor are called "neutrino oscillations" [25] Observations from neutrino experiments such as "Super-Kamiokande" confirm that the probability of having a neutrino oscillation $\nu_\alpha \to \nu_\beta$ is:

$$P(\nu_\alpha \to \nu_\beta) = \left| \sum_i U_{\beta i} e^{-\frac{\Delta m_{i1}^2}{2E} t} U_{\alpha i}^* \right| \quad , \tag{2.28}$$

where the difference in the square of the masses is given by Δm_{i1}^2 and the unitary matrix U corresponds to the flavor mixing angle Maki-Nakagawa-Sakata (MNS) matrix. This formula clearly shows that to have neutrino oscillations, both flavor mixing described by a non-diagonal U and nonzero mass differences Δm_{i1}^2 are necessary.

There are additionally many other open questions in particle physics, for example: "How can general relativity and the standard model be combined [26]?", "What is the microphysical nature of dark matter [27–29]?", and "Why is there more matter than anti-matter in the Universe [30]?", and "Can we unify the strong and electroweak interactions [31]?". Supersymmetry is an extension of the Standard Model that aims to fill some of these gaps. More details about the framework of supersymmetry are given in the next Section.

2.3 Supersymmetry

Supersymmetry (SUSY) [32–37] comprises a category of beyond-Standard Model BSM theories that provides solutions to some of the open questions listed in Section 2.2. The SM contains several symmetries (as discussed before) between particles, and any theory beyond the SM should include both those pre-existing and new ones. Supersymmetry introduces a new symmetry that relates the fermions and bosons. To elucidate this new symmetry, the supercharge operator Q, which is the generator of supersymmetry transformations, can be used:

$$\begin{aligned} Q\,|\text{Fermion}\rangle_{\text{SM}} &= \quad |\text{Boson}\rangle_{\text{SUSY}} \\ Q\,|\text{Boson}\rangle_{\text{SM}} &= |\text{Fermion}\rangle_{\text{SUSY}} \quad . \end{aligned} \tag{2.29}$$

Based on this pair of equations, all the spin-1 gauge bosons of the SM have spin-1/2 superpartners in SUSY, and all the spin-1/2 fermions of the SM have spin-0 superpartners. All types of SUSY particles are listed in subsection 2.3.1. If SUSY were unbroken then the SM particles and their supersymmetric partners would have the same masses. Since no SUSY particles have been discovered, then if SUSY correctly describes nature, it must be a broken symmetry. There are a variety of SUSY breaking mechanisms, and some of them are discussed in subsection 2.3.3.

2.3.1 SUSY particles and supermultiplets

The particle states in SUSY are organized within irreducible representations of Lie algebras, called "*supermultiplets*". Each supermultiplet contains a fermion state and a boson state which are superpartners of each other. There are three types of supermultiplets:

Chiral supermultiplets

These are the simplest supermultiplets, and each contains a Weyl (massless) fermion and two real scalars as its superpartner. The fermionic degrees of freedom for each Weyl fermion (corresponding to two different spin helicity states: $n_F = 2$) results in the existence of two real scalar bosons (each with $n_B = 1$). The superpartners of fermions (leptons and quarks) are called "*sfermions*" (sleptons and squarks), and a tilde ($\tilde{}$) is used to represent the superparticles. The Higgs boson must be in a chiral supermultiplet, since it has spin 0. All chiral supermultiplets in the Minimal Supersymmetric Standard Model

are shown in Table 2.2.

Names		Spin 0	Spin 1/2	$SU(3)_C, SU(2)_L, U(1)_Y$
squarks, quarks	Q	$(\tilde{u}_L\ \tilde{d}_L)$	$(u_L\ d_L)$	$(3,\ 2,\ \frac{1}{6})$
(×3 families)	$\bar{u}$	$\tilde{u}_R^*$	$u_R^\dagger$	$(3,\ 1,\ -\frac{2}{3})$
	$\bar{d}$	$\tilde{d}_R^*$	$d_R^\dagger$	$(3,\ 1,\ \frac{1}{3})$
sleptons, leptons	L	$(\tilde{\nu}\ \tilde{e}_L)$	$(\nu\ e_L)$	$(1,\ 2,\ -\frac{1}{2})$
(×3 families)	$\bar{e}$	$\tilde{e}_R^*$	$e_R^\dagger$	$(1,\ 1,1)$
Higgs, higgsinos	H_u	$(H_u^+\ H_u^0)$	$(\tilde{H}_u^+\ \tilde{H}_u^0)$	$(1,\ 2,\ +\frac{1}{2})$
	H_d	$(H_d^+\ H_d^0)$	$(\tilde{H}_d^+\ \tilde{H}_d^0)$	$(1,\ 2,\ -\frac{1}{2})$

Table 2.2: Chiral supermultiplets in the Minimal Supersymmetric Standard Model. Table from [24].

Gauge/Vector supermultiplets

Gauge bosons of the SM and their fermionic superpartners reside in gauge supermultiplets. The names of fermionic supersymmetric particles are the same as the corresponding SM gauge bosons but with a -ino suffix.

The last SUSY particle is the gravitino which is the superpartner of the graviton. Gravity should be mediated by the graviton with spin 2, so the gravitino should be a spin-3/2 SUSY particle [24]. Gravitinos are the lightest supersymmetric particles in gauge-mediated SUSY-breaking (GMSB) models.

2.3.2 Minimal Supersymmetric Standard Model

The Minimal Supersymmetric Standard Model (MSSM) [38] is the supersymmetric extension to the Standard Model with the minimum number of new

Names	Spin 1/2	Spin 1	$\mathbf{SU(3)_C, SU(2)_L, U(1)_Y}$
gluino, gluon	$\tilde{g}$	g	**(8, 1, 0)**
winos, W bosons	$\tilde{W}^{\pm}\ \tilde{W}^{0}$	$W^{\pm}\ W^{0}$	**(1, 3, 0)**
bino, B boson	$\tilde{B}^{0}$	$\tilde{B}^{0}$	**(1, 1, 0)**

Table 2.3: Gauge supermultiplets in the Minimal Supersymmetric Standard Model. Table from [24].

particle states and new interactions consistent with SUSY and with the existing SM. The superpotential for MSSM is:

$$W_{\text{MSSM}} = \tilde{u} y_{\text{u}} \tilde{Q} H_{\text{u}} - \tilde{d} y_{\text{d}} \tilde{Q} H_{\text{d}} - \tilde{e} y_{\text{e}} \tilde{L} H_{\text{d}} - \mu H_{\text{u}} H_{\text{d}} \quad , \tag{2.30}$$

where $Q, \tilde{u}, \tilde{d}, L$ are scalar components of the chiral supermultiplets (squarks and sleptons), and the Yukawa coupling parameters are given by $y_{\text{u}}, y_{\text{d}}, y_{\text{e}}$. The μ term is the SUSY version of the Higgs boson mass. Two examples for supersymmetric interactions proportional to Yukawa couplings are shown in Figure 2.7.

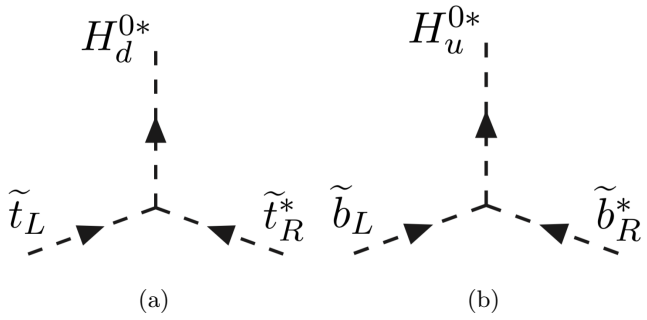

Figure 2.7: Examples of supersymmetric Higgs couplings to (a) stop and (b) sbottom.

The MSSM description can be completed by adding SUSY-breaking terms in order to have massive superparticles. The general soft SUSY-breaking Lag-

rangian includes mass terms for gauginos and scalar fields:

$$\begin{aligned}\mathcal{L}_{\text{soft}}^{\text{MSSM}} = &-\frac{1}{2}\left(M_3\tilde{g}\tilde{g} + M_2\tilde{W}\tilde{W} + M_1\tilde{B}\tilde{B}\right) \\ &-\left(\tilde{u}a_{\text{u}}\tilde{Q}H_{\text{u}} - \tilde{d}a_{\text{d}}\tilde{Q}H_{\text{d}} - \tilde{e}a_{\text{e}}\tilde{L}H_{\text{d}}\right) \\ &-\tilde{Q}^{\dagger}\text{m}_{\text{Q}}^2\tilde{Q} - \tilde{L}^{\dagger}\text{m}_{\text{L}}^2\tilde{L} - \tilde{u}^{\dagger}\text{m}_{\text{u}}^2\tilde{u} - \tilde{d}^{\dagger}\text{m}_{\text{d}}^2\tilde{d} - \tilde{e}^{\dagger}\text{m}_{\text{e}}^2\tilde{e} \\ &-m_{H_u}^2 H_u H_u - m_{H_d}^2 H_d H_d - (bH_u H_d) \quad .\end{aligned}$$

The first and the third rows include the mass terms for gauginos and sfermions. $a_{\text{u}}, a_{\text{d}}, a_{\text{e}}$ are 3×3 matrices in one-to-one correspondence with the Yukawa couplings, and make it possible to have Higgs-sfermion-sfermion interactions. This Lagrangian introduces many new parameters: 105 masses, phases, and mixing angles, which makes SUSY difficult to explore [24].

In order to have baryon number (B) and lepton number (L) conservation in MSSM, "R-parity" is added to the theory [39]. R-parity is defined as:

$$P_R = (-1)^{3(\text{B}-\text{L})+2s} \quad , \tag{2.31}$$

where s corresponds to the spin of the particle. All the SM particles have even R-parity ($P_R = +1$), while all the MSSM particles like squarks, sleptons, gauginos, and higgsinos have odd R-parity ($P_R = -1$). Some of the phenomenological consequences of R-parity conservation are:

- There should be an even number of supersymmetric particles in every interaction vertex.
- The lightest supersymmetric particle (LSP) with $P_R = -1$ must be stable. LSPs are neutral supersymmetric particles, interact only weakly with matter and can be a candidate for the non-baryonic dark matter. All SUSY particles must decay to a final state containing an odd number of LSPs.

2.3.3 Supersymmtery-breaking models

In order to have massive sparticles, the MSSM needs to be extended via spontaneous symmetry breaking. It is not easy to make a phenomenological framework with renormalizable interactions to achieve SUSY breaking. One problem relates to the fact that there is no coupling of (scalar)-(gaugino)-(gaugino) in supersymmetry to cause gaugino mass. The typical expectation is that SUSY breaking occurs in a "hidden sector". The hidden sector would contain new

particles that are not part of the MSSM fields. On the other hand, MSSM particles (the SM particles and superparticles) live in the "visible sector." The particles in the hidden and visible sectors have no or very small couplings with particles in the other sector. However, some interactions can make communication possible for SUSY-breaking between the two sectors. The two sectors and mediators are shown in Figure 2.8.

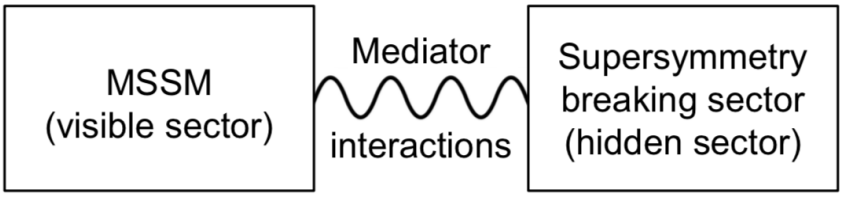

Figure 2.8: SUSY breaking and MSSM sectors. The mediator connects the hidden sector to the visible sector.

We can distinguish two mechanisms, depending on which interaction provides the communication between the SUSY-breaking sector and the MSSM sector:

Planck-scale-mediated SUSY-breaking (PMSB)
In these models the SUSY-breaking sector connects with the MSSM sector through gravitational interactions. In PMSB [40–42], what is called the soft term in the visible sector is given by:

$$m_{\text{soft}} \sim \frac{\langle F \rangle}{M_{\text{P}}} \quad , \tag{2.32}$$

where $\langle F \rangle$ is the VEV of the SUSY-breaking field in the hidden sector and M_{P} is the Planck scale (2.4×10^{18} GeV). Equation 2.32 shows that when SUSY is unbroken ($\langle F \rangle \to 0$) or gravity is negligible ($M_{\text{P}} \to \infty$), m_{soft} should vanish. After writing the SUSY-breaking Lagrangian and minimizing the form for the normalization of kinetic terms and gauge interactions which is called *minimal supergravity* (MSUGRA), the soft terms in $\mathcal{L}_{\text{soft}}^{\text{MSSM}}$ are all determined by these

parameters:

$$\begin{aligned} m_{1/2} &= f\frac{\langle F\rangle}{M_{\mathrm{P}}} \\ m_0^2 &= (k+n^2)\frac{\langle F\rangle^2}{M_{\mathrm{P}}^2} \\ A_0 &= (\alpha+3n)\frac{\langle F\rangle}{M_{\mathrm{P}}} \\ B_0 &= (\beta+2n)\frac{\langle F\rangle}{M_{\mathrm{P}}} \quad , \end{aligned} \tag{2.33}$$

where $m_{1/2}$ is the gaugino mass parameter, m_0 is the scalar (squarks and sleptons) mass, A_0 is the supersymmetrization of the Yukawa coupling, and B_0 relates to the Higgs mass parameter by $b = B_0\mu$. Based on Eq. 2.33 in MSUGRA the entire MSSM spectrum can be predicted by just five parameters $m_{1/2}, m_0, A_0, B_0$, and μ. In all the SUSY-breaking models, Higgsino ($\tilde{H}$) and gauginos ($\tilde{W}, \tilde{Z}$) can combine to form neutralinos ($\tilde{N}$) and charginos ($\tilde{C}$). In MSUGRA, the neutralino is the LSP which means all SUSY particles decay finally to the neutralino.

Gauge-mediated SUSY-breaking (GMSB)

GMSB [43–47] is another SUSY-breaking model where ordinary gauge interactions are responsible for transmission of SUSY-breaking effects to the visible sector. In GMSB, a set of chiral supermultiplets (fermion and boson superpartners), called "messengers," make the connection between the hidden and visible sectors. Messengers interact both with the source of the SUSY-breaking VEV $\langle F\rangle$ and MSSM fields (through $\mathrm{SU_C}(3) \times \mathrm{SU_L}(2) \times \mathrm{U_Y}(1)$ gauge boson and gaugino interactions). Due to SUSY-breaking, the fermion messengers obtain different masses from the boson messenger particles. It is through the messenger 1-loop contribution that MSSM gauginos obtain mass:

$$m_{\mathrm{soft}} \sim \frac{\alpha}{4\pi}\frac{\langle F\rangle}{M_{\mathrm{mess}}} \quad , \tag{2.34}$$

where $\frac{\alpha}{4\pi}$ is a loop factor for gauge interactions and M_{mess} is a mass scale for messenger particles. The mass of squarks and sleptons comes from 2-loop contributions, but the mass scale is still as in Eq. 2.34. In GMSB the spin-3/2 gravitino (the superpartner of the graviton) is the LSP. As discussed in Section. 2.1.5, the $W^{\pm}$ and Z^0 gauge bosons in the SM obtain mass by absorbing

Goldstone bosons. In a similar way, the gravitino in GMSB gains a mass by absorbing ("eating") the spin-1/2 particle after the spontaneous symmetry breaking.

Chapter 3

The Large Hadron Collider and the ATLAS detector

This chapter provides an introduction to the large hadron collider, LHC, the world's highest energy particle accelerator, and the ATLAS detector, one of the four main experiments at the LHC. The LHC can accelerate bunches of protons to 99.99999991% of the speed of light, and after colliding some of the protons in the bunches , new heavy particles can be made. After reconstructing the charged particle trajectory and energy deposits resulting from the collision, these new particles can be detected by ATLAS. Section 3.1 describes the LHC and briefly the other accelerators at CERN. In addition, some of the LHC parameters such as luminosity and pileup are explained in this Section. The ATLAS structure is discussed in Section 3.2.

3.1 The Large Hadron Collider

The LHC [48] at CERN is a synchrotron particle accelerator located on the border between France and Switzerland. It is 27 km in circumference, located in an underground tunnel up to 170 m below ground level which was previously used by the Large Electron-Positron Collider (LEP) [49]. The LHC collides beams of proton bunches moving in opposite directions at four different points. Four particle detectors, ATLAS [50], CMS [51], ALICE [52], and LHCb [53], housed at these points, can detect the production of these proton-proton collisions. 1232 superconducting dipole magnets that are each 15 m long are used to keep the proton beams in a circular path. These dipole magnets are made of a niobium-titanium alloy and are cooled by 150 tons of superfluid helium

at a temperature of 1.9 K [54]. The LHC dipoles provide an 8.3 T magnetic field which bends the paths of the protons to keep them inside the ring. 392 quadrupole magnets along the LHC ring are used to focus the proton bunches by squeezing them either vertically or horizontally. Radio-frequency (RF) cavities along the LHC tunnel provide electrical fields to accelerate proton beams. There are 16 RF cavities oscillating with a 400 MHz frequency and each can produce 5 MeV/m accelerating field.

There are several accelerators within the complex at CERN, of which LHC is the last step in this chain, where protons are accelerated up to 6.5 TeV. The summary for other accelerators is mentioned below:

- At Linac2 the proton source (hydrogen gas) is ionized by an electric field, and the resulting protons are accelerated to a kinetic energy of 50 MeV.
- The first synchrotron accelerator in the chain, the Proton Synchrotron Booster (PSB), is made up of four superimposed synchrotron rings, and increases the kinetic energy of the protons to 1.4 GeV.
- The Proton Synchrotron (PS) was CERN's first synchrotron with 628 m circumference and 100 dipoles, and further accelerates the protons to 25 GeV kinetic energy.
- With a circumference of 7 kilometers, the Super Proton Synchrotron (SPS) is the second-largest machine in CERN's complex. The SPS accelerates the protons up to 450 GeV and it includes 744 dipoles. The Nobel-Prize-winning discovery of W and Z bosons was made at the SPS running (during years 1976 - 1983) with proton-antiproton beams.
- The last and the largest particle accelerator is the LHC, which first started up on 10 September 2008. In the LHC it takes 15 minutes for each beam to reach the present maximum energy of 6.5 TeV (design energy is 7 TeV for each beam).

A general schematic (not to scale) of all CERN accelerators and the locations of the four main LHC experiments (ATLAS, CMS, LHCb, ALICE) can be seen in Figure 3.1.

3.1.1 LHC operational parameters

The center-of-mass energy and the integrated luminosity are two of the most important parameters at LHC. The LHC is designed to provide collisions at

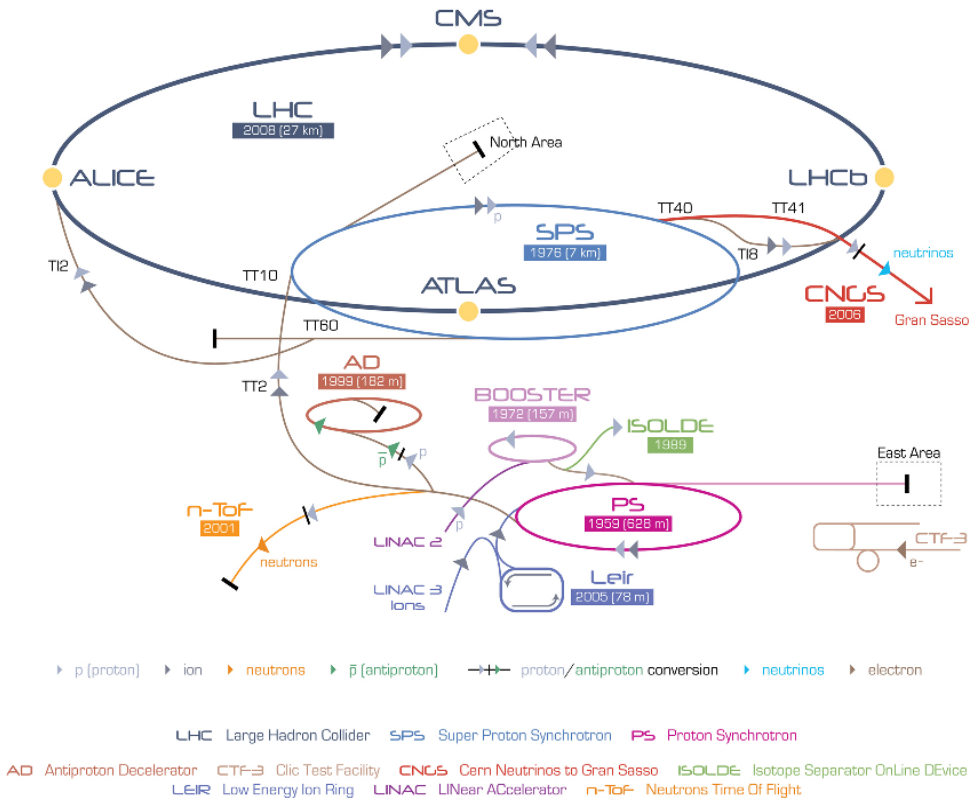

Figure 3.1: The CERN accelerator complex. There are four interaction points along the four main detectors. The accelerator chain is as follows: Linac2 → PSB → PS → SPS → LHC. Figure from [55].

$\sqrt{s} = 14$ TeV center-of-mass[1]. During 2011 and 2012, the LHC was running with a centre-of-mass energy of 7 and 8 TeV, and then after the first long shutdown (between 2013-2015), the LHC started colliding protons at 13 TeV. The LHC is shut down now (second long shutdown) for a series of upgrades, then it is expected to operate at $\sqrt{s} = 14$ TeV. The LHC upgrade plan leading to High Luminosity LHC is described in this Reference [56].

There are two measures of luminosity in the LHC: instantaneous and total integrated luminosity. The instantaneous luminosity represents the number of collisions that can be produced per unit time and per transverse area. The instantaneous luminosity is defined as:

$$\mathcal{L} = \frac{f N_b n_1 n_2}{4\pi\sigma_x\sigma_y} \quad , \tag{3.1}$$

which implies that the instantaneous luminosity depends on the properties of

[1]The definition of s is as the following: $s = (p_1 + p_2)^2$ while $p_1 = (E_p, p)$ and $p_2 = (E_p, -p)$. p_1 and p_2 are four-momenta of the two proton beams.

the colliding bunches of protons. n_1 and n_2 are the number of protons in each of the two colliding bunches, N_b is the number of bunches in each beam, f is the revolution frequency 11.2455 kHz, and σ_x and σ_y are the horizontal and vertical transverse beam size at the interaction point. The transverse beam sizes at the interaction point are given by $\sigma_{x,y} = \sqrt{\epsilon_{x,y}\beta^*_{x,y}}$, where $\epsilon_{x,y}$ are known as the horizontal and vertical emittance, and $\beta^*_{x,y}$ are known as the horizontal and vertical amplitude functions at the location of the interaction point [57]. The emittance $\epsilon_{x,y}$ provides a measure of the average spread of proton coordinates in position-and-momentum phase space. The amplitude functions at the interaction point $\beta^*_{x,y}$ are determined by the focusing properties of the LHC magnets near the interaction point and around the ring. As an example, the peak instantaneous luminosity during 2018 data-taking is shown in Figure 3.2a.

To calculate integrated luminosity $\mathcal{L}_{\text{int}}$, we can integrate the instantaneous luminosity with respect to time:

$$\mathcal{L}_{\text{int}} = \int \mathcal{L} dt \quad . \tag{3.2}$$

In Figure 3.2b, the total integrated luminosity during Run 2 data taking (between 2015 and 2018) is shown. Multiplying the production cross section for a specific physics process (such as an expected production cross section for a specific SUSY signal channel) and the integrated luminosity yields the total number of events for that process:

$$N_{\text{event}} = \mathcal{L}_{\text{int}} . \sigma \quad . \tag{3.3}$$

After operating at near-nominal parameters for some years, the LHC will be upgraded for significantly higher luminosity. A higher luminosity likely will be necessary to produce an observable number of possible new heavy particles. Higher luminosity increases the probability of observing multiple proton-proton interactions per bunch crossing (pileup). There are two types of pileup:

- In-time pileup: Signals from particles that have resulted from multiple proton-proton collisions within the same bunch crossing; and
- Out-of-time pileup: Signals from particles that have resulted from additional proton-proton collisions that happen in bunch crossings either just before, or just after, the bunch crossing that contains the primary interaction.

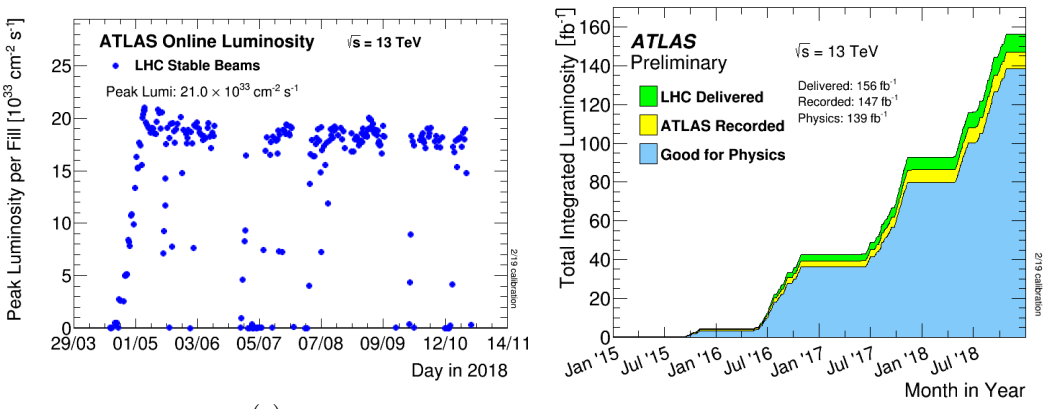

(a) (b)

Figure 3.2: Peak instantaneous luminosity for 2018 data taking 3.2a, and cumulative luminosity versus time delivered to ATLAS (green), recorded by ATLAS (yellow), and certified to be good quality data (blue) during stable beams for pp collisions at 13 TeV centre-of-mass energy in 2015-2018 3.2b. Figures from [58].

Pileup is typically quantified by $\langle\mu\rangle$, which is defined as the average number of minimum bias interactions per bunch crossing . When averaged across all of ATLAS Run 2 data, $\langle\mu\rangle$ is 33.7. Figure 3.3 shows the mean number of interactions per bunch crossing, recorded by the ATLAS detector, during 2015 – 2018 data taking. The mean number of interactions per crossing ($\mu = \mathcal{L}\sigma_{\text{inel}}/fn_b$) is proportional to the instantaneous luminosity $\mathcal{L}$, the inelastic proton-proton collision cross section σ_{inel}, the revolution frequency f at which the bunches collide, and number of bunches per beam n_b.

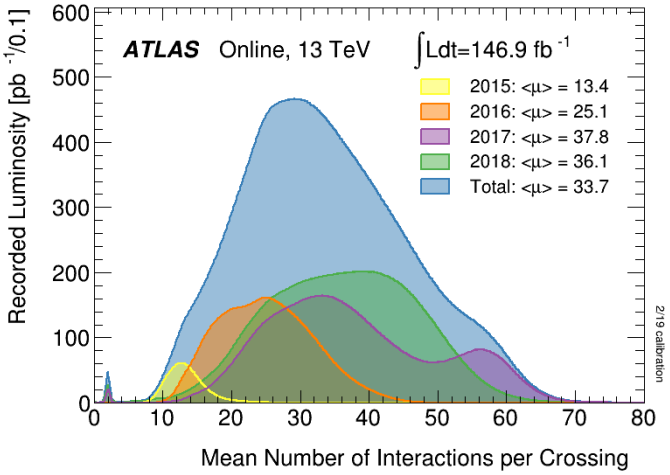

Figure 3.3: Mean number of interactions per bunch crossing distribution for Run 2 (2015-2018) proton-proton collision recorded by the ATLAS experiment during stable beam. Figure from [58].

3.2 The ATLAS Detector

ATLAS (illustrated in Figure 3.4) is one of the two detectors at the LHC used to probe the widest possible range of physics, from SM properties to extra dimensions and other physics beyond the SM. The ATLAS detector is located approximately 100 meters underground, is approximately 44 meters in length and 25 meters in height, and weighs approximately 7000 tons. The collisions occur at the center of the detector (interaction point) and the produced particles leave energy deposits at different subdetector layers. There are four main subdetectors in ATLAS: the Inner Detector (ID) with a cylindrically-shaped barrel and two disk-like end-caps, the Electromagnetic Calorimeter (ECal), the Hadronic Calorimeter (HCal), and the Muon tracking system. All subdetectors are shown in Figure 3.4.

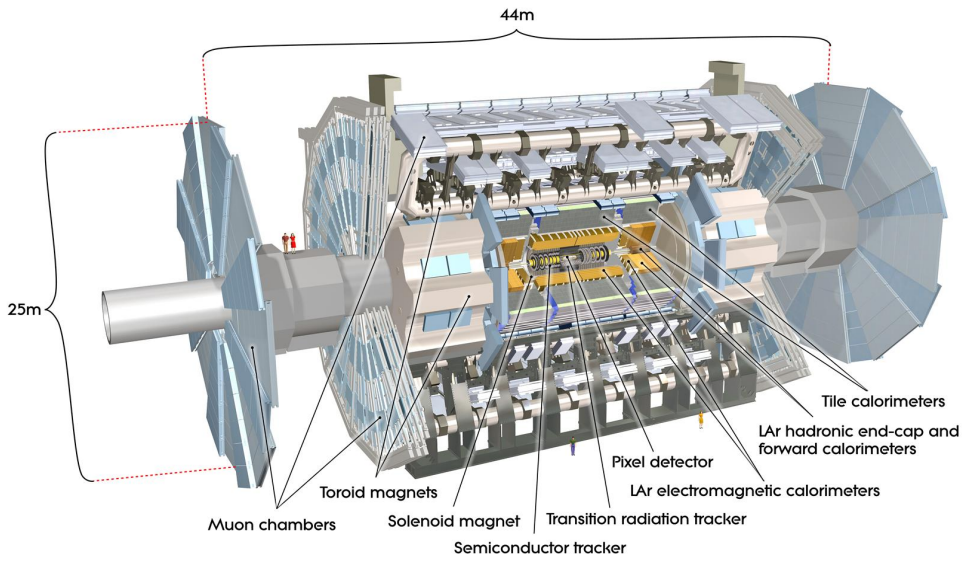

Figure 3.4: The ATLAS detector with all subdetectors and magnet systems. Figure from [50].

As a summary for each subdetector: charged particles are produced at the collision point and travel outwards leaving tracks in the inner detector. The ID collects information from these tracks to make high-precision measurements such as transverse momentum and charge. The ECal, which is just outside the ID, measures the energy of the particles that produce electromagnetic showers in the ECal, such as photons or electrons [50]. The outer calorimeter, HCal, is designed to measure the energy of hadrons which interact via strong interaction like neutrons or charged pions. The only charged particles which traverse the

whole detector with no large energy deposition in the ECal or the HCal, are the muons. The muon spectrometer is the outermost layer of ATLAS, measures the track and momentum of high energy muons. Figure 3.5 shows various fundamental particle interactions inside ATLAS and how they are detected by different subdetectors.

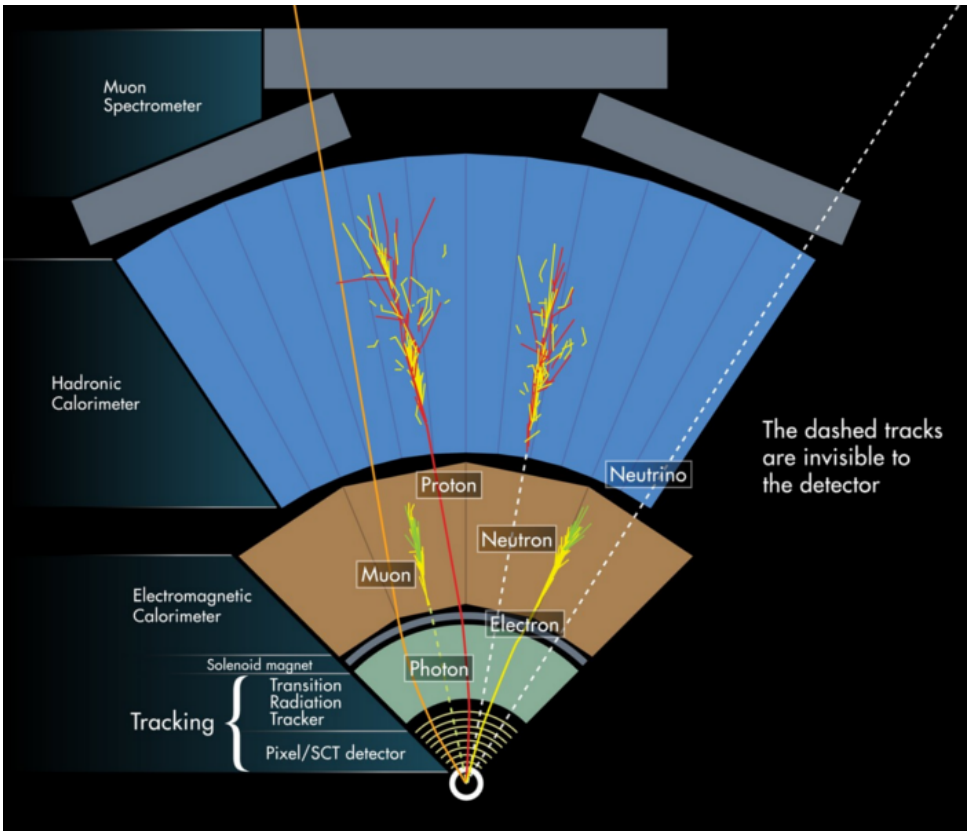

Figure 3.5: Diagram of the ATLAS detector, showing particle interactions with the various subdetectors, as well as the effects of the magnetic field. Figure from [59].

3.2.1 Coordinate system

ATLAS uses a right-handed coordinate system with the center at the nominal interaction point. The beam direction defines the z-axis (with positive z pointing toward the A-side of the cavern, which is in the direction of the Geneva Airport; and negative z pointing toward the cavern C-side, which is in the direction of the Jura), and the $x-y$ plane is perpendicular to the beam direction. The positive x-axis points from the interaction point toward the center of the LHC ring and the positive y-axis points upward as shown in Figure 3.6. In cyl-

indrical coordinates, the radial coordinate $r = \sqrt{x^2 + y^2}$ points outward, and the azimuthal angle $\phi = \text{atan2}(y, x)$ is zero along the positive x-axis, and points counter-clockwise around the beam axis when one looks toward the A-side of the cavern. In spherical coordinates, the polar angle θ is zero along the positive z-axis, and reaches a maximum of $+\pi$ along the negative z-axis. In most cases pseudorapidity η is used instead of θ since the distribution of particles in a detector is approximately flat as a function of pseudorapidity. Pseudorapidity is defined as:

$$\eta = -\ln \tan\left(\frac{\theta}{2}\right) \quad , \tag{3.4}$$

where large positive values of η correspond to the region close to the positive z-axis and $\eta = 0$ is perpendicular to the beam. In general, pseudorapidity is an approximation of rapidity in the limit of massless particles $|p| \gg m$. Rapidity y is defined as:

$$y = \frac{1}{2} \ln \left[\frac{E + p_z}{E - p_z}\right] \quad , \tag{3.5}$$

where E denotes the particle's energy, and p_z is the particle's momentum along the (z-axis). Rapidity and pseudorapidity are preferable to polar angle, since the rapidity difference Δy is Lorentz invariant along the beam axis [60] (with the same invariance for pseudorapidity in the limit of massless particles).

In hadron colliders, kinematic variables such as momentum and energy tend to be measured in the transverse plane when they are used in analysis. They are then refereed to as transverse momentum p_T and transverse energy E_T. Energy-momentum conservation is used purely in the transverse plane, since the longitudinal component of the colliding protons' momenta is not conserved by the hard-scattering products of the collision, since only one part (i.e., one parton) of each proton undergoes the hard scatter. Protons are composed of partons (quarks and gluons), and each parton has a varying fraction of the longitudinal momentum of its parent proton. Transverse momentum in the (x, y) plane is defined as:

$$p_T = \sqrt{p_x^2 + p_y^2} \quad , \tag{3.6}$$

where p_x and p_y are the momentum values projected onto the $x - y$ plane.

3.2.2 Inner detector and solenoid magnet

The inner detector in ATLAS [61, 62] measures the position and momentum of charged particles with high precision, and determines the position of the the

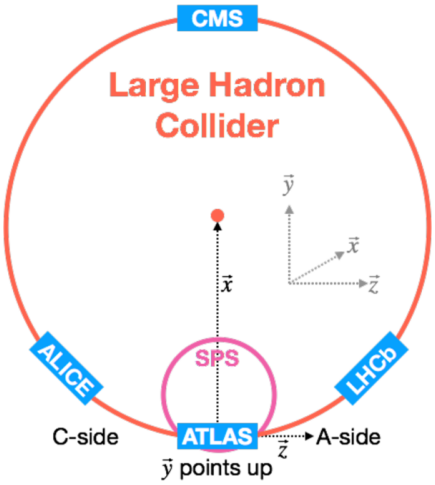

Figure 3.6: The coordinate system which is used in ATLAS.

primary and secondary vertices. The ID is located within a superconducting solenoid magnet which generates a 2 T axial magnetic field. The magnetic field bends the charged particle tracks, and the degree and direction of curvature can be used to measure the momentum and sign of the electric charge. The solenoid magnet is 5.8 m long with a 2.46 m inner diameter and 2.56 m outer diameter. The single-layer wound coil is made of Al-stabilised NbTi conductor and the nominal current is 7.73 kA. The ID is designed to be able to reconstruct a high rate of particles (up to 1000 every 25 ns) emerging from the collision point and passing through the acceptance region of $|\eta|<$ 2.5. The ID consists of three subdetectors: the Pixel detector and the SemiConductor Tracker (SCT) are the two innermost subdetectors, and contain fine granularity sensor channels for reconstructing particle tracks and vertices at high resolution. At larger radius, the Transition Radiation Tracker (TRT) contains its many layers of gaseous tubes. The locations of the three ID subdetectors in the barrel and end-cap are shown in Figure 3.7.

Pixel detector

The subdetector closest to the beam pipe is the pixel detector [63] which is split into barrel and end-cap regions. In the barrel there are three concentric cylindrical layers of silicon sensors placed at radii of 50.5, 88.5, and 122.5 mm. Each pixel of each silicon sensor forms a reverse-biased diode, and thus a small electric current is generated when a charged particle passes through the pixel. The innermost pixel layer in the barrel, the Insertable B-Layer (IBL), was in-

stalled at a radius of 33.2 mm during the first long shut-down (May 2014). The IBL has been operated successfully since the beginning of Run-2, and shows excellent performance: a low dead module fraction, high efficiency, and improved tracking capability. Providing additional hit information at the closest position to the beam collision point, the IBL significantly improves the performance of tagging a cone of particles that originated from a b-quark (is called b-jet). Three disk-like pixel detectors are located in the end-cap at different distances from IP (49.5, 58.0, and 65.0 cm). In total, there are around 80 million pixels, each with area $r\phi \times z = 50 \times 400$ μm^2 and each provides spatial resolution of $z = 115$ μm^2 and $r\phi = 10$ μm. All pixel layers in the barrel and end-cap are illustrated in Figure 3.8 and Figure 3.9.

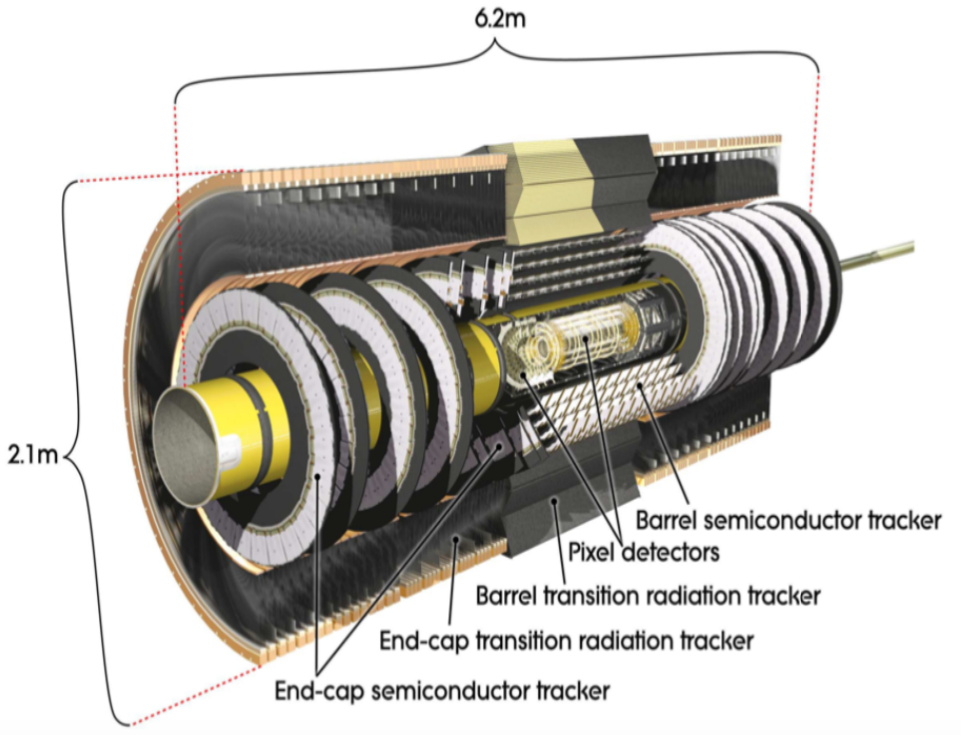

Figure 3.7: The ATLAS inner detector. Three subdetectors in the barrel and end-cap: a pixel detector, a semiconductor tracker, and a transition radiation tracker are shown. Figure from [50].

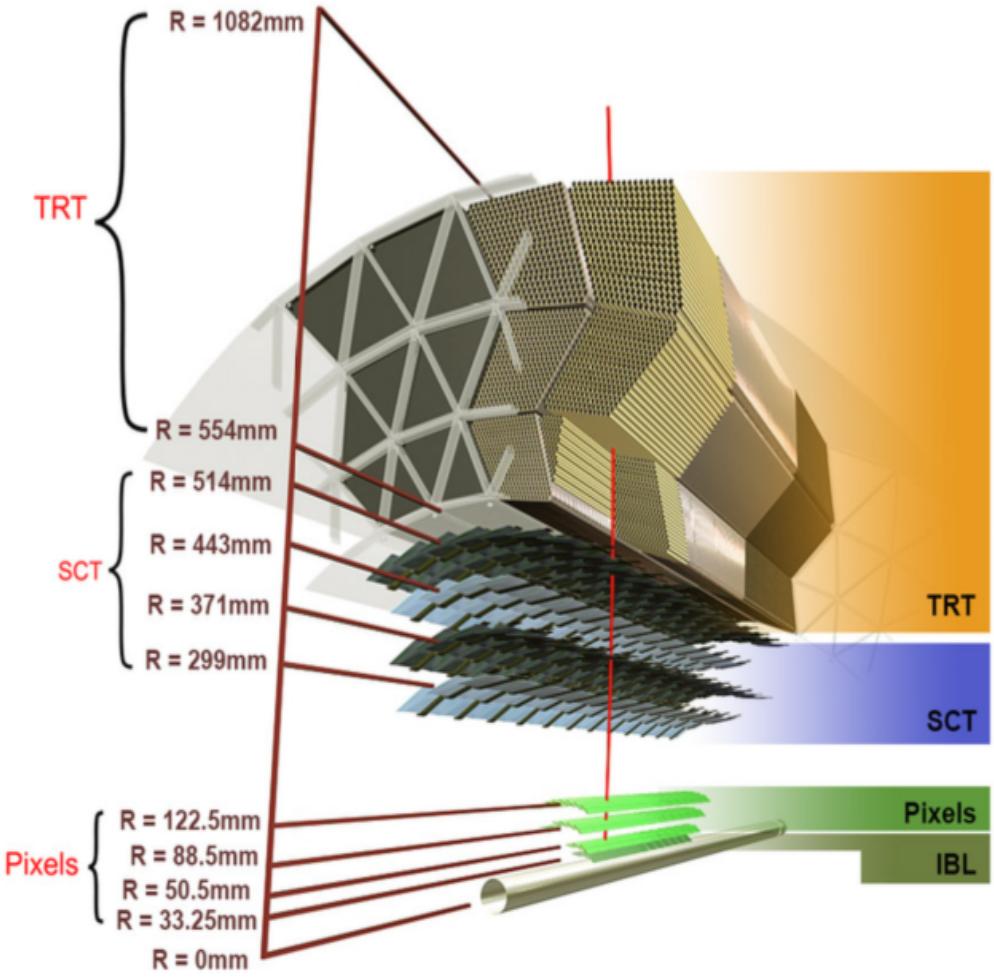

Figure 3.8: Cutaway diagram showing all barrel layers for the ATLAS inner detector. The red line corresponds to the trajectory of a charged track with $p_{\mathrm{T}} = 10$ GeV. The track traverses the beam pipe, three silicon-pixel layers, four cylindrical double layers of SCT, and approximately 36 straws of TRT modules [50].

Semiconductor tracker

Like the pixel detector, the semiconductor tracker [64] consists of multiple layers in both the barrel and the end-cap. In the barrel, the SCT consists of four cylindrical layers positioned at radii of 29.9, 37.1, 44.3, and 51.2 cm, and covers the region corresponding to $|\eta| < 1.4$. In the end-cap, there are nine disks installed at different distances from the IP, which provide coverage for $1.4 < |\eta| < 2.5$. To obtain high-precision tracking in the SCT, silicon strip sensors are each placed in back-to-back pairs, with an angle of 40 mrad between the sensor in each pair. By using this stereo angle, the SCT is able to additionally

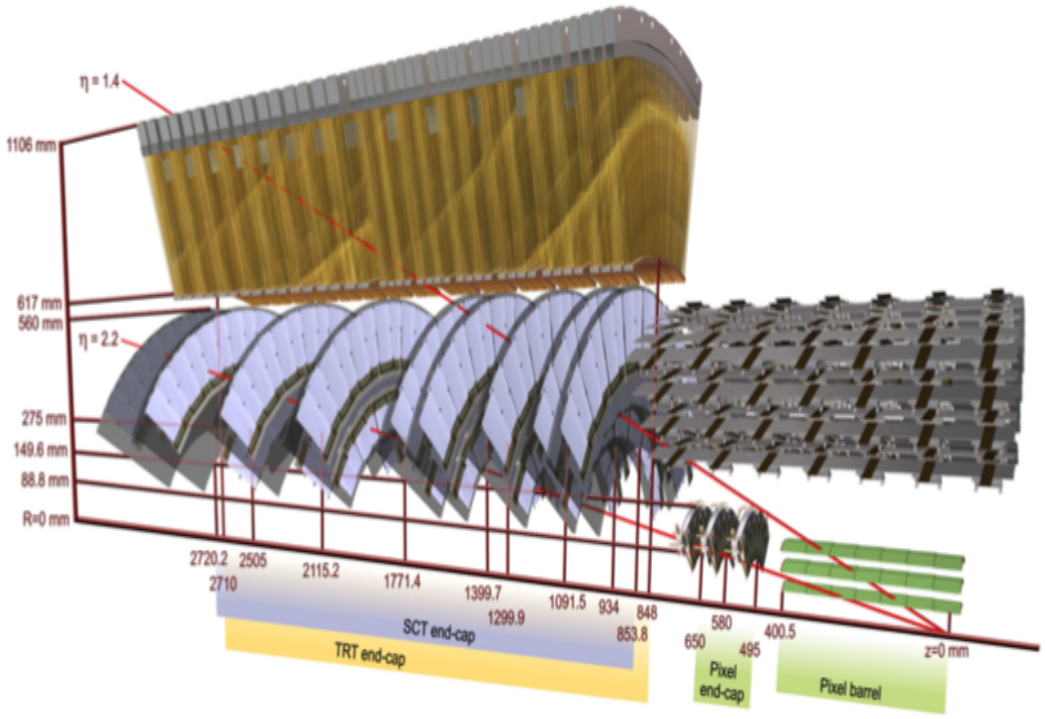

Figure 3.9: The ATLAS inner detector end-cap view. This shows the elements traversed by two charged tracks, both with $p_{\mathrm{T}} = 10$ GeV, in the end-cap ID at $\eta = 1.4$ and $\eta = 2.2$. As an example, the beam pipe, three pixel layers, four disk layers of SCT, and approximately 40 straws of TRT are the structures that the particle at $\eta = 1.4$ passes through. Figure from [50].

measure z coordinates in the barrel and r coordinates in the end-cap. The intrinsic resolution in the barrel is 17 μm in the transverse plane, and 580 μm in the longitudinal plane. The SCT layers are shown in Figures 3.8 and 3.9.

Transition Radiation Tracker

The outermost subdetector of the ID is the transition radiation tracker [61], TRT. The TRT covers the region of $|\eta| < 2.0$, and it consists of both barrel and end-cap modules. In the barrel, the TRT tubes are small-diameter drift tubes which are parallel to the beam direction. The tube walls (which form the cathodes) are coated with a conducting layer of "aluminum" and a gold-plated tungsten wire runs through the center of each tube as an anode. Each tube is normally filled with a gas mixture of 70% Xe, 27% CO_2, and 3% O_2. When a charged particle passes through the TRT, it ionizes the gas and produces negative charge electrons and xenon ions. A high voltage between the cathode and anode causes the electrons to drift to the anode wire, and the electronic

readout converts it to signal current. The strength of the current is a function of the velocity of the charged particle. The TRT provides track information on $r-\phi$ in the barrel and $z-\phi$ in the end-cap.

3.2.3 Calorimeters

The ATLAS calorimeters [65,66] (see Figure 3.10) cover the region $|\eta|< 4.9$, and they are primarily used to measure the energy of different types of particles. The calorimeter system consists of two subdetectors: the electromagnetic calorimeter (ECal) which is used for electron and photon reconstruction, and the hadronic calorimeter (HCal) which in conjunction with the ECAL provides accurate jet reconstruction and missing energy measurements. The sampling structure used for both ECal and HCal is similar. A sampling calorimeter uses the dense materials as the absorbers in order to reduce the particle energy, and active materials to provide detectable signal. When a high energy charged particle passes through the ECal, it loses energy in the absorber layers via *bremsstrahlung* [11] and produces a cascade of secondary particles. As an example, high energy electrons produce electromagnetic showers, which include many low energy electrons, positrons and photons. Then, the lower-energy secondary particles interact via ionization with the active layers producing signal for electronic readout channels. The amount of the signal indicates the energy of the primary particles (this also requires calibration of the measured energy by considering the calorimeter response [67]).

The calorimeter depth is an important criteria in order to maximize the containment, and to limit leakage outside the calorimeters. The ECal thickness in the barrel is $>$ 22 radiation lengths (X_0), and $> 24X_0$ in the end-caps. Radiation length X_0 is the distance which an electron or positron traverses through the matter in order to lose $1/e$ of its initial energy, and it depends on the characteristics of the material:

$$X_0(g/cm^2) \simeq \frac{716 \text{ g cm}^{-2}\ A}{Z(Z+1)\ \ln(287/\sqrt{Z})} \quad , \tag{3.7}$$

where Z and A are the atomic number and atomic mass of the material, respectively. In the HCal, the active calorimeter depths are approximately 9.7 interaction lengths (λ) in the barrel and 10λ in the end-cap (see Figure 3.11).

Interaction length is also material-dependent:

$$\lambda \approx 35 \text{ g cm}^{-2} \, A^{1/3} \quad . \tag{3.8}$$

Figure 3.11 shows that there are approximately two interaction lengths of material in front of the HCal (including the ECal and all materials in front of the ECal shown in beige). The full coverage in η (pseudorapidity, as shown or example in Figure 3.11) for the ID, the ECal, and the HCal provides high-precision measurements for the different types of incident particles.

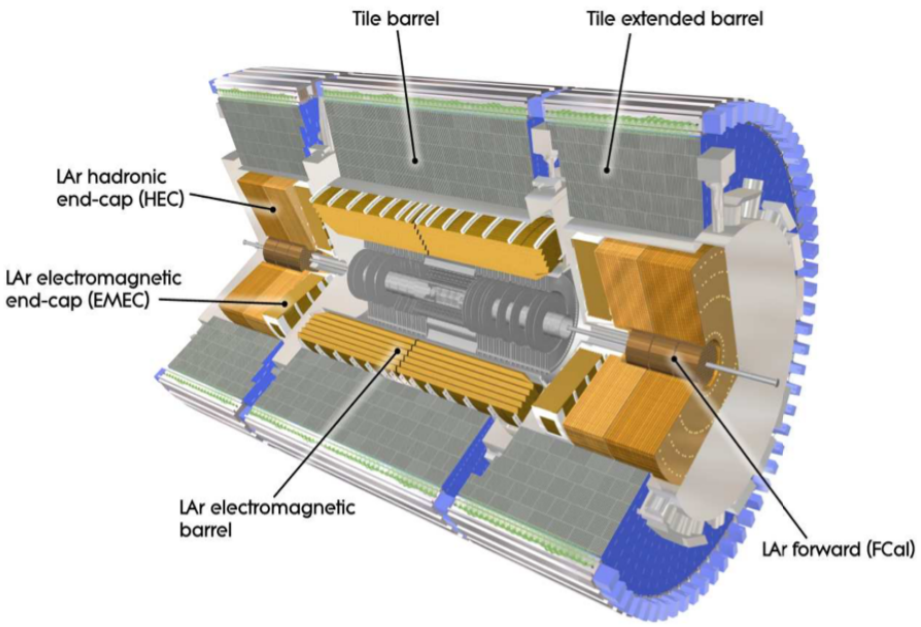

Figure 3.10: The ATLAS calorimeters: the electromagnetic calorimeter (ECal) and the hadronic calorimeter (HCal). The barrel and two end-cap modules for ECal use LAr as an active material. In the barrel of HCal, scintillating tile detector technology is used. In addition, the liquid argon forward (FCal) detector is designed to detect particles with large longitudinal momenta close to the beam. Figure from [50].

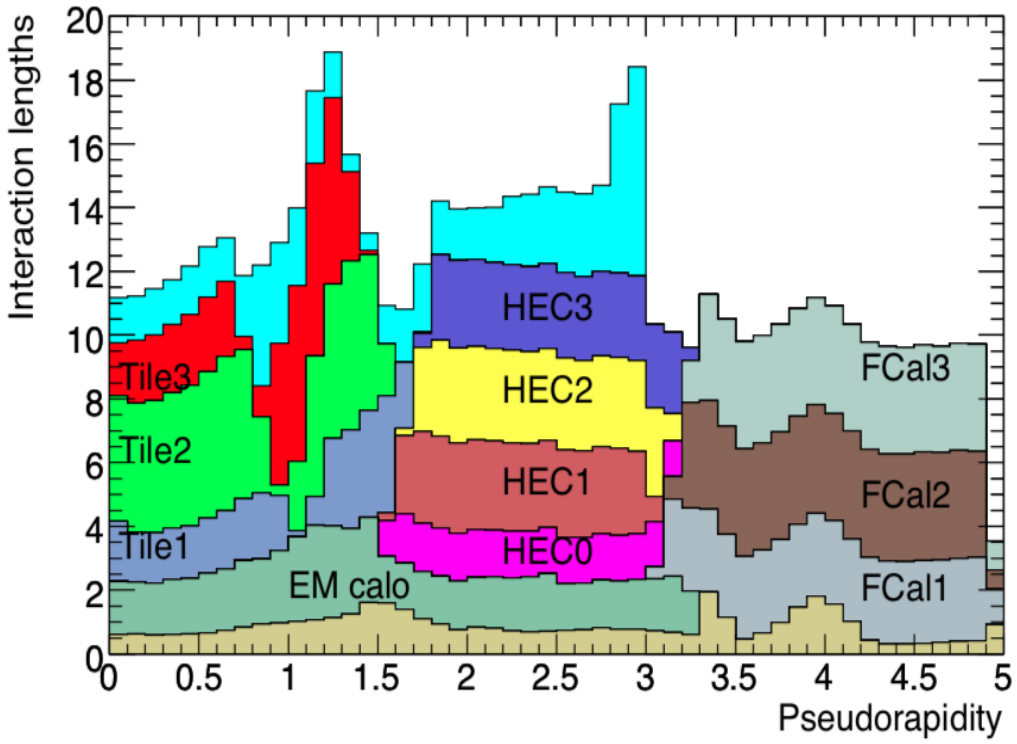

Figure 3.11: Cumulative amount of material, in units of interaction lengths, in front of the various calorimeters as a function of $|\eta|$. The beige colour at the bottom of the plot represents the total amount of material in front of the ECal, and for completeness the first active layer of the muon spectrometer is shown in cyan [50].

Electromagnetic calorimeter

There are three subdetectors within the electromagnetic calorimeter, the first one being the electromagnetic barrel, EMB, which covers $|\eta|< 1.47$, and the second and third being each of the two endcaps, EMEC (side A and C), covering $1.37 < |\eta|< 3.2$. Each of these subdetectors have accordion folded geometry to provide complete ϕ coverage (see Figure 3.12), and use liquid-argon (LAr) as the active material. The transition or crack region refers to the gap between the barrel and the end-cap where cables, gas and coolant tubing, and electronics are placed, and this reduces particle detection efficiency in that region. ATLAS physics analyses thus tend to avoid the crack region for object reconstruction.

Both EMB and EMEC are sampling calorimeters, composed of lead plates as the absorber and liquid argon as the active material. Electromagnetic showers initiate in the absorber, and then particles generated in the shower ionize the liquid argon, resulting in negatively charged electrons and positively charged ions. The electric current is induced by the movement of these free electrons

and are used to measure the energy of initial particles (which can be either electrons or photons). Copper electrodes are used in the readout channels for both barrel and end-cap in order to transmit the electric current.

The EM calorimeters are segmented into three layers with different granularity, as shown in Figure 3.13. The first layer, closest to the beam pipe, is finely segmented in pseudorapidity with $\Delta\eta \times \Delta\phi = 0.0031 \times 0.098$ granularity; the second layer collects the largest fraction of the energy of the electromagnetic shower with strips of $\Delta\eta \times \Delta\phi = 0.025 \times 0.025$, and the third layer collects only the tail of the electromagnetic shower and is therefore less segmented in pseudorapidity: $\Delta\eta \times \Delta\phi = 0.05 \times 0.0245$.

The LAr forward calorimeter, which has a module for EM calorimetry and two modules for hadronic calorimetry, will be discussed in Section 3.2.3.

Hadronic calorimeter

The hadronic calorimeter HCal is made of three subdetectors, including the tile calorimeter, the hadronic end-cap calorimeter HEC, and the forward calorimeter FCal. These three subdetectors are designed to measure the energy of

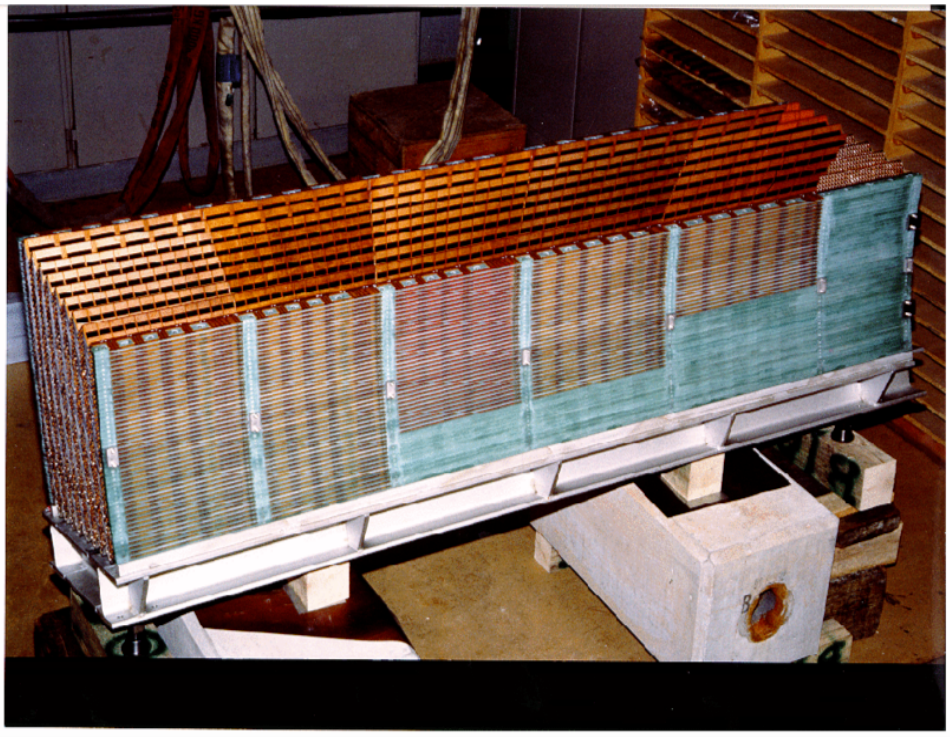

Figure 3.12: View of the electromagnetic calorimeter barrel showing the accordion geometry. Figure from [65].

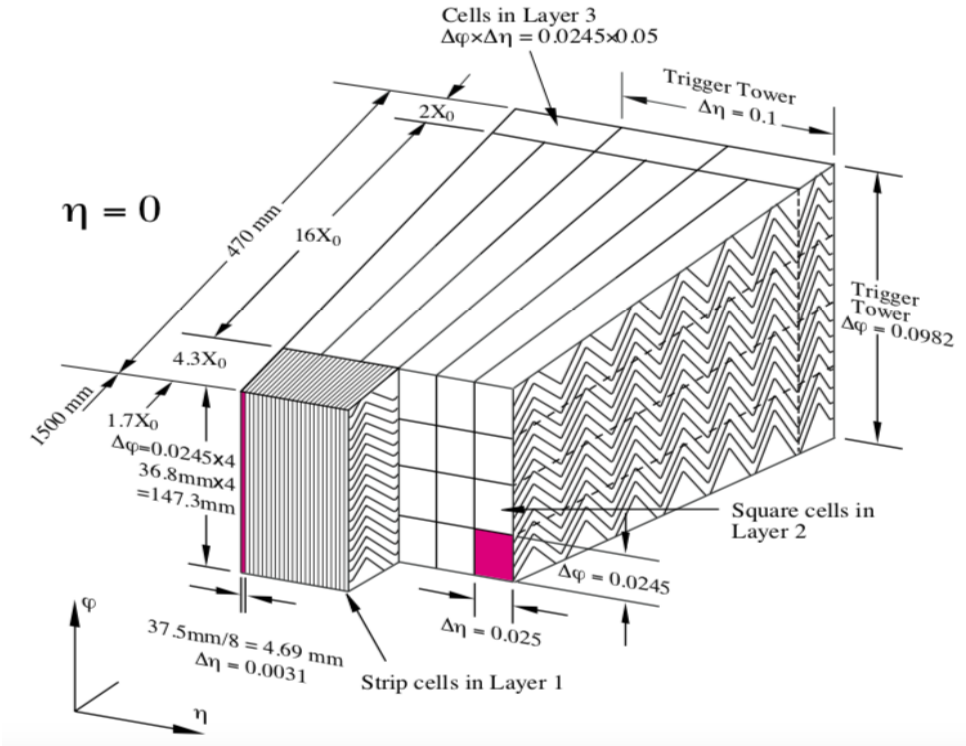

Figure 3.13: A sketch of an EMB module for layers 1, 2, and 3. Figure from [65].

hadrons, such as protons or neutrons.

The tile calorimeter is located directly outside the EM barrel calorimeter; its barrel covers the region $|\eta| < 1.0$, and its two extended barrels $0.8 < |\eta| < 1.7$. Steel is used as the absorber material, with layers of scintillating plastic tiles as the active medium, as shown in Figure 3.14. When a hadron passes through the tile calorimeter, it interacts with the atomic nuclei of the absorber and produces a shower of lower-energy secondary particles which traverse the scintillator, causing it to radiate light. Long fibers then carry the light to photomultiplier tubes (PMT) which convert the light signals into an electric current. Like the EM calorimeter, the tile calorimeter is segmented into three readout layers: in the first two layers, the cell geometry is approximately $\Delta\eta \times \Delta\phi = 0.1 \times 0.1$ and in the outermost layer, $\Delta\eta \times \Delta\phi = 0.2 \times 0.1$.

The HEC calorimeter is a liquid-argon cylindrical calorimeter which covers $1.5 < |\eta| < 3.2$. At the transition region between the end-cap and the forward calorimeter (around $|\eta| = 3.1$), the HEC extends to $|\eta| = 3.2$ to reduce the drop in material density. The same overlapping is valid between the HEC and tile calorimeter at $|\eta| = 1.5$. The HEC calorimeter is assembled into two independent wheels (per end-cap) and each wheel is built from parallel copper

plates, with LAr filling the gaps.

Forward calorimeter

The LAr forward calorimeter (FCal) is located close to the HEC ($3.1 < |\eta| < 4.9$), and provides uniformity of the calorimetric coverage as well as reducing background contamination in the muon spectrometer. The FCal has three modules: one for EM calorimetry and two for hadronic calorimetry. The first and innermost layer is made of copper and is optimized for EM measurements. The outer two modules are made of tungsten as the absorber and measure the energy of hadronic particles. All FCal layers can be seen in Figure 3.15. A shielding plug made of a copper alloy has been mounted behind FCal3 to reduce backgrounds in the end-cap muon system.

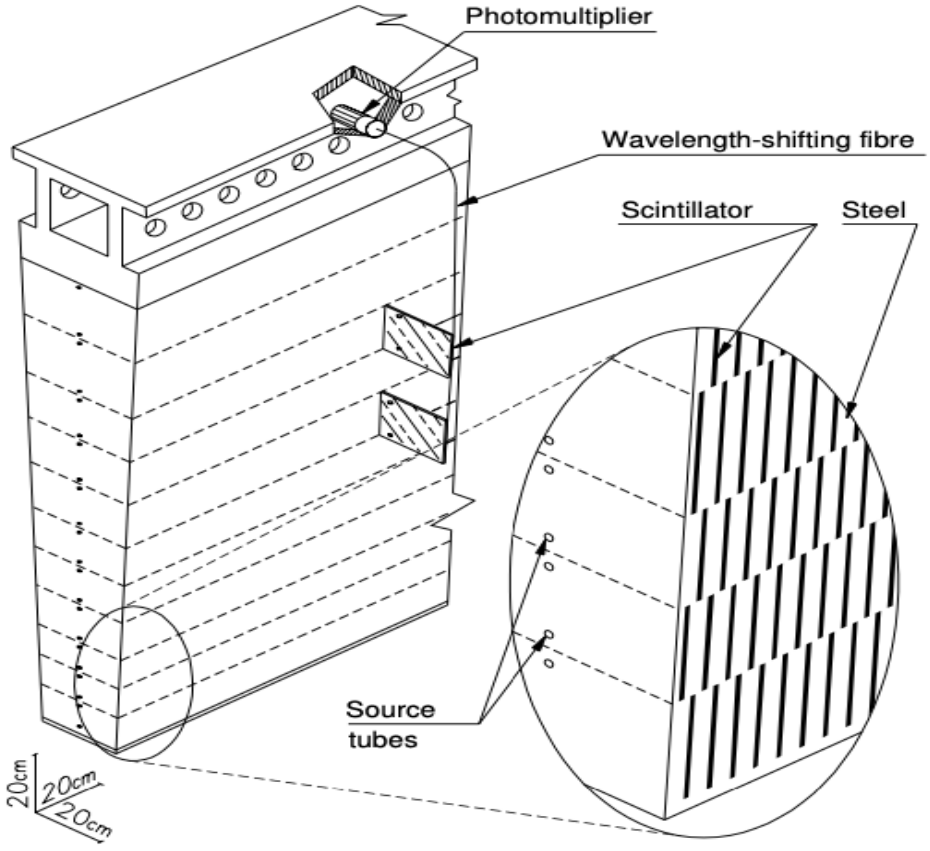

Figure 3.14: Sketch of a barrel module of the tile calorimeter. Figure from [50].

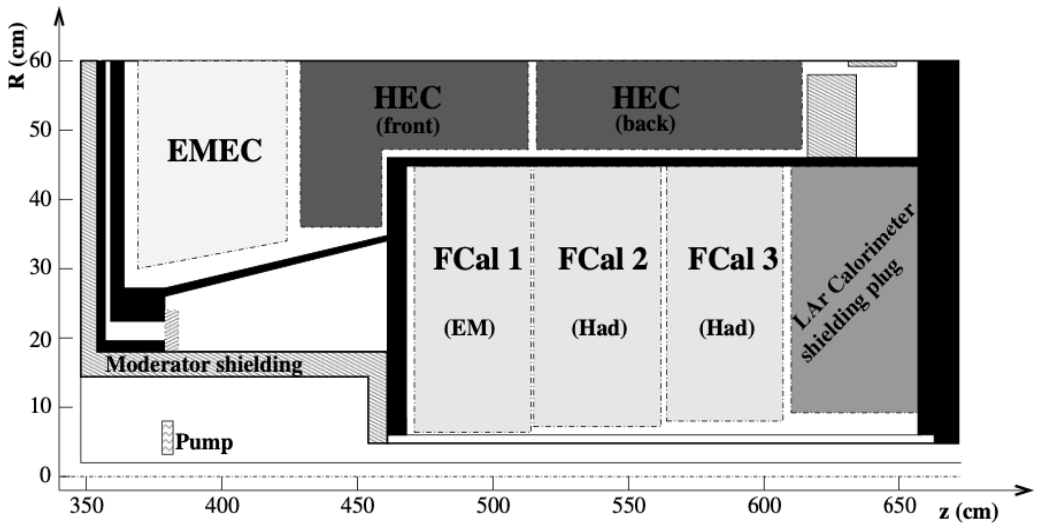

Figure 3.15: Sketch of the three FCal modules located in the end-cap cryostat. Figure from [50].

3.2.4 Muon spectrometer

The muon spectrometer (MS) [68] is the outermost region of the ATLAS detector, and provides muon momentum measurement in the pseudorapidity range $|\eta| < 2.7$ (illustrated in Figure 3.16). In the barrel (for $|\eta| < 1.7$), in order to measure the momenta of muons, the trajectories of the muons are bent by the magnetic field produced by eight superconducting air-core barrel toroidal magnets [69] as shown in Figure 3.17. For $1.6 < |\eta| < 2.7$, muon tracks are bent by two smaller toroidal end-cap magnets inserted into both ends of the barrel toroid. Over $1.4 < |\eta| < 1.6$, magnetic deflection is provided by a combination of the barrel and end-cap magnetic fields. The benefit of toroid magnets is to allow the production of a high magnetic field over a large volume with a reduced amount of material, which minimizes the resolution loss due to multiple scattering. The ATLAS toroid magnetic fields are roughly perpendicular to the trajectory of the incoming muons and the bending is in the $r - z$ plane.

The MS consists of four subdetectors dedicated to precise momentum measurement and triggering: monitored drift tubes (MDT) [70], cathode strip chambers (CSC) [71], resistive plate chambers (RPC) [72], and thin gap chambers (TGC) [73]. Momentum measurement is done by the MDT which, covers both the barrel and end-cap ($|\eta| < 2.7$) and also by the CSC in the end-cap region ($|\eta| > 2$). MDTs are drift cells with an aluminum tube filled with a gas mixture of Ar, N_2, and CH_4, and a cathode wire made of an alloy of tungsten

and rhenium (97%-3%). Conceptually, each MDT tube is fairly similar to a single tube of the TRT, which in this case means that muons ionize the gas atoms creating a cascade and then the electric current is fed into electronics. The CSCs are multi-wire proportional chambers located in the high η region of ATLAS where there is a large flux of particles. Drift time is shorter in the CSCs than in MDTs, which results in improved muon reconstruction efficiency in the forward region.

The ATLAS muon trigger systems must be capable of identifying events with high momentum muons with timing resolution that permits the identification of the LHC bunch-crossing, where the bunch crossings are spaced by 25 ns. In the barrel region, RPCs have been arranged in three layers outside the outermost layer of MDT and provide the ϕ coordinate (i.e., the non-bending direction) for the track. Three TGC layers are located in the region behind the first end-cap wheel to cover $1.05 < |\eta| < 2.4$ for triggering. The TGCs are multi-wire proportional chambers filled with a gas mixture of 55% CO_2 and 45% n-C_5H_{12}. The purpose of the chambers is to provide the second coordinate of the MDT measurement in the non-bending plane. The time resolution for the TGC is 1.5 ns (similar to the RPC) and it provides 2-7 mm spatial resolution.

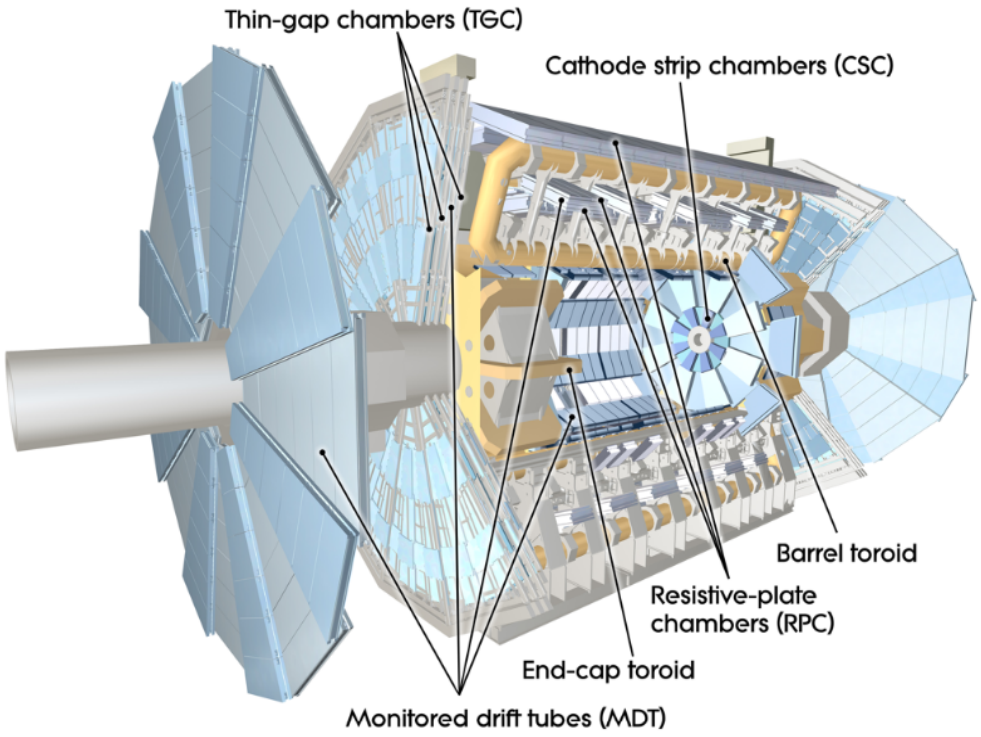

Figure 3.16: A cut-away view of the ATLAS muon system showing all major components: MDT, CSC, RPC, and TGC. Figure from [50].

Figure 3.17: Layout of the three types of magnets used in the ATLAS detector: the solenoid in the center, the two end-cap and the barrel toroids. Figure from [74].

Chapter 4

Triggering, Data, and Monte Carlo simulation

Prior to physics analyses, triggering and object reconstruction must be performed. The Trigger and Data Acquisition TDAQ system [75] in ATLAS is a crucial component of the ATLAS experiment, responsible for selecting events of interest at a recording rate of approximately 1 kHz from up to 40 MHz of bunch crossing collisions, corresponding to 25 ns bunch spacing of the LHC, and then save them to disk [76]. The recorded events are then analyzed offline to reconstruct different physics objects such as jets and missing transverse energy, which are used in ATLAS analyses. This chapter provides a brief introduction to the TDAQ system, ATLAS data, event-simulation process. Object reconstruction will be discussed in Chapter 5.

4.1 The TDAQ system

The LHC is designed to collide each of the 2808 proton bunches per beam in each of the two rings at a nominal rate of 40 MHz. During Run 1, the trigger system of the ATLAS detector operated at an instantaneous luminosity of 8×10^{33} cm^{-2}. At the start of Run 2, both the center of mass energy and instantaneous luminosity increased, and this requires a more efficient trigger system to keep the saved event rate low enough, but to save as many as possible rare hard scattering events to disk.

4.1.1 Level-1 trigger

Figure 4.1 represents the TDAQ system, which consists of two levels: the L1 hardware-based trigger [77], and the software-based high-level trigger (HLT) [78]. The L1 trigger uses information from the calorimeter detectors (L1Calo) and the muon spectrometer (L1Muon) - mainly from the RPCs and the TGCs - to choose interesting events. The L1 trigger decision is made by the Central Trigger Processor (CTP) [79] which works at a maximum rate of 100 kHz. It searches for a variety of signatures from high p_{T} muons, electrons, photons, jets and events with large missing transverse energy $E_{\mathrm{T}}^{\mathrm{miss}}$. For those events passed by the CTP, which are called L1 accept (L1A) events, the L1 trigger defines one or more Regions-of-Interest (ROI), which include information on the geographical coordinates η and ϕ, type of feature identified, and the threshold passed. Those ROIs are subsequently passed to the HLT for improved reconstruction, and further event rate reduction. The two analyses in this thesis contain a large number of jets (which can be b-tagged jets) and missing transverse energy, and thus more details are provided below about the L1Calo trigger system.

L1 Calo trigger

In order to identify high transverse energy electrons, photons, taus, and jets, the L1Calo searches for electromagnetic and hadronic energy deposits. The L1Calo receives analogue signals (from one or more of 7000 trigger towers of granularity $\Delta\eta \times \Delta\phi = 0.1 \times 0.1$) in both the electromagnetic and the hadronic calorimeters. The preprocessor system [80] then digitizes and calibrates the analogue input signals, and then transfers the output to the Cluster processor (CP) and Jet/energy processor (JEP) subsystems. An example of electromagnetic and hadronic trigger towers used in the electron/photon and the tau cluster algorithm in the CP and the jet algorithm in the JEP are shown in Figure 4.2. These trigger towers are classified as [81]:

1. For measurement of the transverse energy of the electromagnetic showers: neighboring pairs (in the radial direction) of towers, shown as green boxes;
2. For isolation in the electromagnetic calorimeter, twelve electromagnetic towers (shown in yellow);
3. Four hadronic towers (in red) behind the electromagnetic core for transverse energy measurement of the hadronic showers; and

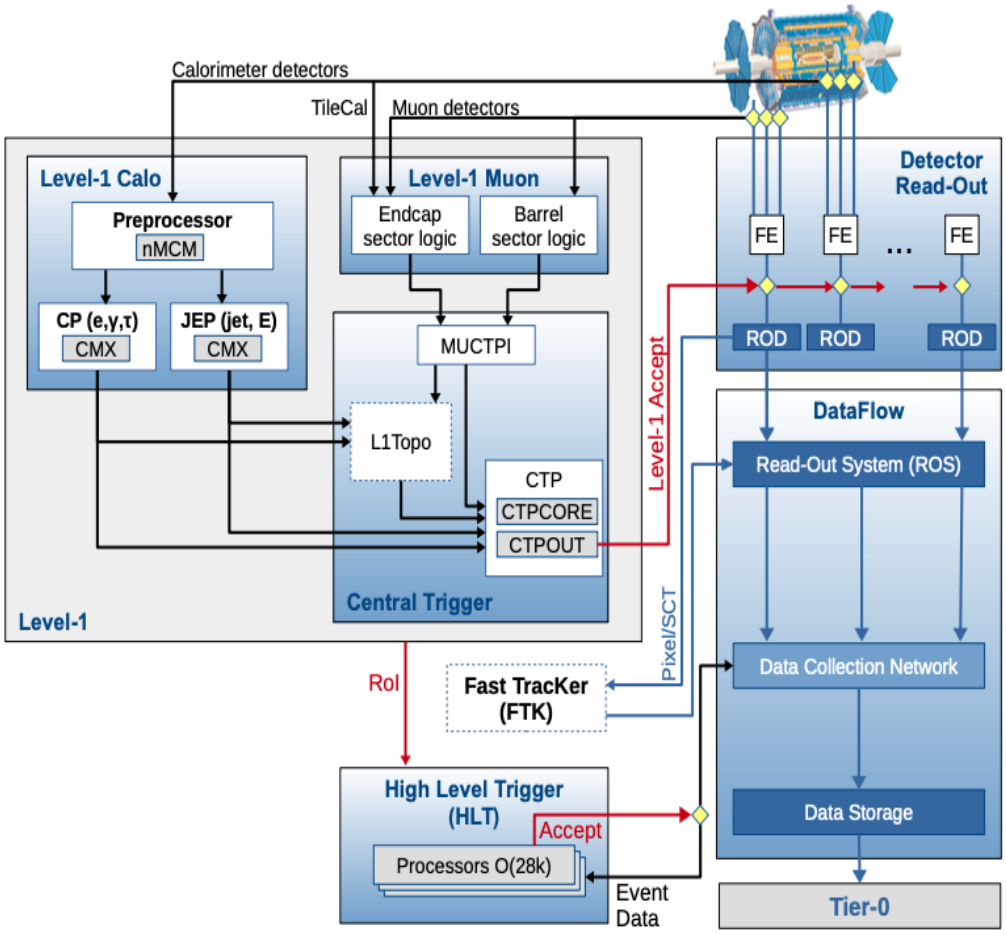

Figure 4.1: Run 2 ATLAS TDAQ system. The relevant components for triggering are: the Level-1 trigger (L1), and the High-Level Trigger (HLT). Figure from [75].

4. Twelve hadronic towers (in purple) provide a hadronic isolation ring for isolation in the hadronic calorimeter.

The CP uses a sliding window algorithm, and it identifies a 2×2 cluster of electromagnetic or hadronic trigger towers which exceeds a pre-defined threshold. At this point, other isolation-veto cuts can be set on those electromagnetic/hadronic isolation rings.

The inputs for the JEP algorithm are jet elements, which are the sum of 2×2 electromagnetic trigger towers and 2×2 hadronic trigger towers. The JEP performs a search to identify 4×4 or 8×8 trigger tower windows where the sum of electromagnetic and hadronic transverse energy exceeds a predefined threshold.

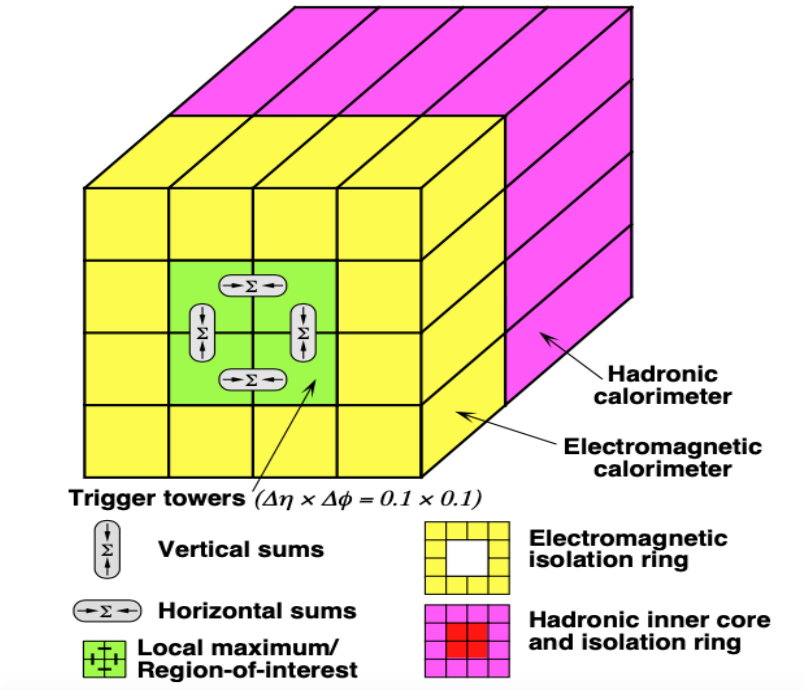

Figure 4.2: Sketch of the calorimeter trigger towers used as input to the CP and JEP algorithms to identify triggerable objects. Figure from [75].

4.2 High Level Trigger

After an L1A acceptance, the events (or rather, more specifically in this context, the ROI) are sent to the HLT for further reduction. The HLT uses finer granularity information from the calorimeters, tracking information from the ID (which was not available in L1), and tracking measurements from the MS. In Run 1, the HLT used two separate approaches for event reconstruction: a fast algorithm (L2 trigger) to reject the majority of events, and a slower precision Event Filter reconstruction for the remaining selected events. In Run 2 these two steps have been merged, in order to have a consistent setup, as well as no HLT-based rate limitation (at present LHC luminosity levels). The HLT reduces the event rate to about 1 kHz and sends the accepted events to the data collection network. Since trigger settings are not changeable during data taking runs, a prescale factor can be used to reduce output rate. A prescale factor (PS) is a number applied at L1 and/or at the HLT to determine the fraction of triggered events that will be recorded. In the analysis described in Chapter 6, the $E_{\mathrm{T}}^{\mathrm{miss}}$ trigger applied for both the 0-lepton and 1-lepton channels is unprescaled (PS = 1).

4.3 ATLAS Data

The LHC delivered 156 fb^{-1} of proton-proton collision data during Run 2 in the years 2015-2018, and the ATLAS detector recorded 147 fb^{-1} of these events, as shown in Figure 3.2b. ATLAS recorded data is divided into *runs*, which each have a unique six-digit identifying number referring to the time interval of data collection (which typically lasts for multiple hours). Then each run is further split into *luminosity blocks* (LB) representing data collection over a minute. The LB is the standard unit of granularity for data quality book-keeping [82, 83].

ATLAS analyses use collections of run numbers (*periods*) which include details on the LHC and ATLAS conditions like the luminosity or bunch spacing. For each period, data quality experts provide a list – the so-called Good Runs List (GRL) – that contains the list of certified LBs in a set of of files with XML format. Data quality monitoring checks the LHC status, and for existence of electronic noise or high voltage trips in modules and other such defects. LBs collected during problems such as those are excluded from the GRL. ATLAS data quality efficiency increased between 2015 and 2018 due to continuous detector maintenance and software development. Figure 4.3 shows the data quality in ATLAS between 2015 and 2018.

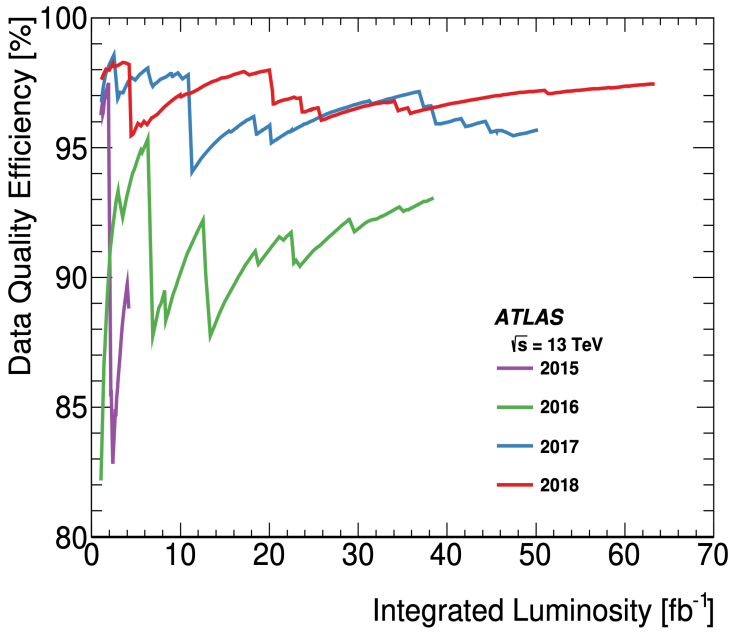

Figure 4.3: Data quality efficiency versus total integrated luminosity delivered to the ATLAS detector between 2015 and 2018. Figure from [82].

4.4 Monte Carlo Simulation

4.4.1 Proton-proton Interaction

All background and signal Monte Carlo (MC) samples in this analysis are generated based on the simulation of inelastic proton-proton collisions and the ATLAS detector response. The proton is made of partons: three valence quarks (two up and one down), gluons, and "sea quark" pairs of quarks and antiquarks of all flavors. Since protons are not fundamental particles, the proton-proton collision is a collision of partons, which have different momentum distributions [84]. These parton distribution functions (PDFs), which are functions of the fraction x of the proton's momentum carried by the parton, and also of the squared energy scale Q^2 of the proton interaction, can then be used to derive production cross-sections for different final states in terms of the subprocess cross-section [85]:

$$\sigma(pp \to X) = \sum_{q,\bar{q},P} \int dx_q dx_{\bar{q}} f_{q/P_1}(x_q, \mathrm{Q}^2) f_{\bar{q}/P_2}(x_{\bar{q}}, \mathrm{Q}^2) \hat{\sigma}_{q\bar{q}} \quad , \tag{4.1}$$

where q and $\bar{q}$ are all possible partons, $\hat{\sigma}_{q\bar{q}\to X}$ is the partonic cross-section, and $f_{q/P_1}(x_q, \mathrm{Q}^2)$ and $f_{\bar{q}/P_2}(x_{\bar{q}}, \mathrm{Q}^2)$ are the PDFs of parton q in proton P_1 and for parton $\bar{q}$ in proton P_2 respectively. PDFs need be determined experimentally, since there is no theoretical prediction for the PDFs as function of x. However, equations independently derived by Dokshitzer [86] - Gribov and Lipatov [87] - Altarelli-Parisi [88], known as DGLAP, can be used to evaluate PDFs at different Q^2 squared energy scales. In Figure 4.4, representations of two PDF sets at the next-to-leading order for $Q^2 = 10$ GeV^2 and $Q^2 = 10^4$ GeV^2 are plotted. At low x, gluons and sea quarks receive the majority of the total momentum (and this increases with Q^2). On the other hand at, high x values, the PDF of valence quarks (u_v and d_v in the plot) are dominant, which is consistent with the parton model [89]. In the high energy regime shown in Figure 4.4b, heavy flavor quarks (b and c) obtain larger momentum fractions and appear more readily in collisions.

In Figure 4.5 two colliding protons (green ellipses with left and right arrows) interact via partons (gluons, quarks, or antiquarks) at the hard scattering point (red circle). The partons produced in the hard scatter process lose energy by QCD radiation, and the resulting gluons can split into quark-antiquark pairs. This cascade of radiation is called parton showering and is shown by red lines.

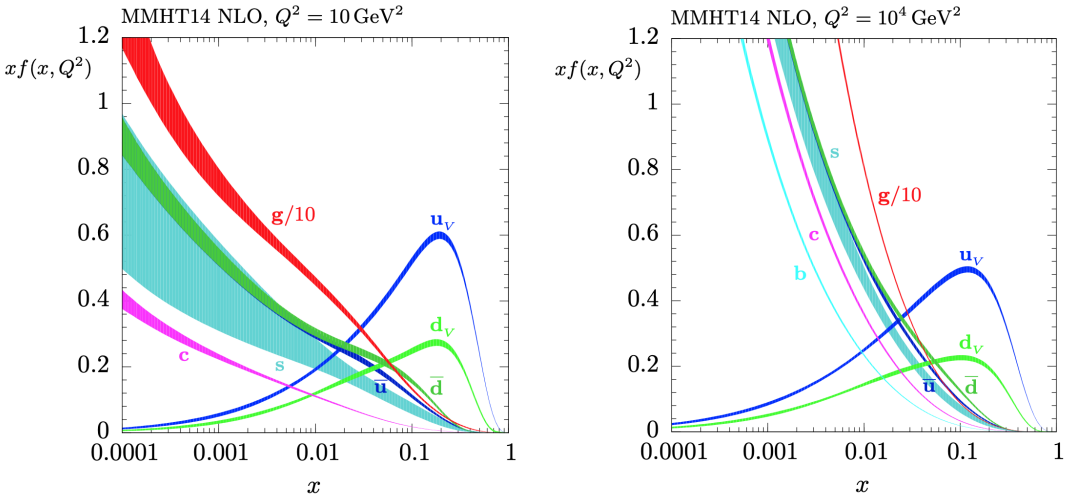

(a) $Q^2 = 10$ GeV^2 (b) $Q^2 = 10^4$ GeV^2

Figure 4.4: MMHT14 (Martin, Motylinski, Harland-Lang, Thorne) NLO PDFs for $Q^2 = 10$ GeV^2 (left) and $Q^2 = 10^4$ GeV^2 (right). The vertical axis represents the parton's PDF multiplied by x. Figure from [90].

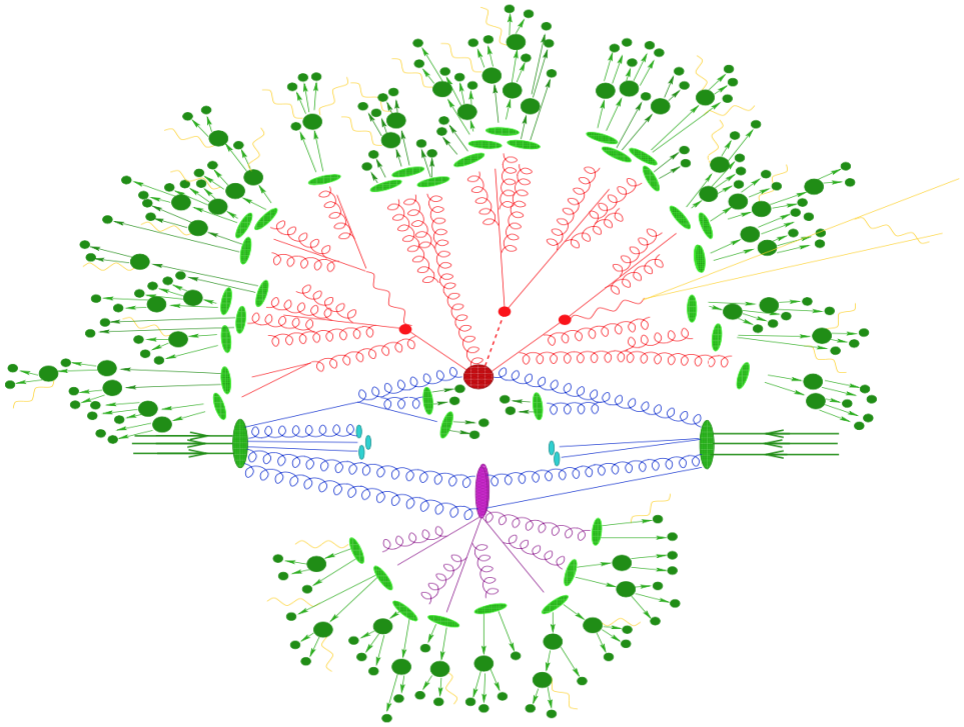

Figure 4.5: Representation of an MC simulation of a pp collision involving hard scattering, parton showering, hadronization, and the underlying events. Figure from [91].

The final gluons and quarks subsequently hadronise into stable final states such as mesons (green circles). The other partons not involved in the hard scattering may interact and undergo the process referred to as the underlying event UE (purple ellipse). Beam remnants (small blue ellipses) and soft photon radiation at parton shower level (yellow lines) are the other possible components of proton-proton collision events.

4.4.2 ATLAS Event Simulation

The comparison of ATLAS detector data with Monte Carlo (MC) simulation is one of the most important parts of every ATLAS analysis. MC is used to help calibrate the ATLAS detector, to make predictions for the types and amounts of background in signal regions, and to estimate experimental and theoretical uncertainties. The three main steps in the simulation of an event in ATLAS are explained below:

Monte Carlo Generation

The first step to produce ATLAS MC samples is to generate proton-proton collisions, which consists of determining the following:

1. Matrix element (ME) or amplitude: For each process of interest such as $p_i p_j \rightarrow X$ (two partons in the initial state interact and produce a final state consisting of X) the matrix element $\mathcal{M}$ at a given order in QCD and QED should be computed. Leading order (LO) and Next-to-leading order (NLO) represent sets of Feynman diagrams used in the ME calculation [92]. Higher-order corrections can change the overall normalization of cross-sections, and also change kinematic distributions, which may (for example) make various final state transverse momentum spectra harder or softer. There are several generators available to provide a full ME computation such as MADGRAPH5 [93], POWHEG [94], and SHERPA [95].

2. Parton shower: The partons produced in the hard scattering have a large momentum transfer and, similar to QED radiation by accelerated electrons, partons will emit QCD radiation. Then, gluons which carry colour charges can pair-produce into quark-antiquark pairs $g \rightarrow q\bar{q}$, or pair-produce into other gluons $g \rightarrow gg$ to emit further radiation known as parton showers. From the Sudakov form factor [96] we find that the probability for a parton to loose energy and evolve from scale q_1^2 to q_2^2 is given

by:

$$\Delta_i(q_1^2, q_2^2) = \exp\left\{ -\int_{q_1^2}^{q_2^2} \frac{dq^2}{q^2} \frac{\alpha_s}{2\pi} \int_{Q_0^2/q^2}^{1-Q_0^2/q^2} dz \int_0^{2\pi} d\phi P_{ji}(z,\phi) \right\} \quad . \quad (4.2)$$

Here, α_s is the strong coupling constant, $q^2 = Q_0^2 \approx 1$ GeV^2 is the hadronization scale, and $P_{ji}(z,\phi)$ represents the splitting function for $i \to j$ which describes the probability that the parton j carries a fraction z of the momentum of parton i . The sequence of parton showering is terminated when the hadronization scale is reached.

3. Hadronization: As described in subsection 2.1.4, the strong coupling constant α_s is scale dependent, which specifically means that at the hadronization scale, it reaches a large value. Thus, at this scale, perturbation theory is not valid anymore, and the effect of QCD confinement implies that low energy coloured partons become bound within color singlet hadrons. There are two hadronization models which are used in both the PYTHIA [97, 98] and HERWIG++ [99, 100] generators. The first one is the string model [101] which is based on quark-antiquark confinement. A good example is quark-antiquark pair production in electron-positron annihilation, as sketched in Figure 4.6. At the annihilation point, the quark and antiquark move apart from each other. As the gluonic string between them is stretched, its potential energy is increased. When the potential energy gets close to the hadron masses, it is highly probable for the string to be broken and a new quark-antiquark pair to be created. The new quark forms a bound state with the original antiquark and the new antiquark connects to the original quark. Further stretching and breaking are possible until all the energy of the system converts into quark-antiquark pairs, which are represented as hadrons.

   The second method is the cluster [102] model which is based on QCD preconfinement. It is assumed that at an evaluation scale q, where q is less than the hard subprocess scale, partons created in the shower can combine and form colour-singlets (clusters) with an invariant mass distribution depending on q. Then, all produced clusters decay into observed hadrons as shown in Figure 4.7.

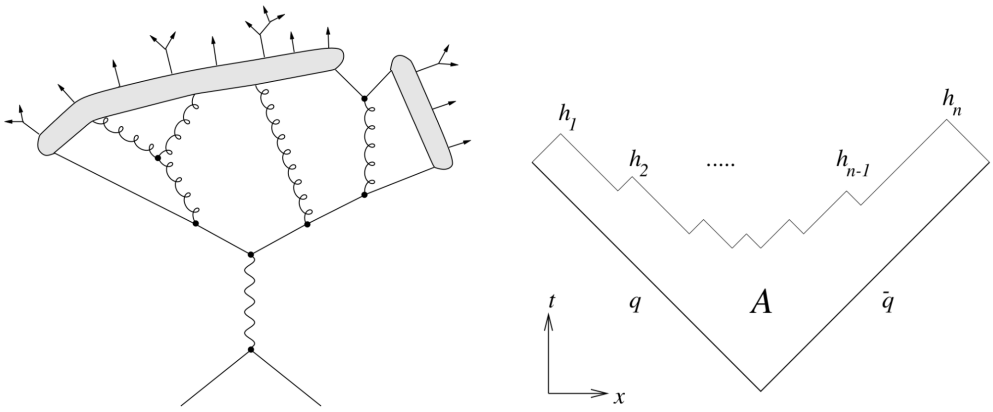

(a) (b)

Figure 4.6: String hadronization model (a) and a schematic view of the space-time picture of the string model (b). Figure from [102].

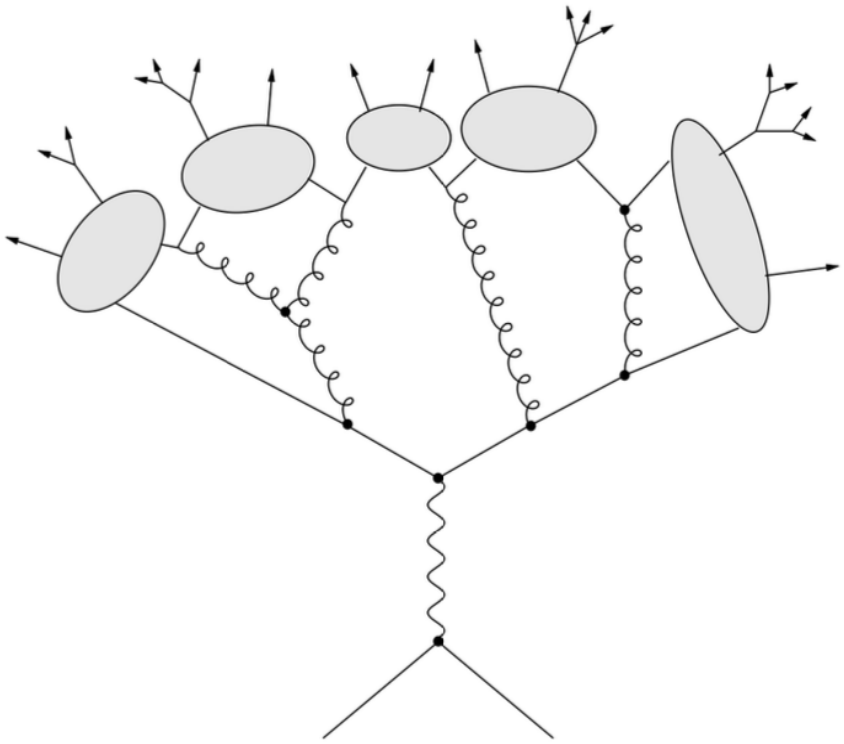

Figure 4.7: Cluster hadronization model. Figure from [102].

Detector Simulation

The next stage in event production is the simulation of the ATLAS detector, which is based on the GEANT4 [103] simulation tool. All four-vectors of final state particles simulated in the previous step pass through GEANT4 as inputs, to model the passage of particles through the detector. All known interactions between particles and the detector materials are simulated, and the resulting energy depositions are recorded as *Hits*. Finally, these hits from hard scattering or pileup are used as inputs for the digitization step, in order to produce simulated detector signals.

Reconstruction

The last step in MC generation is the reconstruction of physics objects such as electrons, muons, and jets from detector signals simulated by GEANT4. Direct comparison is possible between reconstructed analysis data and MC samples, because the same reconstruction software is used on both data and MC. Some examples of reconstruction of physics objects are provided in Chapter 5.

Chapter 5

Object Reconstruction

After ATLAS trigger acceptance, the physical objects in an event are reconstructed from the calorimeter cell energy deposits and the hits from charged particle passage through the inner detector or muon spectrometer. This chapter describes the reconstruction process for different objects used in the data analysis documented in this dissertation such as: jets, leptons, tracks, and missing transverse momentum. Once particles are reconstructed, the energy and momentum of these objects are calibrated to a particular energy scale.

5.1 Inner detector tracks and primary vertices

Tracks are reconstructed from charged particles with $p_{\mathrm{T}} > 0.4$ GeV and $|\eta| < 2.5$ using information provided by the ID. The ID of the ATLAS experiment is responsible for measuring such tracks (charged particle trajectories), and thus the momentum and impact parameters of charged particles. The impact parameters are defined as transverse and longitudinal distances of closest approach to a reference point [104] and are shown in Figure 5.1.

Track reconstruction in the pixel and SCT detectors starts by defining clusters from the raw data (electric charges and currents). A connected component analysis (CCA) [105] groups pixels and strips in a sensor with energy deposits that are above threshold into clusters. Figure 5.2 shows single-particle clusters which are created by energy deposits from individual charged particles. These clusters then can be used to create three-dimensional *space-points* which represent the centroids of the small regions through which the charged particle traverses the active material in the pixel and SCT subdetectors. A set of three space-points form a track seed with a purity that depends on which sub-detectors recorded

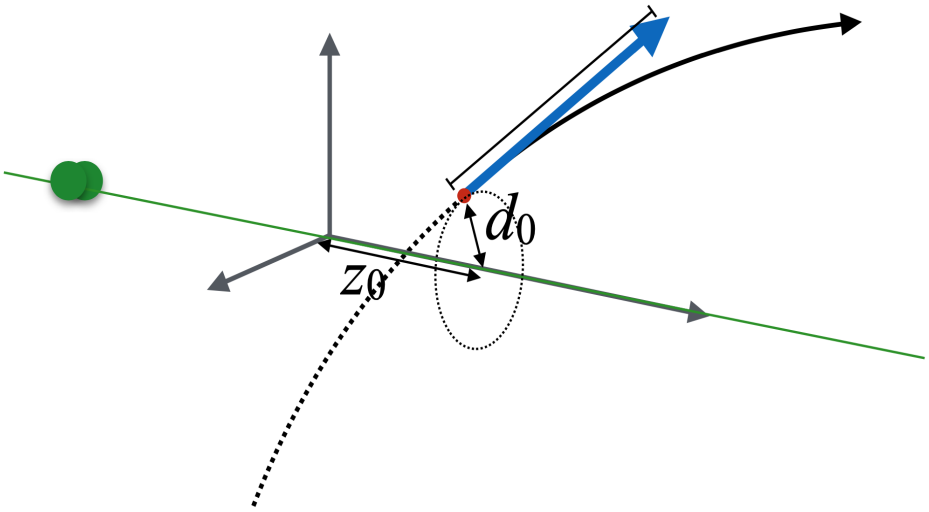

Figure 5.1: Sketch of the transverse (d_0) and longitudinal (z_0) impact parameter in the ID.

those space-points. Additional space-points from outer layers of the ID compatible with the preliminary trajectory are added using a combinatorial Kalman filter [106, 107] to build track candidates.

To study track reconstruction efficiency, two quality criteria (Loose, and Tight-Primary) are used for data collected in 2015 and 2016. These working points have different requirements on the number of hits (energy deposits that are read out in the ID) and holes (missing hits on a track) in different ID layers. The tracking efficiency $\epsilon_{track}(p_{\mathrm{T}}, \eta)$ is first estimated from MC simulation using the following definition:

$$\epsilon_{track}(p_{\mathrm{T}}, \eta) = \frac{N_{\mathrm{rec}}^{\mathrm{matched}}(p_{\mathrm{T}}, \eta)}{N_{\mathrm{gen}}(p_{\mathrm{T}}, \eta)} \quad , \tag{5.1}$$

where $N_{\mathrm{gen}}(p_{\mathrm{T}}, \eta)$ is the total number of generated charged particles, and $N_{\mathrm{rec}}^{\mathrm{matched}}$ is the reconstructed track number matched to a truth charged particle. The track reconstruction efficiency for both Loose and Tight-Primary is shown in Figure 5.3 as a function of p_{T} and η. Tracking efficiency reaches a plateau above $p_{\mathrm{T}} > 5$ GeV and is slightly reduced in the region $|\eta| > 1$ because of the increasing amount of material that the particles traverse. The tighter selection used at the tight working point reduces the percentage of fake tracks, at the expense of lower tracking efficiency.

One of the most important elements of this as well as many other ATLAS data analyses is the reconstruction of primary vertices (PVs) as the points

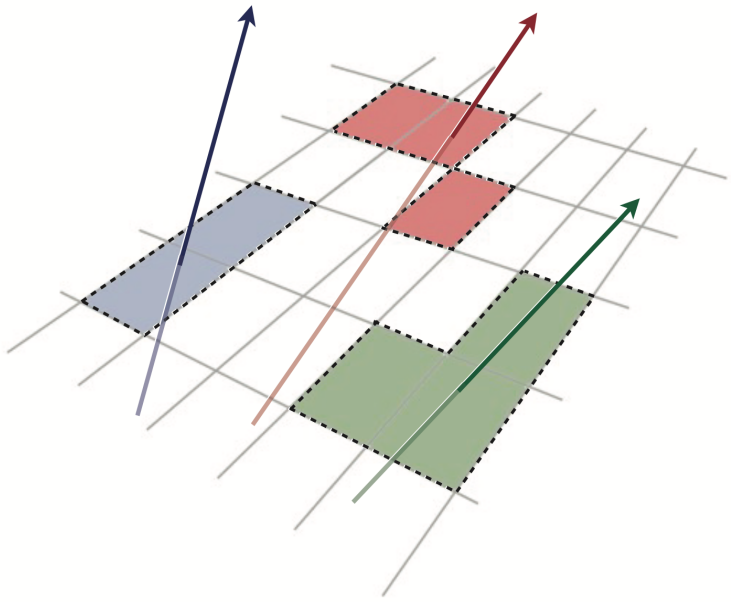

Figure 5.2: Schematic view of single-particle pixel clusters. Energy deposits from different charged particles are shown with different colours [105].

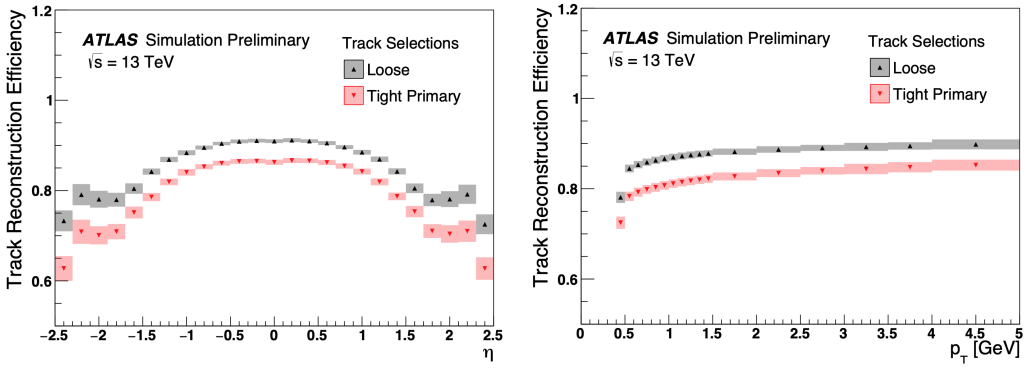

(a) (b)

Figure 5.3: Track reconstruction efficiency for Loose and Tight Primary selections as a function of η (a) and p_{T} (b). Figure from [104].

where two protons scatter. The input for the vertex reconstruction is the full set of tracks in the ID. Tracks used in PV reconstruction must pass requirements including a minimum p_{T} and a minimum number of hits in silicon and pixel layers. The PV reconstruction consists of two steps: vertex finding [108] and vertex fitting. In vertex finding, seed positions for the initial vertices are determined using the set of tracks passing the selections. In vertex fitting, the seed positions and the tracks are used in least-squares fits to find the best vertex positions. Once all the PV are reconstructed, the hard scattering PV is

defined as the one with the highest fraction of track Σp_{T}^2. The remaining PVs are called pileup vertices, which usually come from soft-QCD interactions.

5.2 Jets

Strongly interacting particles produced in a collision (like quarks and gluons) hadronize, and the shower of particles is reconstructed experimentally as a jet. Jets interact with the detector and the resulting energy deposits can be used to determine the properties of the original parton jet.

5.2.1 Jet reconstruction algorithms

Showers of particles lose energy in the calorimeter, and the signal is read out from each active layer cell. Then the cell signal significance $S_{\mathrm{cell}}^{\mathrm{EM}}$ is defined as the ratio of the cell signal $E_{\mathrm{cell}}^{\mathrm{EM}}$ to the average noise $\sigma_{\mathrm{noise,cell}}^{\mathrm{EM}}$ [109]. The cell noise originates from the EM noise and also from fluctuation due to pileup. Cell significance is the main key in the formation of topo-clusters through the application of a growing-volume algorithm. First, primary seed cells are built from cells with significance greater than 4σ. The growing-volume procedure starts with those seed cells, and adds "seed daughter" cells to a given topo-cluster which both neighbour the seed cell and which have significance greater than 2σ. Finally, all cells which neighbor a seed daughter cell and which have positive significance are included to reconstruct topo-clusters.

Topo-clusters are the input for different jet reconstruction algorithms such as the k_{T} family. The application of these successive algorithms is summarized into two steps:

1. For each topo-cluster i, a cluster-beam distance is defined as:

$$d_{iB} = p_{T,i}^{2P} \quad , \tag{5.2}$$

where p_T is the transverse momentum of the cluster, and P corresponds to the type of algorithm which is applied. For each pair of topo-clusters (i, j), we define the cluster-distance,

$$d_{i,j} = min(p_{T,i}^{2P}, p_{T,j}^{2P}) \frac{\Delta_{i,j}^2}{R^2} \quad , \tag{5.3}$$

where $\Delta_{i,j}^2 = (y_i - y_j)^2 + (\phi_i - \phi_j)^2$ [1], and R is a parameter which sets the

[1] Differences in rapidity y (Equation 3.5) are Lorentz invariant under boosts along the beam axis.

size of the jet. Typical values for R are $R = 0.4$ for small radius jets, and $R = 1.0$ for large radius jets.

2. For each topo-cluster i, if $d_{iB} > d_{i,j}$ for any other topo-cluster j, both clusters are merged, otherwise i is called a jet and it is removed from the list of entities. This procedure is repeated until no topo-clusters are left.

The value of P in equation 5.2 and 5.3 corresponds to the jet reconstruction algorithm that is applied. $P = 1$ refers to the ***k_t* algorithm** [110, 111] in which soft clusters are merged into harder ones first, and then the hardest clusters are grouped. Jets produced with the k_t algorithm may have irregular borders, as shown in Figure 5.4a. For $P = 0$, the **Cambridge-Aachen algorithm** [112], the merging of clusters does not depend on the p_T and is purely geometrically-ordered. The **anti-*k_t* jet reconstruction algorithm** ($P = -1$) [113] is the default choice in ATLAS. Because of the reverse p_T dependence, the soft objects tend to cluster with hard ones, which results in jets that are more circularly-shaped, and which center around the hard objects. Figure 5.4 represents the application of different jet reconstruction algorithms in a sample that is generated at parton-level. The FastJet package [114] is used to reconstruct jets in ATLAS.

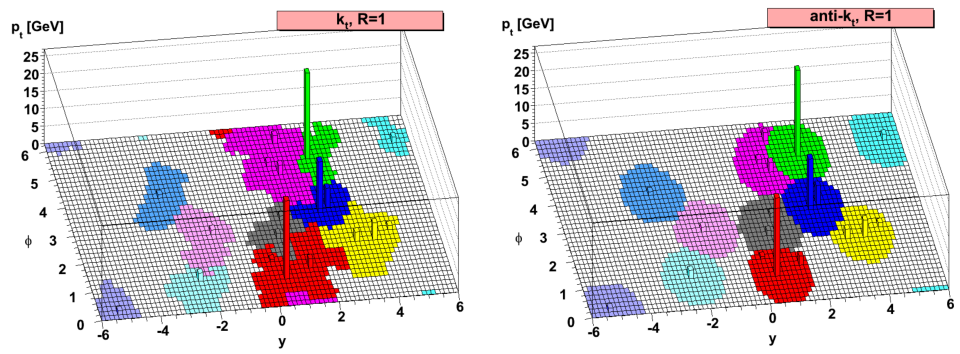

(a) (b)

Figure 5.4: Jet reconstruction with k_t (a) and anti-k_t (b) algorithms. Figure from [113].

5.2.2 Jet energy calibration

Jets are reconstructed from topo-clusters, which are calibrated at the EM scale. A dedicated jet energy scale (JES) calibration method must be implemented in order to derive more precise measurement of the kinematics of jets in the calorimeter. Figure 5.5 presents different stages of the JES calibration to correct

four-momentum and η using both simulation-based and data (in-situ) analyses. A summary of each step is outlined as follows:

Origin correction

Topo-clusters are reconstructed with the origin pointing to the center of the ATLAS detector. As a result, the four-momentum of jets must be recalculated to point to the hard-scatter primary vertex. This correction improves the η resolution of the jets [115].

Pileup correction

To remove excess energy due to in-time and out-of-time pileup, the pileup correction is applied in two steps [116]: first, the per-event pileup of energy depositions is parametrized based on the median p_{T} density of jets:

$$\rho = \left(\frac{p_{\mathrm{T}}}{A}\right) \quad , \tag{5.4}$$

where ρ is the p_{T} density of each jet, and A is the area of a jet. The second residual correction depends on N_{PV} (i.e., the number of PV), the number of interactions per bunch crossing μ, and the jet's pseudorapidity η. The p_{T} corrected after applying both of these pileup corrections is given by:

$$p_{\mathrm{T}}^{corr} = p_{\mathrm{T}}^{reco} - \rho \times A - \alpha \times (N_{\mathrm{PV}} - 1) - \beta \times \mu \quad , \tag{5.5}$$

where p_{T}^{reco} corresponds to the p_{T} of the reconstructed jet before pileup correction. Initial α and β values are derived from linear fits in bins of p_{T} and η.

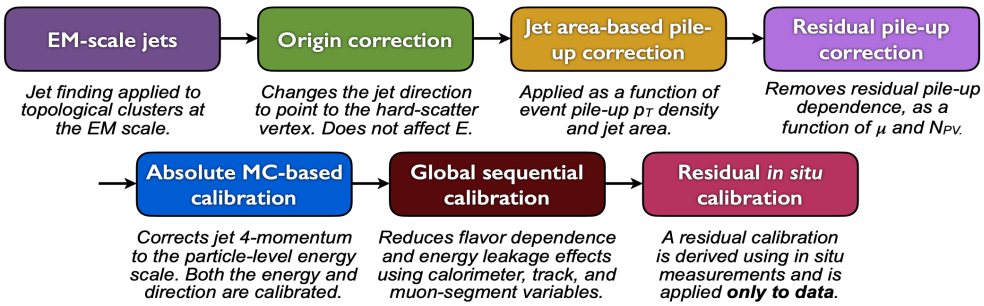

Figure 5.5: Each of these calibration steps must be applied for EM-scale jets. Figure from [115].

Jet energy scale and η calibration

After origin and pileup corrections, the JES calibration is applied to correct the reconstructed jet energy to a scale given by the MC truth jet energy. The average jet energy response R_{EM}^{jet} derived from the energy ratio of reconstructed jets to the truth jets (E^{reco}/E^{truth}), binned in E^{truth} and η_{det}, is used to correct the jet's four-momentum. Jet response is then used to correct the biases in the reconstructed jet η [117] and to calibrate the energy scale.

Global sequential calibration

Global sequential calibration (GSC) corrects for the jet energy scale dependency on the longitudinal jet energy distribution, on the transverse jet energy distribution, and on the particle composition of the jet. GSC corrections are made based on five individual jet properties:

1. Jet energy fraction measured in the first layer of the tile calorimeter.
2. Jet energy fraction measured in the third layer of the LAr calorimeter.
3. Number of identified tracks associated with the jet.
4. Number of muon track segments associated with the jet.
5. p_T-weight of the tracks associated with the jets.

In-situ calibration

The last step, in-situ data-driven calibration, corrects for the remaining differences in jet response between data and MC simulation. The η intercalibration uses well-measured reference jets in the central region ($|\eta|< 0.8$) to calibrate probe jets in forward regions ($0.8 < |\eta|< 4.5$). Z+jets, γ+jets and multijet events are used to correct for the last remaining differences between reconstructed jets in data and MC simulation. In this approach, the p_T balance between well-calibrated reference objects and probe jets is measured to derive the residual in-situ correction:

$$R = \left(\frac{p_T^{jet}}{p_T^{ref}}\right)_{data} / \left(\frac{p_T^{jet}}{p_T^{ref}}\right)_{MC} . \tag{5.6}$$

The largest number of individual uncertainties on the JES comes from in-situ calibration, which mainly reflects uncertainties due to the potential mismodel-

ing of physics effects, or uncertainties on the kinematic measurement of reference objects.

JES uncertainties

The various stages of the calibration described above result in a set of 80 systematic uncertainties. The majority (67) of them are associated with the in-situ calibration, and the other (13) systematics are derived from other sources, such as pileup uncertainties resulting in potential MC mismodeling of N_{PV} or μ, from the η intercalibration, and from the difference in jet response due to the flavor of the jet (light-quark, b-quark). The combined uncertainties are shown as a fraction of the total jet energy scale in Figure 5.6 for 3.2 fb^{-1} of Run 2 data as a function of p_{T} at $\eta = 0$ (5.6a) and as a function of η at $p_{\mathrm{T}} = 80$ GeV (5.6b).

5.2.3 Re-clustered jets

Due to the large center-of-mass energy in the LHC, there is sufficient energy available for the production of Lorentz-boosted heavy particles, whose decay products become collimated. The angular separation (ΔR) between decay products of a heavy object is approximately [118]:

$$\Delta R \approx \frac{2m}{p_{\mathrm{T}}} \quad , \tag{5.7}$$

where $\Delta R = \sqrt{(\Delta y)^2 + (\Delta\phi)^2}$, and m and p_{T} are the mass and transverse momentum of the parent particle. Thus, the opening angle between decay particles is smaller for parent particles with $p_{\mathrm{T}} \gg m$. As shown in Figure 5.7, the angular separation between the W boson and $b-$quark products of top quark decays ($t \to Wb$) is less than 0.4 for $p_{\mathrm{T}}^{\mathrm{t}} > 600$ GeV. The jet re-clustering technique is an effective way to reconstruct collimated decay particles with a large R jet ($R = 0.8$), instead of misleadingly obtaining multiple small $R = 0.4$ jets. In this method, the fully calibrated small radius jets are used as the input for the re-clustering algorithm, and jet trimming [119] is applied to suppress the effect of the pileup soft component on the resulting re-clustered jets. In the trimming procedure, any sub-jets with $p_{\mathrm{T}}^{i}/p_{\mathrm{T}}^{\mathrm{jet}} < f_{\mathrm{cut}}$ are discarded, where p_{T}^{i} is the sub-jet transverse momentum and f_{cut} is set to 0.1.

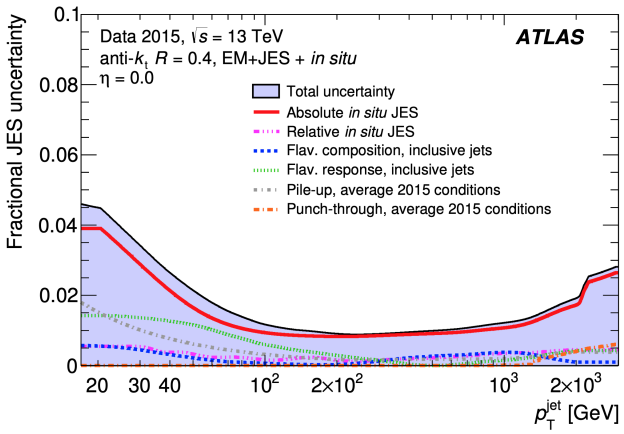

(a)

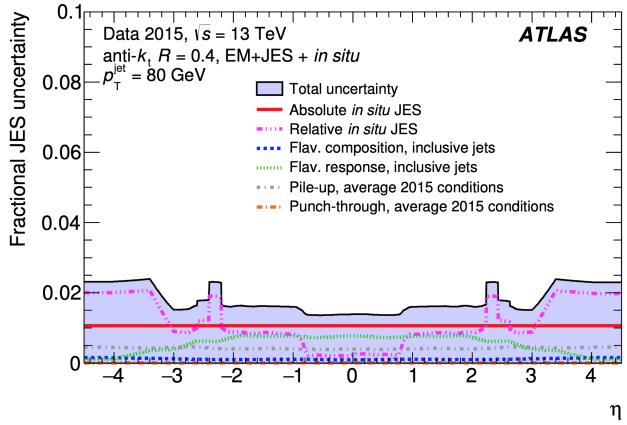

(b)

Figure 5.6: Combined uncertainties in JES as a function of (a) jet p_{T} at $\eta = 0$, and (b) η at $p_{\mathrm{T}} = 80$ GeV. Figure from [115].

5.3 Flavour tagging

The identification of heavy-flavour (b quark or c quark) and light-flavour jets plays a vital role in many ATLAS analyses. It is important in SM measurements such as the Higgs decay channel $H \to b\bar{b}$ (which has the highest branching fraction of all Higgs decays), or for determining the existence of b-jets in many BSM scenarios such as SUSY or Exotics models. A b-quark (or $\bar{b}$) produced in a pp collision will hadronize and form a bound state, which is called a B-hadron, with a quark that is typically of another flavour [11]. B-hadrons travel a short distance (of the order of mm) and decay into other hadrons and leptons. The typical decay topology of B-hadrons is shown in Figure 5.8.

Since Run1, there have been three different b-tagging algorithms [121] used in ATLAS. Impact parameter-based algorithms (IP2D and IP3D) make use

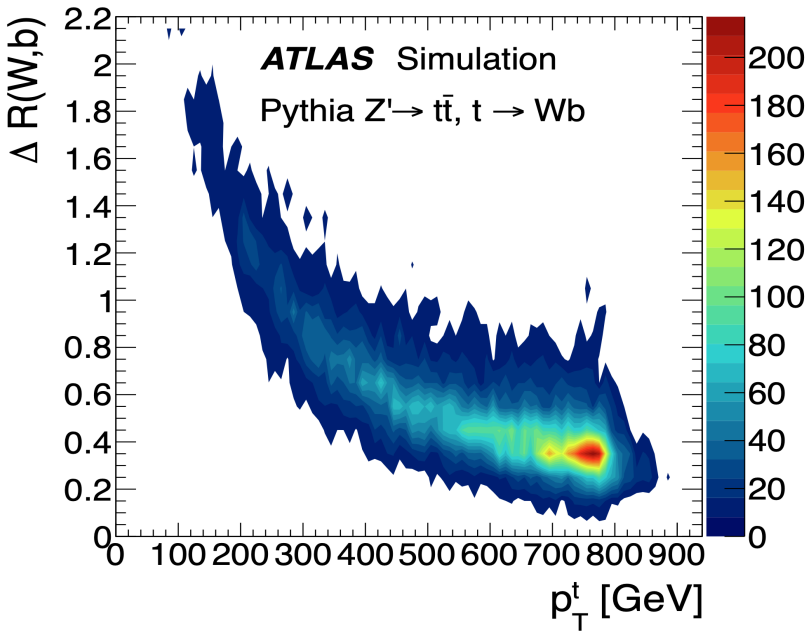

Figure 5.7: Angular separation between the W boson and $b-$quark in top decays as, a function of top-quark transverse momentum. Figure from [120].

of the transverse d_0 and longitudinal z_0 impact parameter significance of the jet tracks. Tracks are associated to jets based on spatial matching $\Delta R_{\text{jet,track}}$ defined as:

$$\Delta R_{\text{jet,track}} = \sqrt{(\eta_{\text{jet}} - \eta_{\text{track}})^2 + (\phi_{\text{jet}} - \phi_{\text{track}})^2} \quad . \tag{5.8}$$

Typically, tracks originating from B hadrons (secondary vertices) possess a larger impact parameter than light-quark and gluon jets (originating from the PV). Secondary vertex finding algorithms (SV1) reconstruct the secondary vertex for each jet using the candidate tracks. Tracks from long-lived particles (e.g. K_S or Λ), and photon conversion or hadronic interactions with the detector material are rejected. A decay chain algorithm, JetFitter [122], attempts to exploit the weak decay of b-hadrons to c-hadrons (PV$\rightarrow b \rightarrow c$), and reconstruct the two decay vertices as shown in Figure 5.8. In this approach, the Kalman filter [106] is used to find the flight path and the positions of b-hadrons.

The default ATLAS b-tagging algorithm is MV2c10, which uses input variables obtained from IP, SV and JetFitter results [123, 124]. MV2c10 is an algorithm based on a boosted decision tree (BDT), which is trained with a $t\bar{t}$ sample to discriminate between b-jets as signal, and light-jets and c-jets as backgrounds. The c-jet and light-jet fractions in the training sample for MV2c10 were set to the typical relative data fractions of 7% and 93%. Figure 5.9 shows

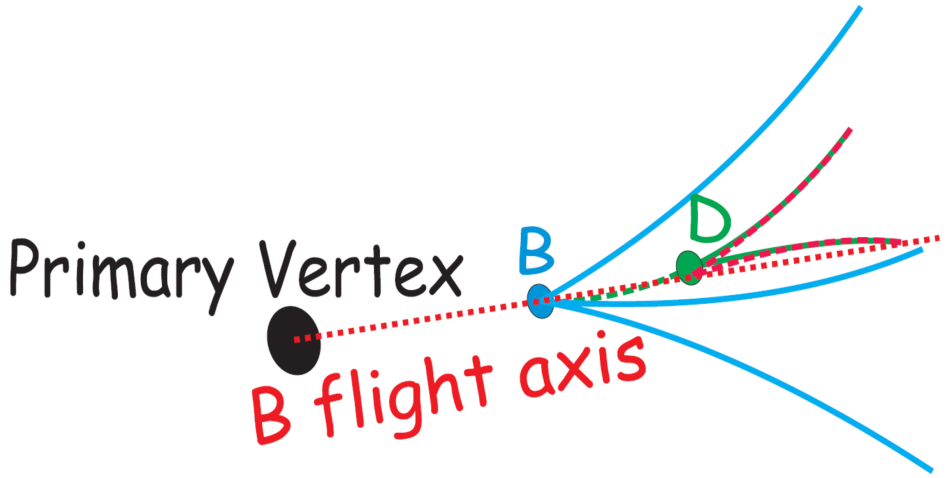

Figure 5.8: Schematic view of the flight and decay of a B hadron, and the subsequent flight and decay of its D hadron decay product. A D hadron is a meson containing a single c quark as the heavier of its quarks. Figure from [122].

the performance of different b-taggers used by ATLAS during Run2. The light-flavour and c-jet rejection are shown as functions of the b-tagging efficiency. MV2c20 and MV2c00 belong to the MV2 family, where the name of the tagger indicates the c-jet fraction that is used in the training. Improved impact parameter resolution due to the IBL insertion is expected to increase the rejection of c- and light-flavour jets in Run2. MV2c10 with the 2016 configuration provides approximately the same light-flavour jet rejection as the MV2c20 configuration, but 40% higher c-jet rejection at the 77% b-tagging efficiency working point.

5.4 Muons

Muons leave charged tracks in both the ID and the MS, thus in the ATLAS experiment, information from the ID and the MS is combined to reconstruct muons. There are four different classifications for ID-MS muon candidate reconstruction [125] **Combined** muons: ID and MS tracks that have been combined with a global fit; **Segment-tagged** muons: low p_{T} muons which cross only one layer of a MS chamber, and can be associated with an ID track that points toward this chamber; **Calorimeter-tagged** muons: an ID track is matched to an energy deposit in the calorimeter compatible with a minimum-ionizing particle and that is also consistent with being a muon. This type recovers acceptance for muons in the region that MS is not fully efficient (since cabling

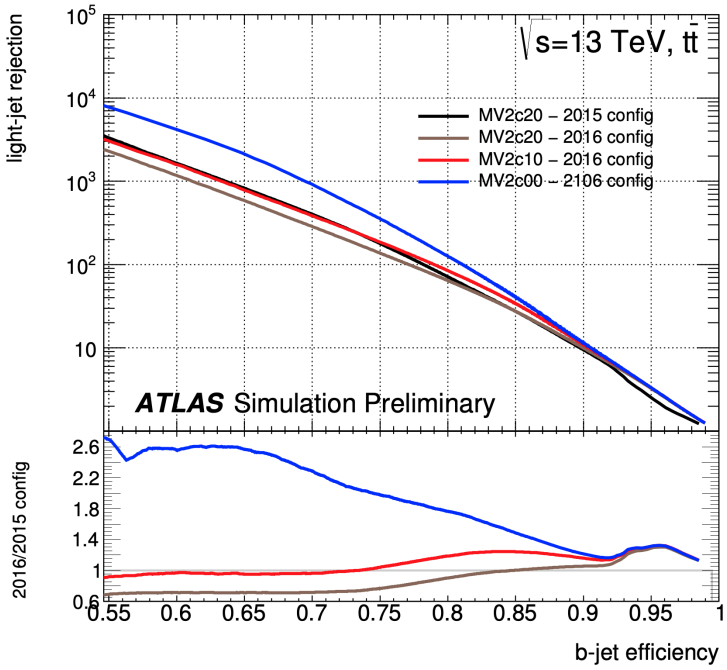

(a)

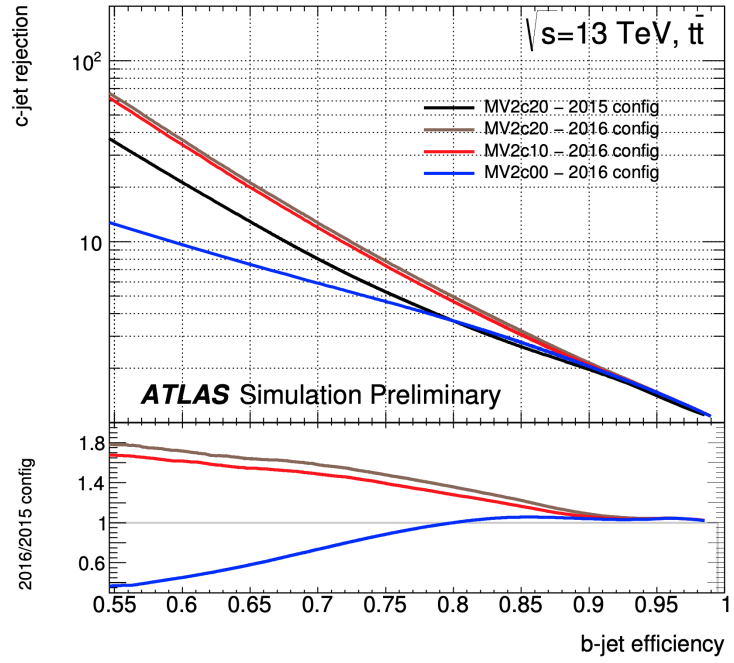

(b)

Figure 5.9: The light-flavour (a) and c-jet (b) rejection of the MV2 b-tagging algorithm as a function of b-jet tagging efficiency. Figure from [124].

and services to the calorimeter affect this region). **Extrapolated** muons: MS tracks which are compatible with having originated from the IP are used to

reconstruct muon candidates. This category extends the acceptance to high η regions which are not covered by the ID.

In order to reject background contamination from decays of pions and kaons, muon identification is used. The three most important variables used in muon identification are: the difference in q/p significance, which is defined as the ratio of the charge and the momentum of the muon measured in the ID and MS; the difference in ρ which is defined as the normalized p_{T} measurement; and the normalized measurement in the ID and MS divided by combined track p_{T}; and the normalized χ^2 fit of the combined track. There are four muon identification selections (known as operating points, or OPs) with an increasing signal purity: Loose, Medium, Tight, and High-p_{T}. Medium OP is the default selection in ATLAS, as this selection tends to minimise the systematic uncertainties associated with muon reconstruction and calibration. Only Combined and Extrapolated muons are used in the medium OP, and the former are required to have ≥ 3 hits in at least two MDT layers, while the latter must have at least three three MDT/CSC layers within the region $2.5 < |\eta| < 2.7$. Figure 5.10 shows the reconstruction efficiency as a function of transverse momentum for the Medium OP. $Z \to \mu\mu$ and $J/\psi \to \mu\mu$ samples are used to derive the reconstruction efficiency for high- and low-p_{T} muons.

Muon isolation is a powerful tool to suppress background muons that originate from semileptonic decay of hadrons. The *LooseTrackOnly* isolation OP that is used in this dissertation has an efficiency that is consistently near 99% in η and p_{T} for $p_{\mathrm{T}}^{\mathrm{varcone30}}/p_{\mathrm{T}}^{\mu}$. $p_{\mathrm{T}}^{\mathrm{varcone30}}$ is a track-based isolation variable, defined as the scalar sum of the transverse momenta of the tracks with $p_{\mathrm{T}} > 1$ GeV in a cone with $\Delta R = \min(10\ \mathrm{GeV}/p_{\mathrm{T}}^{\mu}, 0.3)$ around the muon.

5.5 Electrons

In the ATLAS detector, electrons leave tracks in the ID and energy deposits in the ECal. In the central region ($|\eta| < 2.47$), electron particle identification is performed in two steps [126, 127] first a 3 unit $\times$ 5 unit sliding window region, in units of 0.025×0.025 ($\eta \times \phi$), is used to search for seed clusters with energies above 2.5 GeV. Then, tracks in the ID are extrapolated and matched to the clusters, which are subsequently used to distinguish between electrons and photons. The key feature is that photons carry no electric charge and produce no tracks when they pass through the ID.

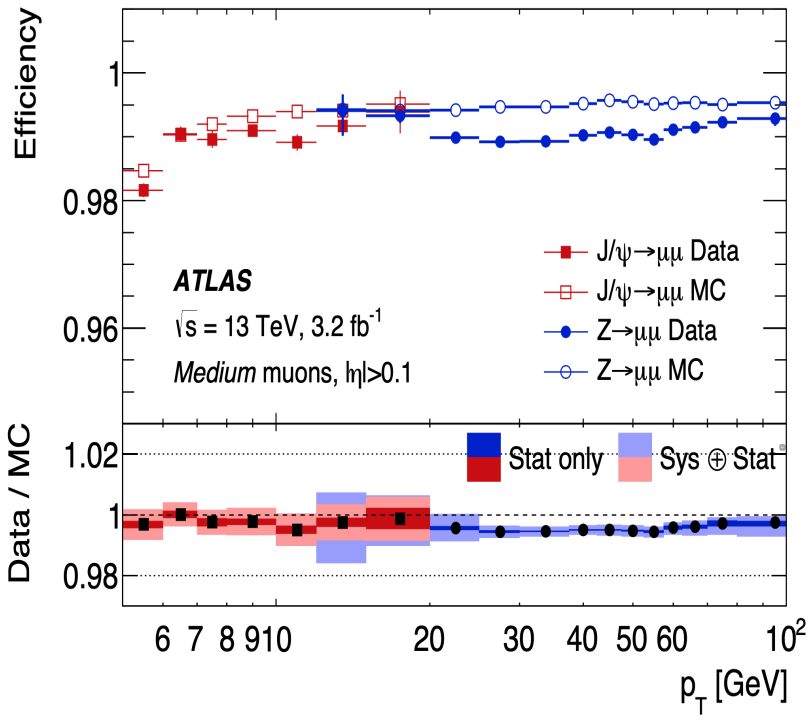

Figure 5.10: Reconstruction efficiency for the Medium muon selection as a function of the muon p_{T}, in the region $0.1 < |\eta| < 2.5$. $Z \to \mu\mu$ and $J/\psi \to \mu\mu$ samples are used for high- and low-p_{T} regions. Figure from [125].

Electron identification is applied to reject backgrounds such as converted photons or electrons in the decay of hadronic jets. The variables used to distinguish signal from backgrounds are related to quantities such as the ratio of E_{T} in different HCal and ECal layers, number of hits in pixel and SCT detectors, and track-cluster matching. Loose, Medium and Tight are three identification OPs in ATLAS, ordered by increasing background rejection level (signal purity). In addition to the identification process above, electrons need to pass isolation criteria to be classified as prompt. In the isolation process, most backgrounds from non-isolated electrons, such as electrons produced from photon conversion or from heavy flavour hadron decays, are suppressed. The electron isolation used in this dissertation is based on a track isolation variable, $p_{\mathrm{T}}^{\mathrm{varcone0.2}}$, defined as the scalar sum of the transverse momentum of all tracks excluding electron-associated tracks, passing quality selections, in a cone $\Delta R = \min(0.2, 10\ \mathrm{GeV}/E_{\mathrm{T}})$ around the electron candidate. The default ATLAS isolation OP is LooseTrackOnly with 99% efficiency, which does not have any significant variation over the full range of E_{T} considered in this dissertation.

5.6 Missing Transverse Momentum

The missing transverse energy ($\vec{E}_{\mathrm{T}}^{\mathrm{miss}}$) is the final reconstructed object that we consider, and which refers to any p_{T} imbalance in an event. This can, for example, originate from weakly interacting particles such as neutrinos in the SM, or LSPs in SUSY. $E_{\mathrm{T}}^{\mathrm{miss}}$ is defined [128, 129] as the negative vector sum of the p_{T} of reconstructed calibrated objects (hard term), as well as the soft term, which accounts for ID tracks or calorimeter energy deposits not associated with any reconstructed objects (soft term):

$$\vec{E}_{\mathrm{T}}^{\mathrm{miss}} = -\sum_{\substack{\text{electrons}\\ \text{taus}\\ \text{muons}}} \vec{p}_{\mathrm{T}} - \sum_{\text{photons}} \vec{p}_{\mathrm{T}} - \sum_{\text{jets}} \vec{p}_{\mathrm{T}} - \sum_{\text{soft}} \vec{p}_{\mathrm{T}} \quad .$$

A set of selections is applied to all reconstructed objects in the above formula to achieve optimal $E_{\mathrm{T}}^{\mathrm{miss}}$ reconstruction performance.

The soft term in the $E_{\mathrm{T}}^{\mathrm{miss}}$ definition is determined using several approaches in ATLAS, of which just two formulations are summarized here. In the **Track soft term** (TST), high-quality tracks from the hard-scatter PV that are not associated to any charged object such as an electron, a tau lepton, a muon, or a jet contribute to $E_{\mathrm{T}}^{\mathrm{miss}}$ reconstruction. TST is largely insensitive to pileup effects, since just tracks from the hard-scatter PV are included in the $E_{\mathrm{T}}^{\mathrm{miss}}$ calculation [130]. In the **Cluster soft term** (CST), the $E_{\mathrm{T}}^{\mathrm{miss}}$ is calculated from topo-clusters calibrated at EM scale which are not associated with any reconstructed objects. CST contains information from neutral particles (unlike TST), however it is sensitive to the effects of pileup. TST is the algorithm used in this dissertation to calculate the $E_{\mathrm{T}}^{\mathrm{miss}}$ soft term.

Chapter 6

Search for SUSY in Gluino Pair Production

As the center-of-mass energy was increased to 13 TeV for LHC Run2 (as compared with the 7 and 8 TeV center-of-mass energies used in LHC Run1), the physics reach of many SUSY searches was greatly increased: for example, searches for inclusive production of squarks and gluinos, and for the electroweak production of sparticles. This analysis is a search for production of gluino pairs, which is well-motivated due to the increase in cross-section of gluino pairs with increasing center-of-mass energies (as shown in Figure 6.1). A significant excess of observed events over expected backgrounds was not observed in the previous iteration of this analysis [131, 132]. This chapter is summarized as follows: Section 6.1 describes the signal models used to interpret the analysis results. Sections 6.2 to 6.5 present the data sets and MC samples used to simulate SM backgrounds, and the definitions of the variables used to discriminate between SUSY signals and SM backgrounds. Each of the analysis regions in the cut-and-count approach are detailed in Section 6.6, and Section 6.7 discusses the main sources of experimental and theoretical uncertainties included in the fit results.

6.1 Signal Models

The large number of free parameters in the MSSM makes it effectively impossible to scan over the entire phase space. To reduce the number of parameters, **simplified models** are defined as the limits of more complete models, and tend to include just a few masses of SUSY particles and production cross-

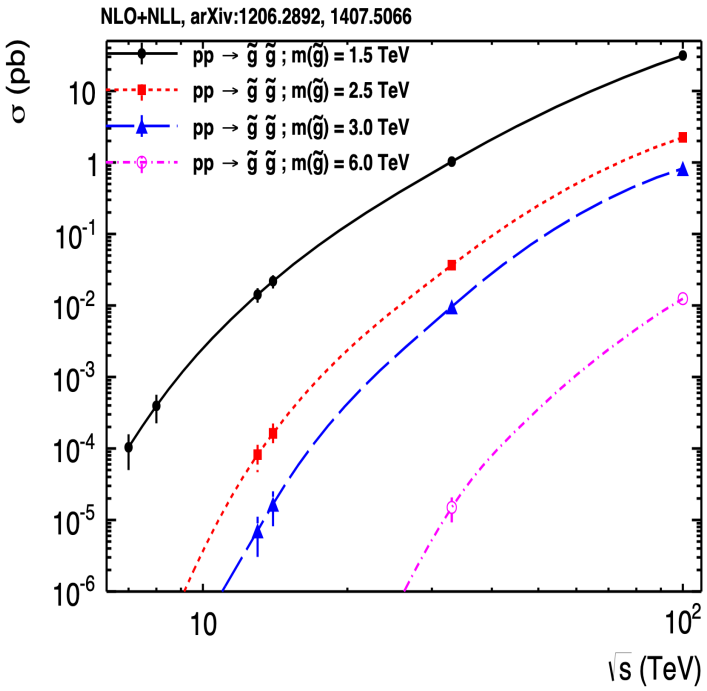

Figure 6.1: Gluino pair production cross-section as a function of center-of-mass energy. Figure from [133].

sections as free parameters. Figure 6.2 illustrates the simplified models used in this dissertation as signal processes to optimize event selection and interpret the results. In the Gtt model, containing the decay topology shown in Figure 6.2a, pairs of gluinos are produced ($pp \to \tilde{g}\tilde{g}$), and then each gluino decays with 100% branching ratio to an off-shell stop and an anti-top ($\tilde{g} \to \tilde{t_1}\bar{t}$), and then the stop decays to a top quark and to the lightest neutralino ($\tilde{t_1} \to t\tilde{\chi}_1^0$). In the Gbb model, the gluino three-body decay happens through an off-shell sbottom ($\tilde{g} \to \tilde{b_1}\bar{b} \to b\bar{b}\tilde{\chi}_1^0$). In order to have only two free parameters in the Gtt and Gbb models (specifically, the gluino and the neutralino masses), the stop and sbottom are assumed to be off-shell. The presence of the top quark in the Gtt model motivates the design of signal regions with higher multiplicity than for Gbb models. The final state in both models contains multiple jets, of which some are b-tagged, and large $E_{\mathrm{T}}^{\mathrm{miss}}$ from the undetectable neutralinos.

6.2 Data and Monte Carlo backgrounds

The ATLAS data used in this dissertation are collected from pp collisions produced by the LHC at a center-of-mass-energy $\sqrt{s} = 13$ TeV and 25 ns bunch

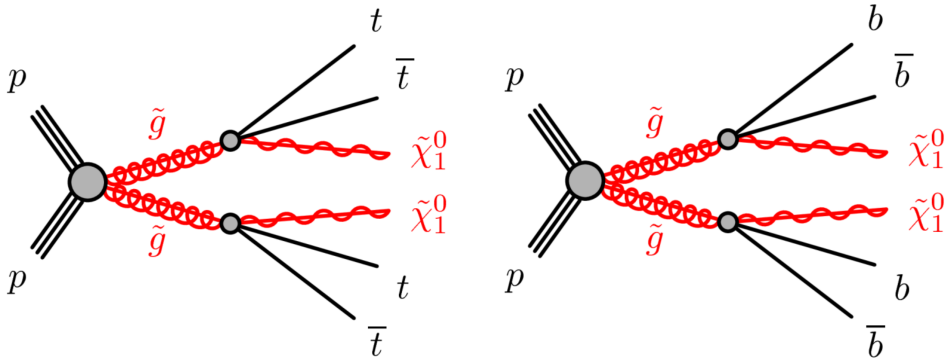

(a) (b)

Figure 6.2: Feynman diagrams for decay topologies in (a) Gtt and (b) Gbb simplified models.

spacing during 2015-2018. After applying data-quality selections (Section 4.3), the total dataset contains 139 fb^{-1} of integrated luminosity. The uncertainty in the combined 2015–2018 integrated luminosity is 1.7%, obtained using the $x-y$ beam separation scan method with the LUCID detector [134]. Events are required to pass the $E_{\mathrm{T}}^{\mathrm{miss}}$ trigger with the lowest available unprescaled threshold. (These thresholds differ between the different years of data taking).

In this analysis, all signal and background processes are MC simulated, except the multijet background, which is estimated based on data-driven method (which will be described in subsection 6.5.1). The Gtt and Gbb models are generated with up to two additional partons using MADGRAPH5_aMC@NLO v2.3.3 at leading order (LO) with the NNPDF2.3 [135] Parton Density Function (PDF) sets. Pythia v8.2 is subsequently used for the modeling of the parton showering, hadronisation and UE.

The main source of SM background is $t\bar{t}$ production with additional jets. This background channel is simulated at next-to-leading order (NLO) using POWHEG-BOX with the NNPDF3.0 PDF set, interfaced to Pythia v8.2 for parton showering and hadronisation. In order to have enough MC statistics in the extreme signal-sensitive regions (signal regions with tight $E_{\mathrm{T}}^{\mathrm{miss}}$ selection), $E_{\mathrm{T}}^{\mathrm{miss}}$-sliced $t\bar{t}$ samples are used, in addition to the inclusive sample.

Smaller backgrounds come from production of single-top quarks, top quark pairs produced in association with $W/Z/h$ and additional jets ($t\bar{t}+V$), four top quark ($t\bar{t}t\bar{t}$) events, electroweak vector bosons associated with extra jets (W/Z+jets), and diboson ($WW/ZZ/WZ$) events. Single-top and $t\bar{t}+h$ events are simulated using POWHEG-BOX v2 interfaced to Pythia v8.2. The $t\bar{t}+V$ and four top quark use MADGRAPH5_aMC@NLO and Pythia v8.2 respect-

ively. The production of W/Z+jets and diboson events are simulated in Sherpa with the NNPDF3.0 PDF set. A summary of the sample generation and PDF packages used to simulate signals and backgrounds is shown in Table 6.1.

All simulated background samples are passed through the full ATLAS detector simulation using GEANT4 as discussed in subsection 4.4.2. The Gtt and Gbb samples are reconstructed with the fast simulation method ATLFAST-II [136], which uses a fast calorimeter simulation to parameterise the lateral and longitudinal shapes of particle showers.

Process	Generator	PDF set	Parton Shower
SUSY signal	MADGRAPH5_aMC@NLO	NNPDF2.3	PYTHIA 8
$\boldsymbol{t\bar{t}}$	POWHEG-BOX	NNPDF3.0	PYTHIA 8
Single-top / $\boldsymbol{t\bar{t}+h}$	POWHEG-BOX	NNPDF3.0	PYTHIA 8
$\boldsymbol{t\bar{t}+V}$ / **4-tops**	MADGRAPH5_aMC@NLO	NNPDF3.0	PYTHIA 8
$\boldsymbol{W/Z}$**+ jets**	SHERPA 2.2	NNPDF3.0	SHERPA 2.2
Diboson	SHERPA 2.2	NNPDF3.0	SHERPA 2.2

Table 6.1: List of the MC generators used for each of the simulated processes.

6.3 Object Definition

Physics objects used in this analysis are classified as either baseline or signal objects. Looser selections are applied to define baseline objects such as electrons, muons and jets. Baseline objects are used as the input for the overlap removal procedure to prevent double-counting. Further requirements are then applied to select final signal objects. The specific selections applied to objects, and to the overlap removal procedure, are given below:

Primary vertex: Interaction vertices are reconstructed from at least two tracks with $p_{\mathrm{T}} > 0.4$ GeV. The vertex with the largest sum of squares of the p_{T} from associated tracks is identified as the primary vertex (discussed in Section 5.1).

Jets: Baseline jets are reconstructed from topological energy clusters using the anti-k_{t} algorithm with radius parameter $R = 0.4$ (subsection 5.2.1). These jets are calibrated at the particle level using the EM+JES+GSC scheme (subsection 5.2.2) and are required to have $p_{\mathrm{T}} > 20$ GeV and $|\eta| <$ 2.8. To suppress fake jets from pileup, jets with $p_{\mathrm{T}} < 50$ GeV must pass the jet-vertex tagger (JVT) *Medium* selection [137,138]. JVT uses information from the scalar sum of the p_{T} of the tracks associated to the jet, and hard-scattering jets are assigned a higher JVT value compared to pileup jets. After overlap removal, the remaining jets are identified as signal if they pass a $p_{\mathrm{T}} > 30$ GeV cut. Baseline jets passing the overlap removal procedure are used for further re-clustering with the anti-k_{t} algorithm and a large radius parameter ($R = 0.8$), as described in subsection 5.2.3. The resulting re-clustered jets are then required to have $p_{\mathrm{T}} > 100$ GeV and $|\eta| <$ 2.

A jet is tagged as a b-jet by means of the MV2c10 algorithm (described in Section 5.3). The OP used in this analysis corresponds to an efficiency of 77.60%, derived from simulated $t\bar{t}$ events. This OP corresponds to rejection factors of 6, 22, and 134 against jets originating from c-quarks, τ-leptons, and light jets respectively.

Electrons: Candidate electrons are reconstructed from clusters of energy in the ECal and ID, and are required to satisfy the *Loose* identification OP and also to pass kinematic selections such as $p_{\mathrm{T}} > 20$ GeV and $|\eta| <$ 2.47 (described in Section 5.5). Signal electrons need to pass the *Medium*

identification OP and *LooseTrackOnly* isolation OP, and are matched to the primary vertex by requiring $|d_0/\sigma_{d_0}|< 5$.

Muons: Baseline muons must satisfy the *Medium* identification OP (described in Section 5.4), and have $p_{\mathrm{T}} > 20$ and $|\eta|< 2.47$. After applying overlap removal, signal muons are required to pass additional selections such as the *FCTightTrackOnly* [139] isolation OP, and to have an impact parameter significance $|d_0/\sigma_{d_0}|< 3$.

Missing transverse energy: The negative vector sum ($\vec{p}_T^{\,\mathrm{miss}}$) of the transverse momenta of all calibrated objects in an event, plus the soft term, is used to define $E_{\mathrm{T}}^{\mathrm{miss}}$ (Section 5.6). In this analysis, the soft term is calculated from ID tracks matched to the PV to make it more resilient to pileup contamination (i.e., the TST algorithm, as explained in Section 5.6).

Objects that potentially have been double counted between jets, muons, and electrons are removed by applying a sequential overlap removal procedure. First, the electron candidates that originate from muon radiation processes, which have $\Delta R < 0.01$[1] from muon candidates, are removed. In the next step, the overlaps between jet and electron candidates are resolved: 1) Any non-b-tagged jets which lie within $\Delta R < 0.2$ from an electron are most likely formed from the showering of a prompt electron, and thus they are discarded[2]. 2) Electron candidates that are produced in the decay chain of hadrons are removed if they satisfy $E_{\mathrm{T}} < 50$ GeV and $\Delta R < 0.4$ from the axis of any jets. 3) To increase the removal efficiency in boosted topologies (mainly of boosted top quarks[3] in this analysis), higher-energy electrons with $E_{\mathrm{T}} > 50$ GeV are removed if the distance parameter ΔR is lower than $\min(0.4, 0.04{+}10\ \mathrm{GeV}/E_{\mathrm{T}})$.

Finally, overlaps between muon and jet candidates are resolved. First, the jets that originate from high-p_{T} muon radiation must be removed. Consequently, jets are removed if they are in close proximity to muons ($\Delta R < 0.2$) and have less than three matching ID tracks. Low-p_{T} muons that originate from the decay chain of hadrons are removed if $\Delta R < 0.4$. Muons with p_{T} higher than 50 GeV and $\Delta R < \min(0.4, 0.04 + 10\ \mathrm{GeV}/E_{\mathrm{T}})$ are also removed.

[1] The distance parameter ΔR is defined in the $y - \phi$ plane as discussed in subsection 5.2.3.
[2] Semileptonic decays of B hadrons include a lepton, and thus the b-tagged jets are retained.
[3] In leptonic decays of boosted top quarks, the lepton and the b jet are produced in close proximity to the top axis, so an energy-dependent cut needs to be applied in association with ΔR.

6.4 Definition of Analysis Variables

Various kinematic variables can be used to discriminate between signal events as described in Gtt and Gbb SUSY models, and the background events from SM processes. There are two classes of variables used in this analysis: the first type is sensitive to the multiplicity of the event, e.g. the number of signal jets or signal leptons (electrons or muons). The second type is composed of energy-related variables, e.g. the inclusive effective mass ($m_{\text{eff}}^{\text{incl}}$) or transverse mass ($m_{\text{T}}$). The definitions of the variables used to describe events are provided here:

N_{jet}: The number of signal jets with $p_{\text{T}} > 30$ GeV and $|\eta| < 2.8$ in the event.

$N_{b-\text{jet}}$: The number of b-tagged jets at the 77% efficiency OP (see Section 5.3) and with $p_{\text{T}} > 30$ GeV.

N_{lepton}: The number of signal electrons and muons (leptons).

$m_{\text{eff}}^{\text{incl}}$: The inclusive effective mass is defined as the scalar sum of the p_{T} of all signal leptons and jets, plus the missing transverse energy:

$$m_{\text{eff}}^{\text{incl}} = \sum_{i \leq n} {p_{\text{T}}}^{j_i} + \sum_{j \leq m} {p_{\text{T}}}^{l_j} + E_{\text{T}}^{\text{miss}} \quad . \tag{6.1}$$

The effective mass is larger in signal events because of the large object multiplicity and also because of the $E_{\text{T}}^{\text{miss}}$ coming from the LSP or neutrinos.

m_{T}: In events with at least one selected signal lepton, the transverse mass m_{T} between the leading lepton (i.e., the lepton with the highest p_{T}) and $E_{\text{T}}^{\text{miss}}$ is defined as:

$$m_{\text{T}} = \sqrt{2 p_{\text{T}}^{l} E_{\text{T}}^{\text{miss}} (1 - \cos \Delta\phi(\vec{E}_{\text{T}}^{\text{miss}}, \vec{p}_{\text{T}}^{l}))} \quad . \tag{6.2}$$

The m_{T} distribution is bounded from above by the W boson mass, and thus it provides a way to discriminate between the Gtt signal which tends to have large $E_{\text{T}}^{\text{miss}}$ and backgrounds from W+jets and semi-leptonic $t\bar{t}$.

$m_{\text{T, min}}^{b-\text{jets}}$: The minimum transverse mass $m_{\text{T, min}}^{b-\text{jets}}$ between the $E_{\text{T}}^{\text{miss}}$ and

any of the three highest-p_{T} $b-$tagged jet in the event is derived by:

$$m_{\mathrm{T,\,min}}^{b-\mathrm{jets}} = \min_{i\leq 3}\left(\sqrt{2p_{\mathrm{T}}^{b-\mathrm{jet}_i}E_{\mathrm{T}}^{\mathrm{miss}}(1-\cos\Delta\phi(\vec{E}_{\mathrm{T}}^{\mathrm{miss}},\vec{p}_{\mathrm{T}}^{\,b-\mathrm{jet}_i}))}\right) \quad . \tag{6.3}$$

For semi-leptonic $t\bar{t}$ events, the $m_{\mathrm{T,\,min}}^{b-\mathrm{jets}}$ distribution has an endpoint corresponding to the top quark mass, while peaking at higher values for Gbb and Gtt events.

$\Delta\phi_{\mathrm{min}}^{\mathbf{4j}}$**:** In the lepton veto region, $\Delta\phi_{\mathrm{min}}^{4\mathrm{j}}$ is defined as the minimum azimuthal angle between any of the leading four jets and the $E_{\mathrm{T}}^{\mathrm{miss}}$:

$$\Delta\phi_{\mathrm{min}}^{4\mathrm{j}} = \min_{i\leq 4}\left(|\phi_{\mathrm{jet}}^{i} - \phi_{E_{\mathrm{T}}^{\mathrm{miss}}}|\right) \quad . \tag{6.4}$$

This variable is used to suppress multijet background, which can produce large $E_{\mathrm{T}}^{\mathrm{miss}}$ events due to mismeasured jets or neutrinos emitted close to the jet's axis. In both cases the fake $E_{\mathrm{T}}^{\mathrm{miss}}$ has an azimuthal angle value close to the mismeasured jet, and $\Delta\phi_{\mathrm{min}}^{4\mathrm{j}} > 0.4$ can reject events with no real $E_{\mathrm{T}}^{\mathrm{miss}}$ (see subsection 6.5.1).

$M_J^{\sum}$**:** The total jet mass is defined as:

$$M_J^{\sum} = \sum_{i\leq 4} m_{J,i} \quad , \tag{6.5}$$

where $m_{J,i}$ refers to the mass of large-radius re-clustered jets in the event. As discussed in subsection 5.2.3, a single large-radius re-clustered jet can be used to reconstruct the decay products of a hadronically-decaying boosted top quark. In the case of boosted Gtt signal events where up to four high p_{T} top quarks are produced, $M_J^{\sum}$ has higher values compared to the SM backgrounds.

6.5 Event preselection

Event selection and preselection are two separate sets of selections, and both are applied to select each event in this analysis. In the event selection, general kinematic requirements are applied to remove poor quality luminosity blocks or corrupted events due to noise in the detector. Some of the common event selections recommended by ATLAS are summarized below:

Good Run List Selection: As described in Section 4.3, data quality selections are first applied to data to remove poor quality luminosity blocks. The runs with IBL off are not included, because this analysis is sensitive to b-tagging.

Tile, LAr, SCT corrupted events: Corrupted events due to errors or problematic regions of the Tile, LAr, and SCT need to be removed, following ATLAS recommendations.

Trigger: The lowest unprescaled (see Section 4.2) $E_{\mathrm{T}}^{\mathrm{miss}}$ triggers for different dataset years and periods are used in this analysis (this is done via the "IsMETTrigPassed" function in **SUSYTools** [140]). These triggers are fully efficient at $E_{\mathrm{T}}^{\mathrm{miss}} > 200$ GeV (i.e., the analysis offline $E_{\mathrm{T}}^{\mathrm{miss}}$ cut at preselection level) and are listed below:

- 2015: `HLT_xe70_mht`
- 2016:
  - A–D3: `HLT_xe90_mht_L1XE50`
  - D4–F1: `HLT_xe100_mht_L1XE50`
  - F2–: `HLT_xe110_mht_L1XE50`
- 2017:
  - B–D5: `HLT_xe110_pufit_L1XE55`
  - D6–: `HLT_xe110_pufit_L1XE50`
- 2018:
  - B–C4: `HLT_xe110_pufit_xe70_L1XE50`
  - C5–: `HLT_xe110_pufit_xe65_L1XE50`

To examine the pre-fit modelling of analysis variables, a preselection with loose criteria has been defined. Preselection criteria in the 0-lepton (0L) channel with a veto on the number of selected leptons, and in the 1-lepton channel (1L) with ≥ 1 signal lepton, are defined in Table 6.2.

Preselection requirements		
	0-lepton	1-lepton
Trigger	$E_{\mathrm{T}}^{\mathrm{miss}}$ trigger	
$E_{\mathrm{T}}^{\mathrm{miss}}$	$E_{\mathrm{T}}^{\mathrm{miss}} > 200$ GeV	
N_{lepton}	$= 0$	≥ 1
$\Delta\phi_{\mathrm{min}}^{\mathrm{4j}}$	> 0.4	-
N_{jet}	≥ 4	
$N^{\mathrm{b\text{-}jet}}$	≥ 3	

Table 6.2: Definition of the preselection criteria for 0-lepton and 1-lepton channels.

6.5.1 QCD estimation

The production cross-section of multijet events is extremely large at the LHC [141], so a data-driven approach is preferred to MC simulation. The multijet background has negligible yield in regions with $\geq$ 1-lepton because of the requirements on the selected leptons, on the multiplicity of jets, and on large $E_{\mathrm{T}}^{\mathrm{miss}}$. SUSY strong production analyses suppress a large majority of multijet events in lepton veto regions (0L) by using a $\Delta\phi_{\mathrm{min}}^{\mathrm{4j}} > 0.4$ selection cut. To estimate the remaining multijet events, a template method is used, following the strategy of Ref. [142]. This data-driven method is described by the following steps:

1. For each 0L region, an equivalent selection with reverse $\Delta\phi_{\mathrm{min}}^{\mathrm{4j}}$ is considered (modified from $\Delta\phi_{\mathrm{min}}^{\mathrm{4j}} > 0.4$ to $\Delta\phi_{\mathrm{min}}^{\mathrm{4j}} < 0.1$). This selection keeps similar kinematic properties as the original region, but is enriched in multijet events, and is thus used to derive the shape of the multijet distribution.

2. The multijet contribution is obtained by subtracting the expected background in this region ($\Delta\phi_{\mathrm{min}}^{\mathrm{4j}} < 0.1$) from the data.

3. A normalization factor is needed to extrapolate the multijet background to the original $\Delta\phi_{\mathrm{min}}^{\mathrm{4j}} > 0.4$ region. To derive this normalization factor, an exponential fit to the multijet distribution is performed in the range

$0.1 < \Delta\phi_{\text{min}}^{\text{4j}} < 0.4$, and the ratio of the integral of the exponential fit in $\Delta\phi_{\text{min}}^{\text{4j}} > 0.4$ to $\Delta\phi_{\text{min}}^{\text{4j}} < 0.1$ is set as the normalization factor.

The exponential fit for the different years of data-taking is shown in Figure 6.3. The multijet normalization factor for the full Run2 is derived as $\Delta\phi_{\text{norm}} = 0.059$. The multijet extrapolation to the preselection region ($\Delta\phi_{\text{min}}^{\text{4j}} > 0.4$) is first validated in lower $\Delta\phi_{\text{min}}^{\text{4j}}$ slices, such as $0.1 < \Delta\phi_{\text{min}}^{\text{4j}} < 0.2$ (using an appropriate normalization factor specifically derived for this slice). In Figure 6.4, one can see that the multijet estimate, in addition to the other backgrounds, leads to a good modelling of the data in the $0.1 < \Delta\phi_{\text{min}}^{\text{4j}} < 0.2$ region.

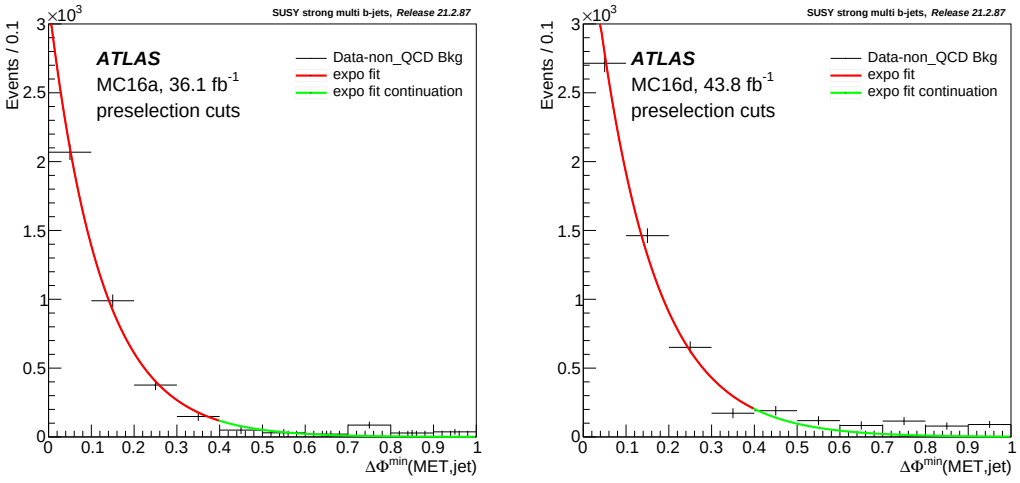

(a)

(b)

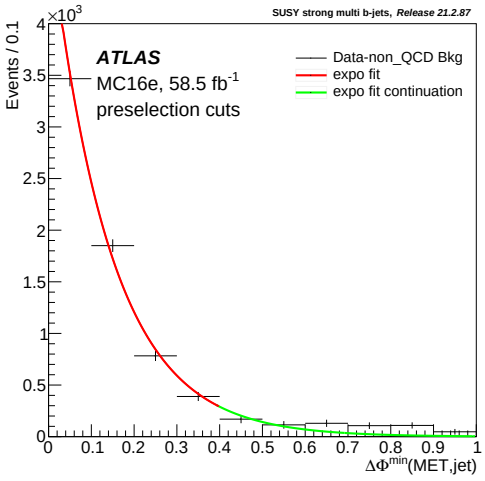

(c)

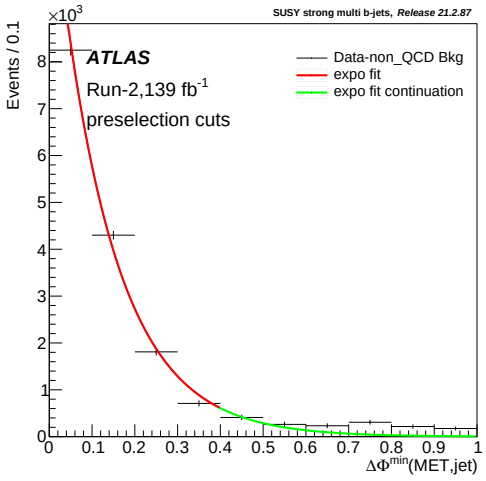

(d)

Figure 6.3: The $\Delta\phi_{\text{min}}^{\text{4j}}$ distribution and exponential fit results for (a) mc16a, (b) mc16d, (c) mc16e, and inclusively for all Run2 data. The shape of this distribution is used to extract a normalization as described in subsection 6.5.1.

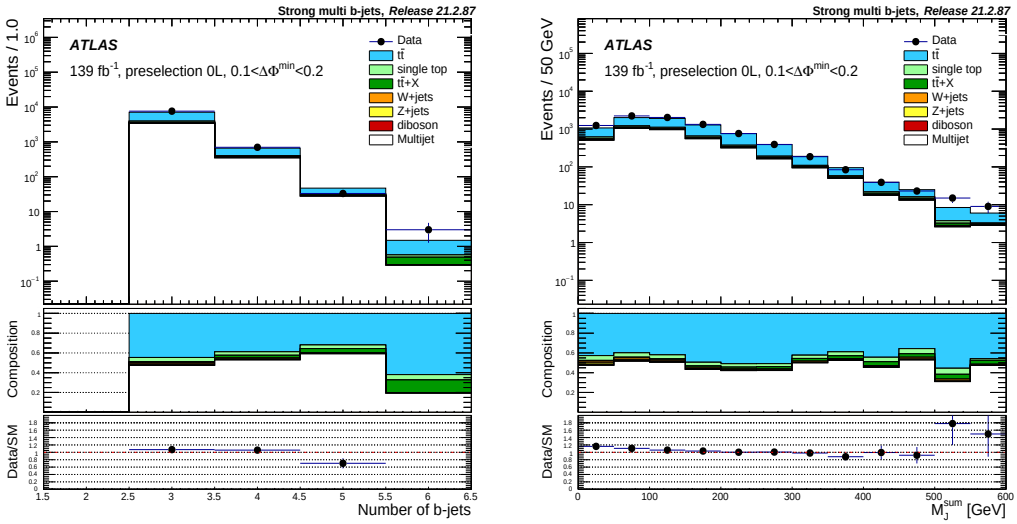

Figure 6.4: Comparison of the distributions of (a) N_{jet}, (b) M_J^{Σ}, (c) $E_{\text{T}}^{\text{miss}}$, and (d) $m_{\text{eff}}^{\text{incl}}$ in data and the corresponding background prediction, in a region defined by the selections: 0 leptons, $N_{\text{jet}} \geq 4$, $E_{\text{T}}^{\text{miss}} > 200$ GeV, and $0.1 < \Delta\phi_{\text{min}}^{4\text{j}} < 0.2$.

6.5.2 Data-MC comparison in the 0-leptons channel

This subsection contains the pre-fit distributions of the analysis observables in the loose selection 0-lepton channel. As discussed in Section 6.5, the 0-lepton channel requires no selected signal lepton, $E_{\mathrm{T}}^{\mathrm{miss}}$ trigger with $E_{\mathrm{T}}^{\mathrm{miss}} > 200$ GeV, and $\Delta\phi_{\mathrm{min}}^{4\mathrm{j}} > 0.4$ to suppress the multijet background. The pre-fit distributions of discriminating variables are shown in Figures 6.5 and 6.6.

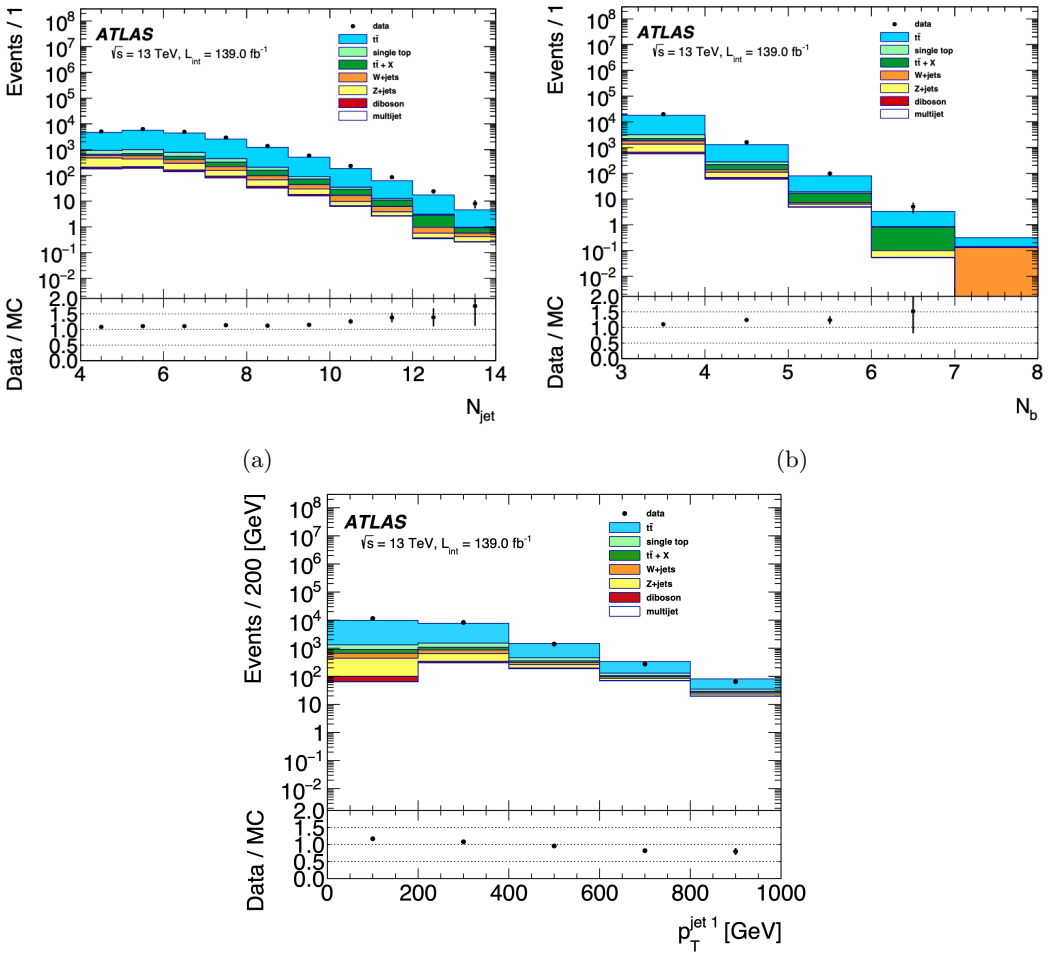

(a) (b)

(c)

Figure 6.5: Distributions of (a) the number of jets, (b) b-jets, and (c) the leading jet p_{T} for events passing preselection 0-lepton requirements. Only the statistical uncertainty is included in each of these plots. The ratio of data to the total background prediction is shown in the lower part of each plot. The data included in these plots were recorded during the 2015–2018 pp collisions data taking periods.

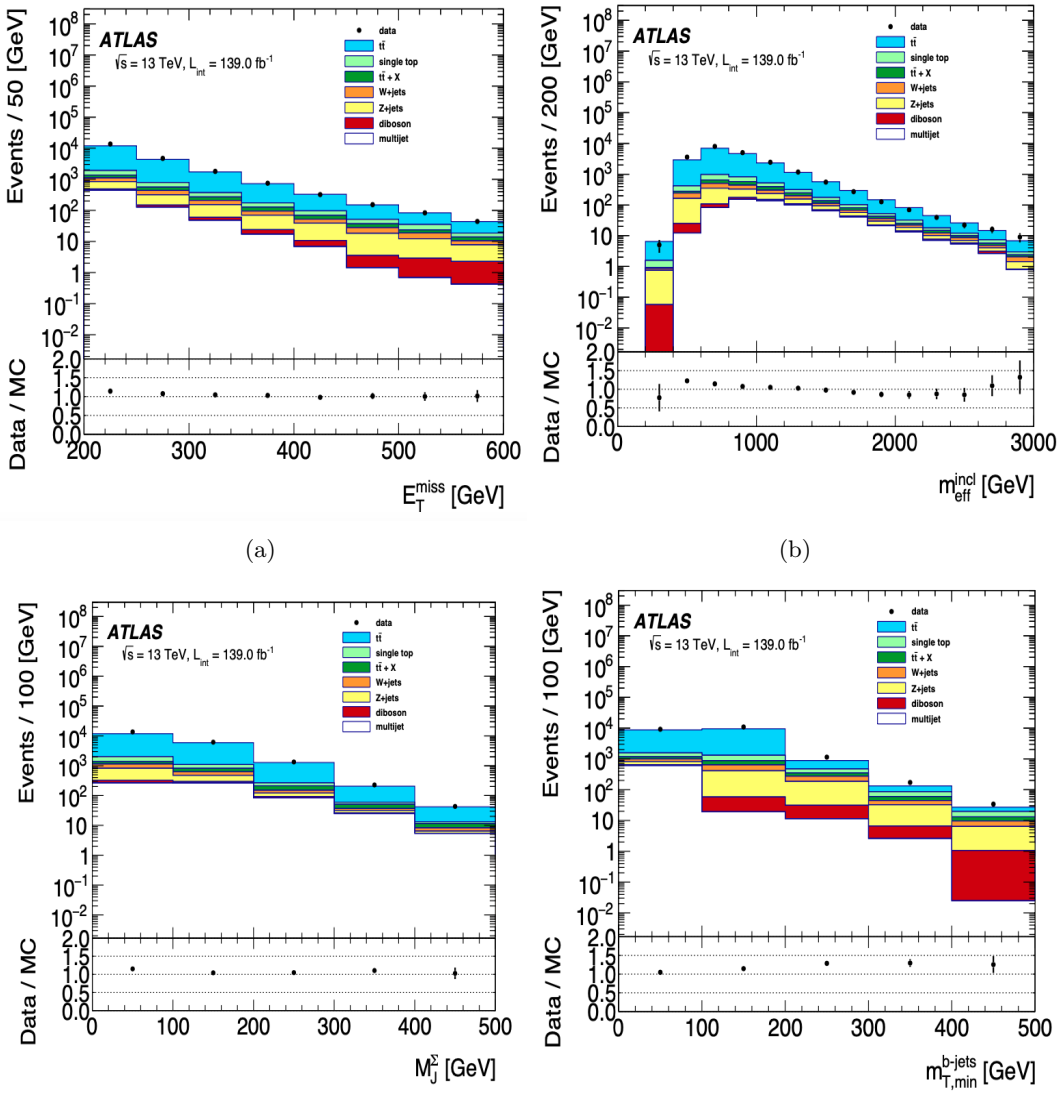

(a) (b)

(c) (d)

Figure 6.6: Distributions of (a) $E_{\mathrm{T}}^{\mathrm{miss}}$, (b) $m_{\mathrm{eff}}^{\mathrm{incl}}$, (c) $m_{\mathrm{T,\,min}}^{b-\mathrm{jets}}$, and (d) $M_J^{\sum}$ for events passing preselection 0-lepton requirements. Only the statistical uncertainty is included in each of these plots. The ratio of data to the total background prediction is shown in the lower part of each plot. The data included in these plots were recorded during the 2015–2018 *pp* collisions data taking periods.

6.5.3 Kinematic Reweighting in 1-lepton channel

The modelling of several energy-related kinematic variables in data and MC shows a moderate disagreement in the high-$m_{\text{eff}}^{\text{incl}}$ region in the $\geq$ 1-lepton channel. As shown in the distributions of $m_{\text{eff}}^{\text{incl}}$ and $E_{\text{T}}^{\text{miss}}$ in Figure 6.7, overestimation is visible in the tail of the data-MC ratio.

In order for the MC predictions to better model the observed data in the high-$m_{\text{eff}}^{\text{incl}}$ tail, a reweighting strategy has been derived based on the distribution of $m_{\text{eff}}^{\text{incl}}$. The reweighting functions are derived separately in a set of orthogonal control regions enriched in various processes such as $t\bar{t}$, single-top, W+jets, and Z+jets. Further details on these control regions and reweighting functions are provided in Appendix A. Comparisons of kinematic variables before and after applying reweighting scale factors in the 1L preselection region are shown in Figures 6.8, 6.9, and 6.10.

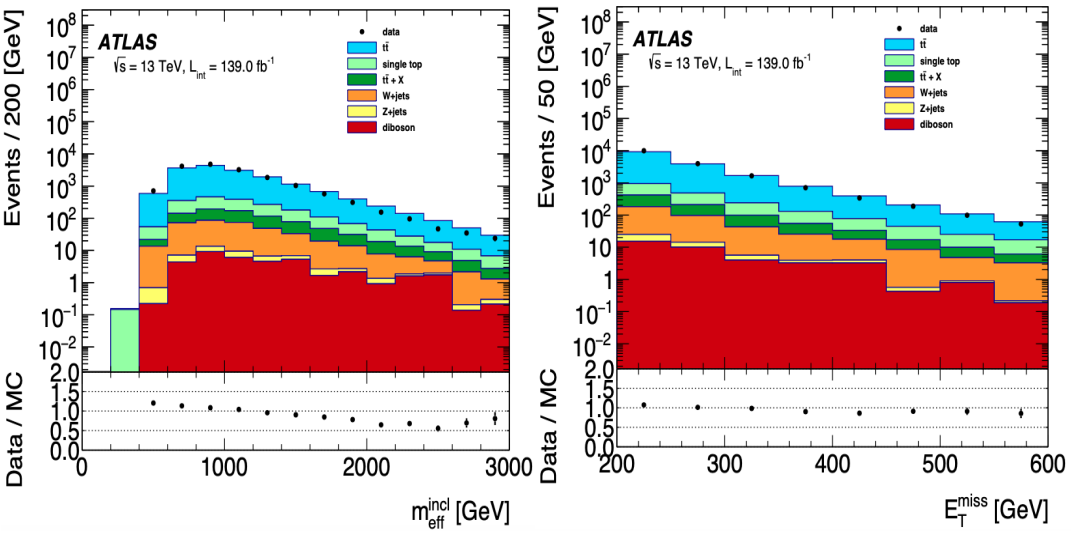

(a) (b)

Figure 6.7: Distributions of (a) $m_{\text{eff}}^{\text{incl}}$, and (b) $E_{\text{T}}^{\text{miss}}$ before kinematic reweighting.

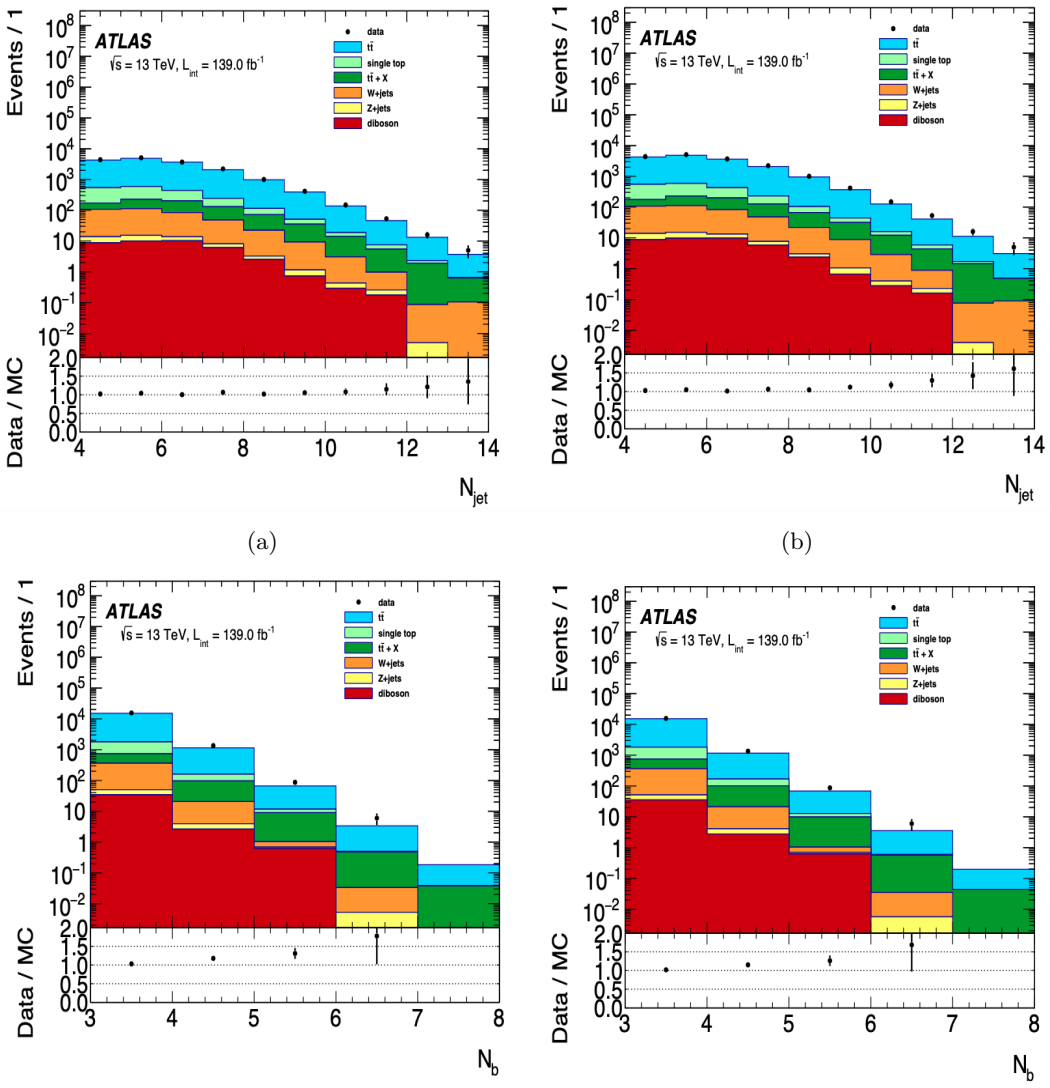

(a) (b)

(c) (d)

Figure 6.8: Distributions of N_{jet} (a) before, and (b) after kinematic reweighting; and distributions of $N_{b-\text{jet}}$ (c) before, and (d) after kinematic reweighting.

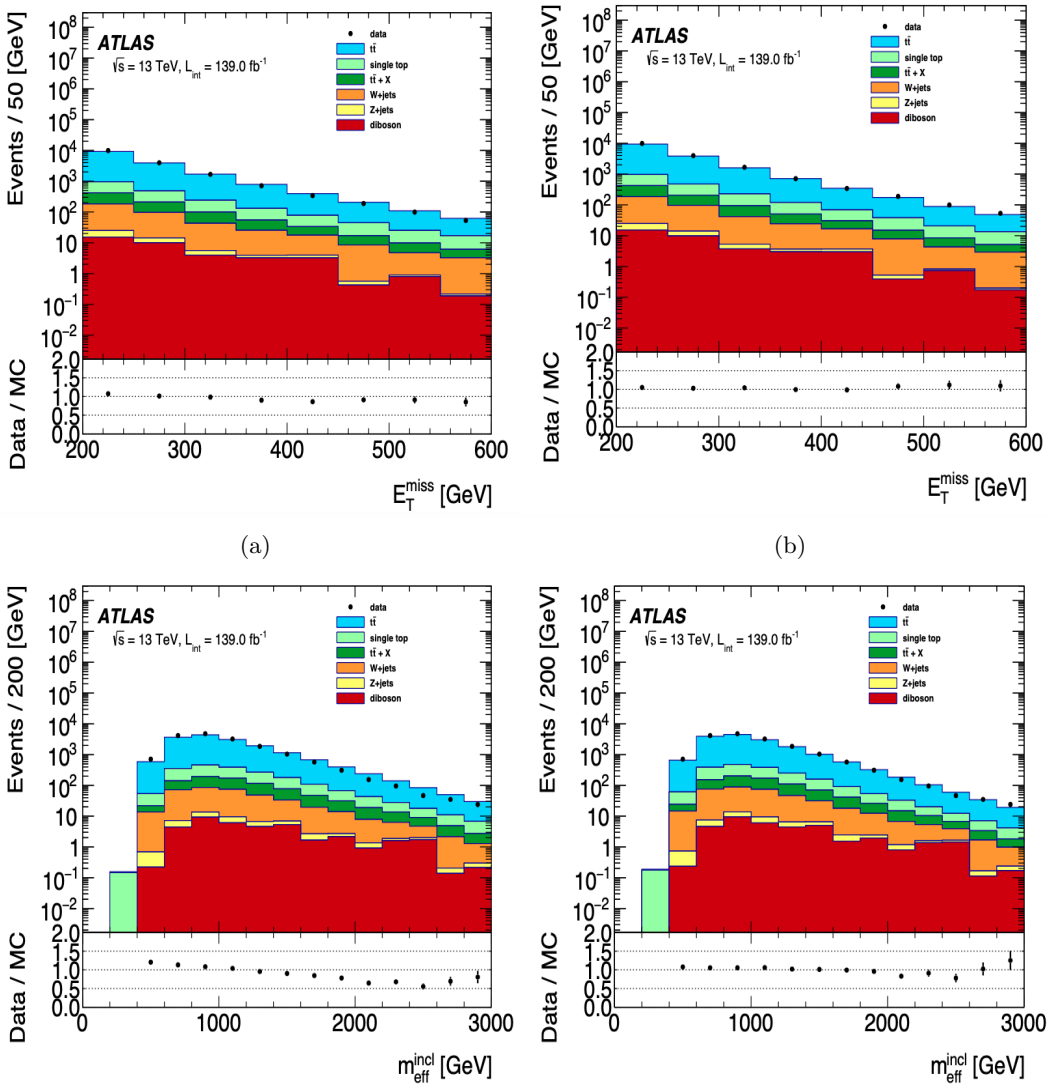

Figure 6.9: Distributions of $E_{\mathrm{T}}^{\mathrm{miss}}$ (a) before, and (b) after kinematic reweighting; and distributions of $m_{\mathrm{eff}}^{\mathrm{incl}}$ (c) before, and (d) after kinematic reweighting.

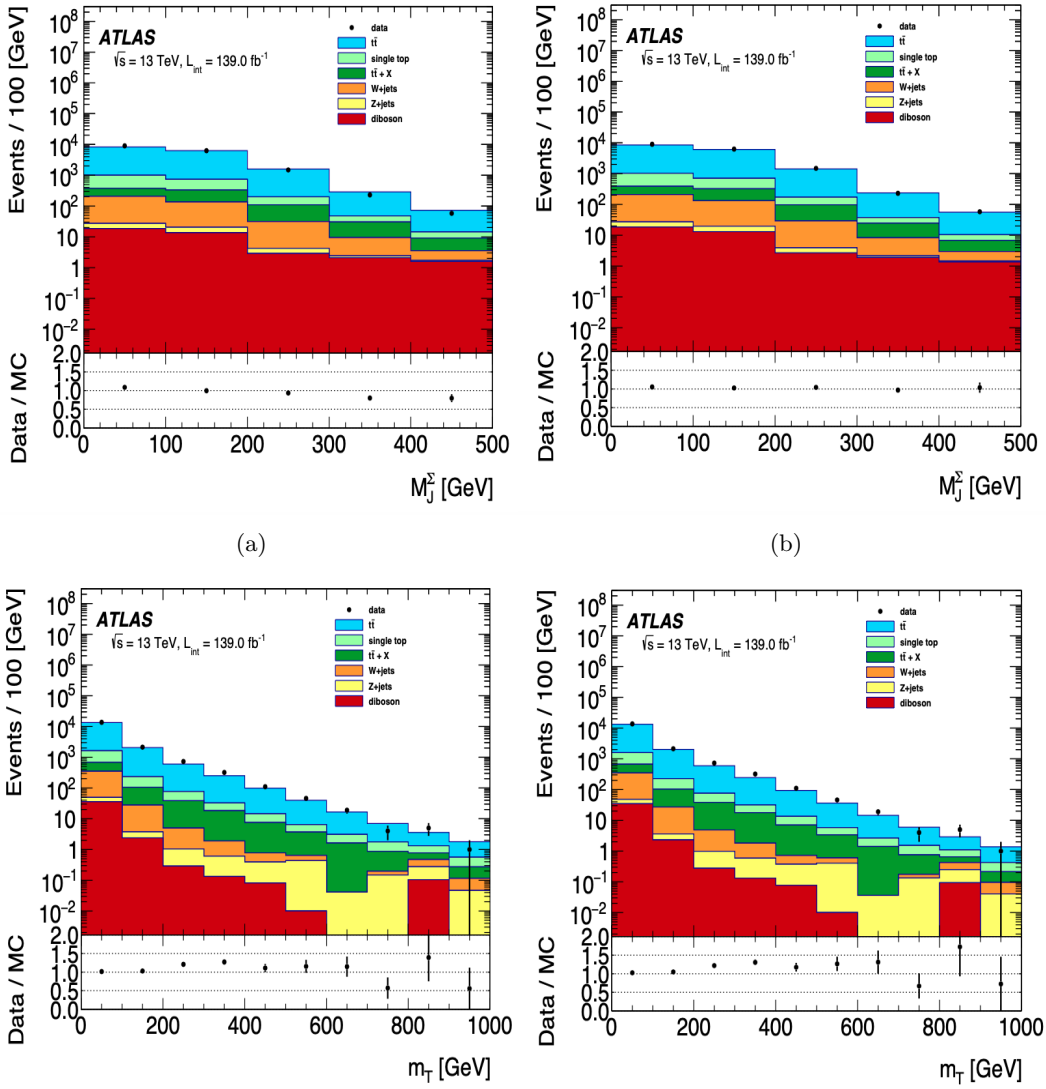

(a) (b)

(c) (d)

Figure 6.10: Distributions of M_J^{Σ} (a) before, and (b) after kinematic reweighting; and distributions of m_{T} (c) before, and (d) after kinematic reweighting.

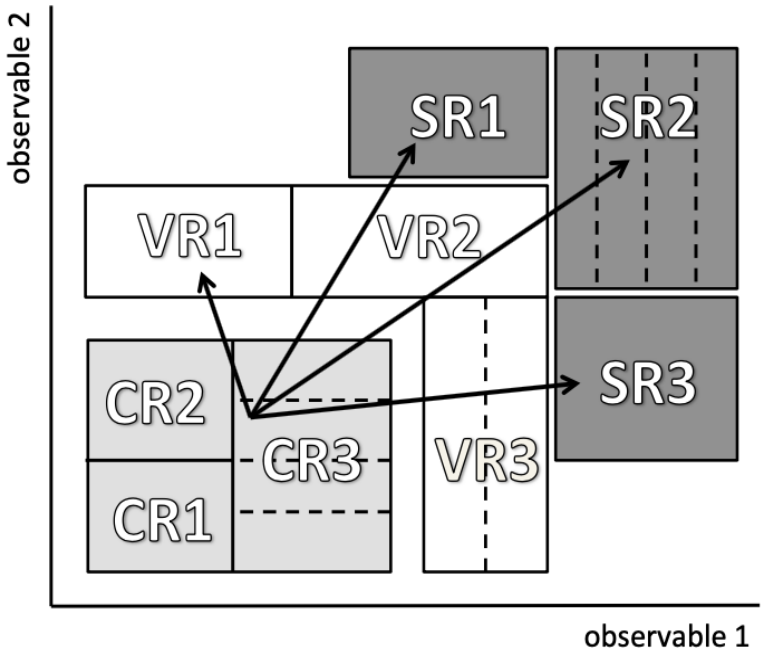

Figure 6.11: Schematic view of an analysis extrapolation strategy from the CR to the SR. Figure from [143].

6.6 Analysis Strategy

In this analysis, multiple signal-enriched regions (SRs) sensitive to various signal benchmarks are optimized. A key aspect is how to estimate the expected number of background events in the SRs. The main background in all these SRs is $t\bar{t}$ pairs in association with heavy and light flavour jets. In each SR, the $t\bar{t}$ normalization factor ($\mu_{t\bar{t}}$) is derived in a dedicated CR which is enriched in $t\bar{t}$ composition with very low signal contribution. To cross-check the extrapolation of $t\bar{t}$ normalization from CRs to SRs, validation regions (VRs) with similar background composition are defined. Figure 6.11 represents the extrapolation strategy used in this analysis.

The estimation of non-$t\bar{t}$ backgrounds, consisting of V+jets, single-top, $t\bar{t}+V$, and diboson events, is derived from MC simulation. The multijet background estimation relies on the data-driven method that was discussed in subsection 6.5.1. (We find that the multijet yields in the SRs are negligible).

To define the analysis SRs, a **cut-and-count** approach is used. In this method, the SR are optimized to maximize the expected discovery significance for benchmark signal models (see subsection 6.6.1). Cut-and-count SRs are then used as the inputs for profile likelihood fits to search for the existence of

potential new physics (see Chapter 7).

6.6.1 Cut-and-count regions

In this Section, the optimization of the SRs, and the definition of the CRs and VRs for Gtt-0lepton, Gtt-1lepton, and Gbb are discussed. The same procedure was used in the previous iteration of this analysis [144, 145].

Signal regions

As discussed in Section 6.6, the SRs in the cut-and-count strategy are designed to maximize the expected significance, which is calculated using **Binomial-ExpZ** [146] from the RooStats statistical package [147]. The optimization of the SRs requires at least 0.5 expected background events, at least 2 expected signal events in each benchmark signal, and $t\bar{t}$ as the dominant background composition. The variables used in the optimization are N_{jet}, $N^{b-\text{jet}}$, $m_{\text{eff}}^{\text{incl}}$, $E_{\text{T}}^{\text{miss}}$, $m_{\text{T, min}}^{b-\text{jets}}$, and m_{T}. In each signal grid point, the set of optimal selections which maximize the expected significance are used to define the SRs. See Appendix B for more details on SR optimization.

Optimizations are performed separately for Gtt-0L, Gtt-1L and Gbb; and three different SRs are defined based on the mass splitting (Δm) between the gluino and neutralino. A boosted (B) region is constructed, which targets signal events with high mass splitting, leading to highly boosted objects in the final state. This region requires placing a tighter cut on the $m_{\text{eff}}^{\text{incl}}$. Conversely, the compressed (C) region focuses on signal models with soft gluino decay products due to the small Δm. To improve acceptance for softer signal models, most of the variable selections such as $m_{\text{eff}}^{\text{incl}}$ and $E_{\text{T}}^{\text{miss}}$ are relaxed by going from B to C. The Moderate (M1, M2) regions target the signal models with intermediate mass splitting. By definition, M1 aims for a higher mass splitting when compared with M2 (as an example, M1 uses the selection $900 \leq \Delta m \leq 1800$ GeV and M2 $400 < \Delta m < 900$ GeV for Gtt-0L). Figure 6.12 shows the phase space division into three regions based on Δm. All cut-and-count SRs probing the different signal models are described in Tables 6.3, 6.4, and 6.5.

Control and Validation regions

The cut-and-count CRs are designed to be kinematically compatible and have no overlap to the SRs, and have dominant $t\bar{t}$ background to accurately extract

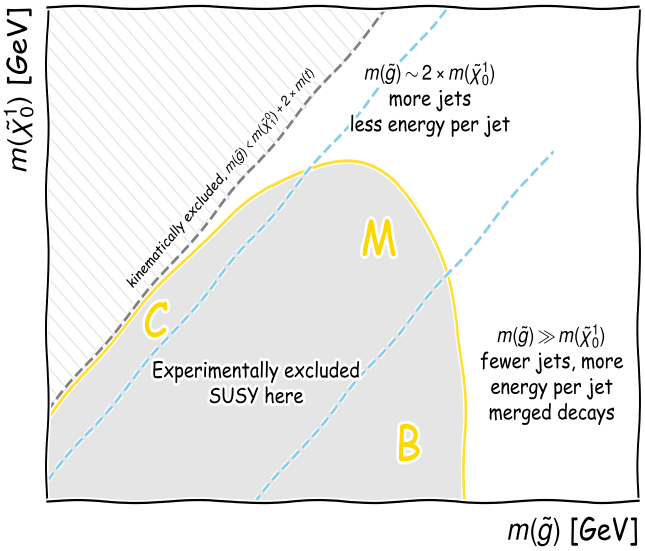

Figure 6.12: Schematic of the cut-and-count analysis for both 0L and 1L channels.

the $t\bar{t}$ normalization factor. The dominant background is semi-leptonic $t\bar{t}$ events where the lepton is outside of the kinematic acceptance, or is a hadronically-decaying τ-lepton (all-hadronic $t\bar{t}$ events do not produce a neutrino in the final state, and thus cannot pass the $E_{\mathrm{T}}^{\mathrm{miss}}$ requirement in analysis regions). The CRs are required to have at least one signal lepton, and an upper cut on m_{T} both to make them non-overlapping with the SRs and to increase the $t\bar{t}$ fraction. Other selections such as $m_{\mathrm{eff}}^{\mathrm{incl}}$, $E_{\mathrm{T}}^{\mathrm{miss}}$, and M_J^{Σ} are relaxed to ensure enough statistics (i.e., at least 10 expected background events).

The VRs are kinematically close to the corresponding SRs and non-overlapping with both the CRs and SRs. In the Gtt-1L region, there are two VRs: VR-m_{T} which validates the extrapolation to high m_{T}, and VR-$m_{\mathrm{T,\,min}}^{b-\mathrm{jets}}$ which checks the background prediction in the high $m_{\mathrm{T,\,min}}^{b-\mathrm{jets}}$ region. An inverted selection on M_J^{Σ} or m_{T} avoids any overlap between the set of events that are contained in the VRs, and the set of events that are contained either in the SRs or in the CRs. The cut-and-count region definitions for Gtt-0L, Gtt-1L, and Gbb are given in Tables 6.3, 6.4, and 6.5.

Background composition

As discussed in Section 6.6, the CRs and VRs are designed to normalize the dominant background (which is $t\bar{t}$ in this analysis) and to validate the extra-

polation process within regions close to the SRs. This is more robust when $t\bar{t}$ composes a larger fraction of the total background. Figures 6.13, 6.14, and 6.15 show the pre-fit background composition in the cut-and-count regions. In general, $t\bar{t}$ and single-top have the largest background composition in most regions.

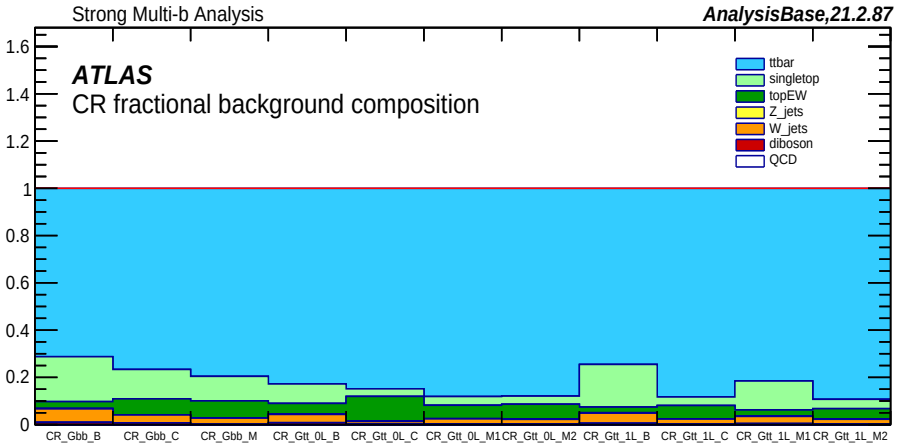

Figure 6.13: Pre-fit background composition in the cut-and-count control regions.

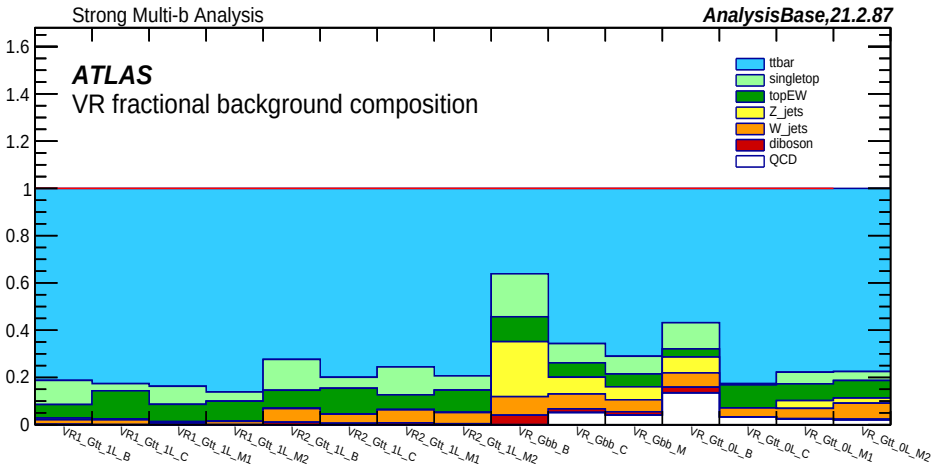

Figure 6.14: Pre-fit background composition in the cut-and-count validation regions.

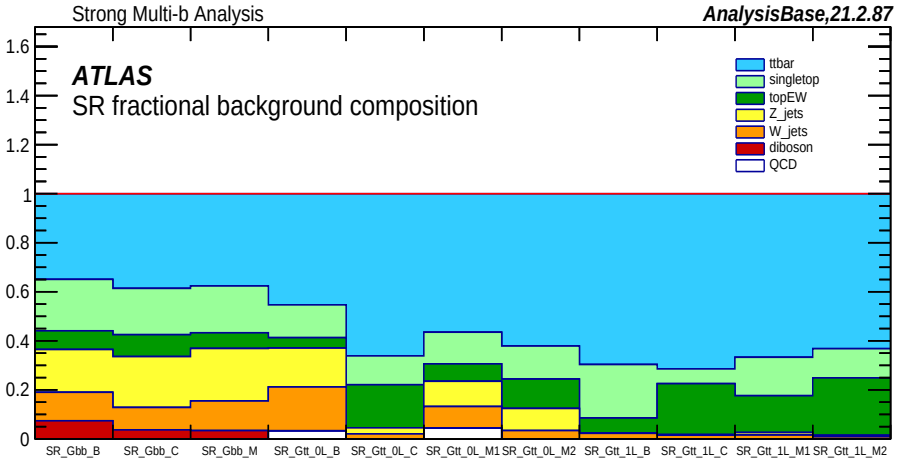

Figure 6.15: Pre-fit background composition in the cut-and-count signal regions.

Table 6.3: Definitions of the Gtt 0-lepton SRs, CRs and VRs of the cut-and-count analysis. All kinematic variables are expressed in GeV except $\Delta\phi_{\text{min}}$, which is in radians. The jet p_{T} requirement is also applied to all signal jets.

Gtt 0-lepton

Criteria common to all regions: $p_{\text{Tjet}} > 30$ GeV

Targeted kinematics	Type	N_{lepton}	N_{jet}	$N^{b-\text{jet}}$	$E_{\text{T}}^{\text{miss}}$	$\Delta\phi_{\text{min}}$	$m_{\text{eff}}^{\text{incl}}$	m_{T}	$m_{\text{T,min}}^{\text{b-jets}}$	M_J^{Σ}
Region B (Boosted, Large Δm)	SR	$= 0$	≥ 5	≥ 3	≥ 600	≥ 0.4	≥ 2900	–	≥ 120	≥ 300
	CR	$= 1$	≥ 4	≥ 3	≥ 200	–	≥ 2000	< 150	–	≥ 150
	VR	$= 0$	≥ 5	≥ 3	≥ 250	≥ 0.4	≥ 2000	–	–	< 300
Region M (Moderate-1 Δm)	SR	$= 0$	≥ 9	≥ 3	≥ 600	≥ 0.4	≥ 1700	–	≥ 120	≥ 300
	CR	$= 1$	≥ 8	≥ 3	≥ 200	–	≥ 1100	< 150	–	≥ 150
	VR	$= 0$	≥ 9	≥ 3	≥ 300	≥ 0.4	≥ 1400	–	–	< 300
Region M (Moderate-2 Δm)	SR	$= 0$	≥ 10	≥ 3	≥ 500	≥ 0.4	≥ 1100	–	≥ 120	≥ 200
	CR	$= 1$	≥ 9	≥ 3	≥ 200	–	≥ 800	< 150	–	≥ 100
	VR	$= 0$	≥ 10	≥ 3	≥ 300	≥ 0.4	≥ 800	–	–	< 200
Region C (Compressed, small Δm)	SR	$= 0$	≥ 10	≥ 4	≥ 400	≥ 0.4	≥ 800	–	≥ 180	≥ 100
	CR	$= 1$	≥ 9	≥ 4	≥ 200	–	≥ 800	< 150	–	≥ 100
	VR	$= 0$	≥ 10	≥ 4	≥ 200	≥ 0.4	≥ 800	–	–	< 100

Table 6.4: Definitions of the Gtt 1-lepton SRs, CRs and VRs of the cut-and-count analysis. All kinematic variables are expressed in GeV except $\Delta\phi_{\text{min}}$, which is in radians. The jet p_{T} requirement is also applied to all signal jets.

Gtt 1-lepton							
Criteria common to all regions: $N_{\text{lepton}} \geq 1$, $p_{\text{T}} > 30$ GeV, $N^{b-\text{jet}} \geq 3$							
Targeted kinematics	Type	N_{jet}	$E_{\text{T}}^{\text{miss}}$	$m_{\text{eff}}^{\text{incl}}$	m_{T}	$m_{\text{T,min}}^{\text{b-jets}}$	M_J^{Σ}
Region B (Boosted, Large Δm)	SR	≥ 4	≥ 600	≥ 2300	≥ 150	≥ 120	≥ 200
	CR	$= 4$	≥ 200	≥ 1500	< 150	–	–
	VR-m_{T}	≥ 4	≥ 200	≥ 1500	≥ 150	–	< 200
	VR-$m_{\text{T,min}}^{\text{b-jets}}$	> 4	≥ 200	≥ 1200	< 150	≥ 120	< 200
Region M (Moderate-1 Δm)	SR	≥ 5	≥ 600	≥ 2000	≥ 200	≥ 120	≥ 200
	CR	$= 5$	≥ 200	≥ 1200	< 200	–	–
	VR-m_{T}	≥ 5	≥ 200	≥ 1200	≥ 200	–	< 200
	VR-$m_{\text{T,min}}^{\text{b-jets}}$	> 5	≥ 200	≥ 1000	< 200	≥ 120	≥ 100
Region M (Moderate-2 Δm)	SR	≥ 8	≥ 500	≥ 1100	≥ 200	≥ 120	≥ 100
	CR	$= 8$	≥ 200	≥ 800	< 200	–	–
	VR-m_{T}	≥ 8	≥ 200	≥ 800	≥ 200	–	< 100
	VR-$m_{\text{T,min}}^{\text{b-jets}}$	> 8	≥ 200	≥ 800	< 200	≥ 120	≥ 100
Region C (Compressed, small Δm)	SR	≥ 9	≥ 300	≥ 800	≥ 150	≥ 120	–
	CR	$= 9$	≥ 200	≥ 800	< 150	–	–
	VR-m_{T}	≥ 9	≥ 200	≥ 800	≥ 150	< 120	–
	VR-$m_{\text{T,min}}^{\text{b-jets}}$	> 9	≥ 200	≥ 800	< 150	≥ 120	–

Table 6.5: Definitions of the Gbb SRs, CRs and VRs of the cut-and-count analysis. All kinematic variables are expressed in GeV except $\Delta\phi_{\text{min}}$, which is in radians. The jet p_{T} requirement is also applied to all signal jets.

Gbb							
Criteria common to all regions: $N_{\text{jet}} \geq 4$, $N^{b-\text{jet}} \geq 3$, $\Delta\phi_{\text{min}} > 0.4$							
Targeted kinematics	Type	N_{lepton}	p_{T}	$m_{\text{eff}}^{\text{incl}}$	$E_{\text{T}}^{\text{miss}}$	$m_{\text{T,min}}^{\text{b-jets}}$	m_{T}
Region B (Boosted, Large Δm)	SR	$= 0$	> 65	> 2600	> 550	> 130	
	CR	$= 1$	> 65	> 2600	> 550		< 200
	VR	$= 0$	> 65	< 2400	> 550	> 130	
Region M (Moderate Δm)	SR	$= 0$	> 20	> 2000	> 550	> 130	
	CR	$= 1$	> 20	> 2000	> 400		< 250
	VR	$= 0$	> 20	> 1600	< 500	> 80	
Region C (Compressed, small Δm)	SR	$= 0$	> 20	> 1600	> 550	> 130	
	CR	$= 1$	> 20	> 1600	> 450		< 200
	VR	$= 0$	> 20	> 1500	< 450	> 130	

6.7 Analysis Uncertainties

This analysis is affected by statistical and systematic uncertainties which need to be estimated accurately. Statistical (random) uncertainties are due to the finite size of data or MC samples, and are approximated by the square root of the number of events $\sqrt{N}$ (e.g., the number of data events collected by the ATLAS detector).

The systematic uncertainties are categorized as experimental (detector-related) or theoretical. The first category comes from the imperfect modelling of the detector performance in MC simulation, for example uncertainties on the modelling of the final measurable objects. For the theory systematics, various theoretical models are used for simulated event generation, hadronization, and initial-final state radiation. A summary of the largest experimental and theoretical uncertainties in this measurement will be presented in the following.

6.7.1 Experimental Systematic Uncertainties

Each of the final objects in this analysis are calibrated to accurately describe the data, and the recommendations from the dedicated performance groups are used to estimate the uncertainty due to modelling in the simulation. Variations of systematic parameters by one standard deviation ($\pm 1\sigma$) are used to determine the effect of systematics. Various sources of experimental systematic uncertainties in this analysis are summarized below:

Jets

In this analysis, the largest sources of experimental uncertainties are the ones which change jet kinematics, such as jet energy scale (JES) and jet energy resolution (JER). As discussed in subsection 5.2.2, by applying the JES, the energies of reconstructed jets are corrected to the particle-level energy scale. A set of nuisance parameters (NPs) is used for the JES uncertainty calculation [148].

In dijet events, the asymmetry distribution [149] between the reference and probe jets can be used to probe the JER ($\frac{\sigma p_{\mathrm{T}}}{p_{\mathrm{T}}}$):

$$\sigma_A^{\mathrm{probe}} = \left\langle \frac{\sigma_{p_{\mathrm{T}}}}{p_{\mathrm{T}}} \right\rangle_{\mathrm{probe}} \oplus \left\langle \frac{\sigma_{p_{\mathrm{T}}}}{p_{\mathrm{T}}} \right\rangle_{\mathrm{ref}} , \tag{6.6}$$

where $\sigma_{p_{\mathrm{T}}}^{\mathrm{probe}}$ and $\sigma_{p_{\mathrm{T}}}^{\mathrm{ref}}$ are respectively the standard deviations of $p_{\mathrm{T}}^{\mathrm{probe}}$ and $p_{\mathrm{T}}^{\mathrm{ref}}$, $\sigma_{A}^{\mathrm{probe}}$ is the standard deviation of the asymmetry distribution, and $\bigoplus$ denotes a sum in quadrature. The JER uncertainty is measured by considering the difference between the calibration derived with the nominal simulation, and a calibration derived with a smeared simulation using a Gaussian function with width set to the JER.

To correct for the residual difference between the b-tagging efficiency in simulation and data, a scale factor is applied to each simulated event. Di-leptonic $t\bar{t}$ events are used to derive the scale factors, which are functions of the jet p_{T}, η, and truth flavor. Several sources of experimental and modelling uncertainties, such as radiation, generator, and fragmentation dependence, affect these scale factors. The b-tagging efficiency scale factors are varied within their uncertainties to evaluate the uncertainty in the tagging efficiency in this analysis.

Leptons

The systematic uncertainties associated with electrons and muons, and specifically related to efficiencies of electron and muon reconstruction, identification, and isolation, are found to be negligible. Muon momentum scale factors are applied to correct the reconstructed transverse momenta in the MS and ID in MC events to the distribution of the same quantity in data events. The muon momentum scale has many sources of uncertainties and is measured to be 0.05% to 0.2% depending on the rapidity [150]. Muon momentum resolution is applied to smear the relative simulated transverse momentum ($\sigma(p_{\mathrm{T}})/p_{\mathrm{T}}$) to properly match the data, and is measured to be 5% for muons in $|\eta|< 1.05$ with $p_{\mathrm{T}} = 100$ GeV. The impact of electron and muon energy scale-resolution uncertainties on the analysis are assessed by re-running the fit programs with $\pm 1\sigma$ variation on these energy scales in each of the regions.

Luminosity

The luminosity measurement in ATLAS is performed by the forward luminometers located far away from the IP. The LUCID detector [151], as the primary ATLAS luminometer, contains 16 PMTs and is placed next to the beamline at approximately 17 m from the IP. When a particle passes through the quartz windows of the PMTs, it produces Cherenkov light, which is then read out with dedicated electronics as a hit. Luminosity is further calibrated with the van

der Meer (vdM) method [152] which is a scan of the two beams in the $x - y$ directions to measure the visible pp cross-section (σ_{vis}). The systematic uncertainty on the integrated luminosity for 139 fb^{-1} data collected is measured to be 1.7% (using techniques described in [57]).

Missing Transverse Energy

The systematic uncertainties associated with $E_{\text{T}}^{\text{miss}}$ are separated into uncertainties on $E_{\text{T}}^{\text{miss}}$ scale and resolution. The average and root mean square of the projection of the soft term ($p_{\text{T}}^{\text{soft}}$) onto the hard scatter term ($p_{\text{T}}^{\text{hard}}$) are used to determine the uncertainties for the $E_{\text{T}}^{\text{miss}}$ scale and resolution [153].

6.7.2 Theoretical Systematic Uncertainties

The theory systematic uncertainties are estimated by comparison between the nominal MC samples with the systematic MC samples, the latter of which are simulated by variation of generator parameters. The theory systematic derivations for $t\bar{t}$+jet and single-top quark backgrounds are described below (based on the ATLAS SUSY recommendations [154]):

Top quark pair-production

Three sources of uncertainties on the modelling of the $t\bar{t}$+jet process are: the generator, the parton showering and hadronization, and the initial-state (ISR) or final-state radiation (FSR). The uncertainty arising from the choice of the MC generator is evaluated by comparing the nominal POWHEG sample to the systematic one generated with MADGRAPH5. Both samples are interfaced to PYTHIA for parton showering. The systematic uncertainty associated with the choice of parton showering and hadronization algorithm is estimated by comparing the nominal sample (showered with PYTHIA) to one showered using HERWIG++. Comparison between the nominal sample (containing two POWHEG samples showered in PYTHIA) with different configurations is used to evaluate the systematic uncertainties due to the modelling of ISR and FSR. The high and low PYTHIA settings correspond to variation of the renormalization and factorization scales, which lead to higher or lower amounts of ISR/FSR. The cross section production for $t\bar{t}$ in association with heavy flavour jets ($t\bar{t}+ \geq 1b$ or $t\bar{t}+ \geq 1c$) is measured in ATLAS with 30% uncertainty [155]. The $t\bar{t}$ cross section uncertainty is assigned as an additional uncertainty in this analysis.

Figures 6.16 and 6.17 show the distributions of the number of signal jets and $m_{\text{eff}}^{\text{incl}}$ in the nominal and systematics-modified $t\bar{t}$ samples.

The modeling uncertainties of the $t\bar{t}$ sample affect the extrapolation from the CRs to the VRs or SRs[4], therefore transfer factors[5] are used to estimate the associated theory uncertainties in the analysis regions. Three main sources of $t\bar{t}$ theory systematics are illustrated in Figure 6.18.

Single-top quark

To estimate modelling uncertainties affecting single-top background, the following comparisons between generators are considered: POWHEG vs. MADGRAPH5 for the matrix elements, PYTHIA vs. HERWIG++ for parton showering and hadronization, and PYTHIA with different sets of configuration (i.e., the variation of the renormalization and the factorization scales) for radiation. Figure 6.19 shows the distributions of the number of signal jets in the nominal and systematics-modified single-top samples. An additional uncertainty arises from the quantum interference between leading-order $t\bar{t}$ production and next-to-leading-order single-top production in the Wt channel. This interference systematic is evaluated by using a dedicated $WWbb$ sample generated at particle level with MADGRAPH5+PYTHIA. The single-top production cross-section uncertainty [156] is also included in the likelihood fit. The four main sources of single-top production theory systematics are illustrated in Figure 6.20.

[4] In the CRs, the $t\bar{t}$ background is normalized by the $t\bar{t}$ scale factor, which is derived from the fit to data.
[5] The transfer factor is defined as the ratio of expected number of background events in the VR or SR to the background yields in the CR.

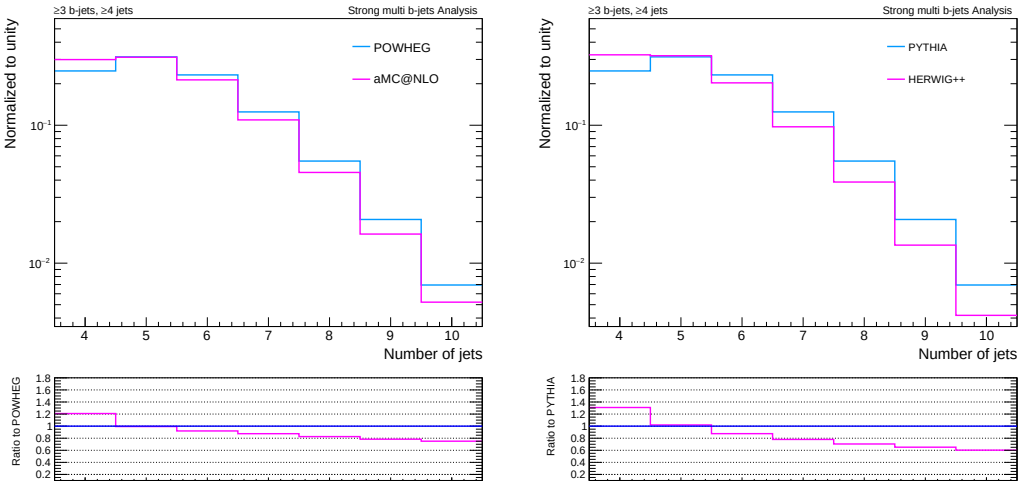

(a)

(b)

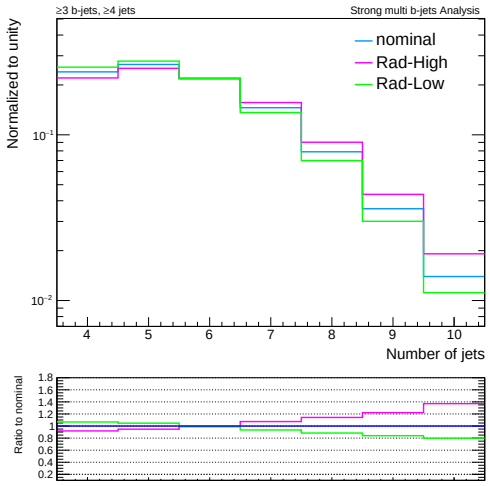

(c)

Figure 6.16: The normalized distributions of the number of signal jets in the $t\bar{t}$ nominal and systematic-modified samples: (a) generator comparison between the nominal POWHEG+PYTHIA (blue line) and systematic-modified MADGRAPH5+PYTHIA (pink line) samples, (b) showering and hadronization comparison between the nominal POWHEG+PYTHIA (blue line) and systematic-modified POWHEG+HERWIG (pink line) samples, (c) radiation comparison between the nominal POWHEG+PYTHIA (blue line) sample and two samples with systematic variations of the renormalization and the factorization scales (pink and green lines).

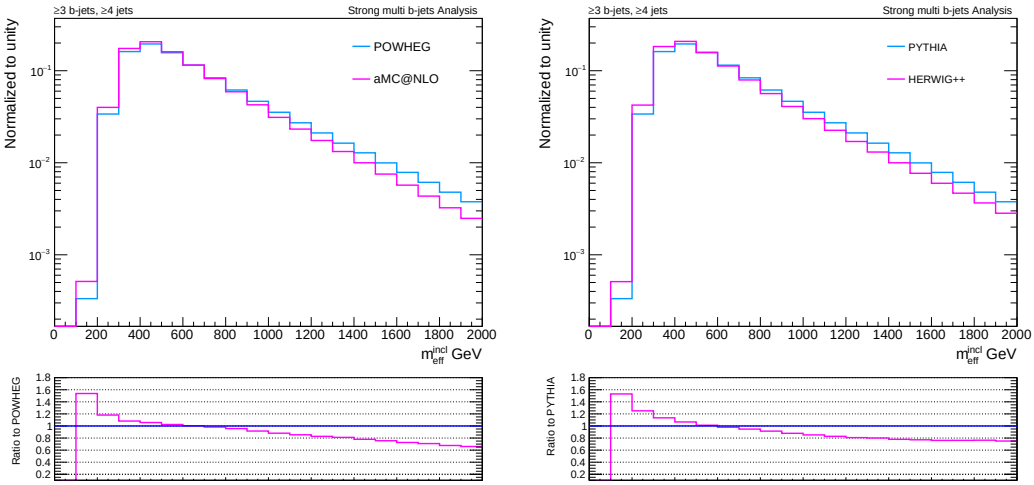

(a)

(b)

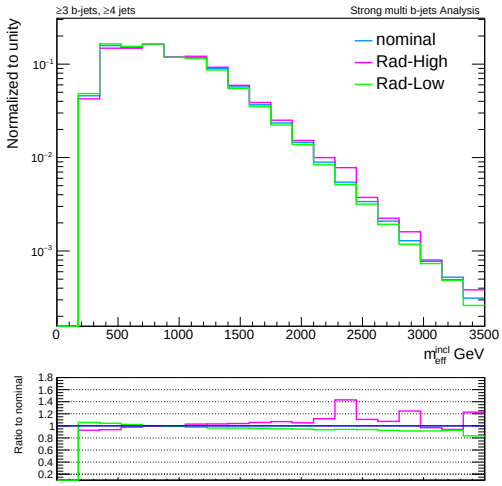

(c)

Figure 6.17: The normalized distributions of $m_{\text{eff}}^{\text{incl}}$ in the $t\bar{t}$ nominal and systematic-modified samples: (a) generator comparison between the nominal POWHEG+PYTHIA (blue line) and systematic MADGRAPH5+PYTHIA (pink line) samples, (b) showering and hadronization comparison between the nominal POWHEG+PYTHIA (blue line) and systematic-modified POWHEG+HERWIG (pink line) samples, (c) radiation comparison between the nominal POWHEG+PYTHIA (blue line) sample and two samples with systematic variations of the renormalization and the factorization scales (pink and green lines).

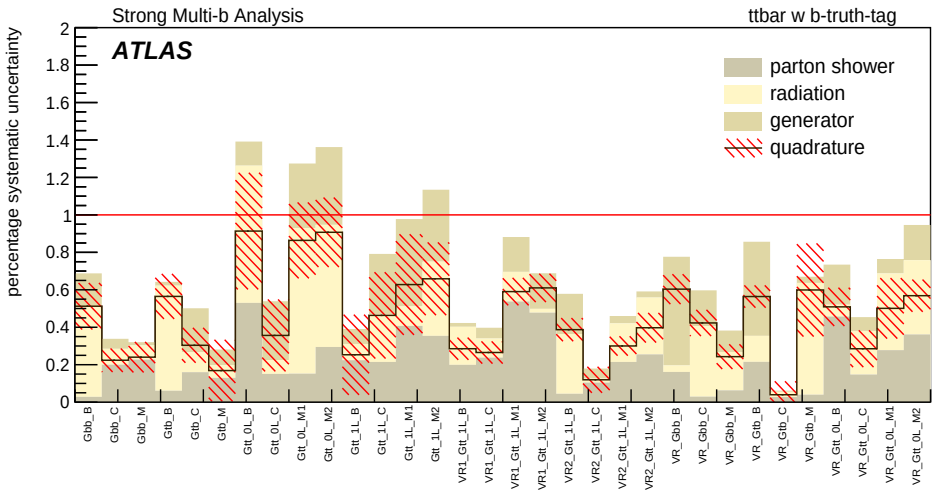

Figure 6.18: Theory systematic components for $t\bar{t}$ background, which are shown as stacked histograms. The quadrature sum of each component and its statistical uncertainty are superimposed as black and shaded red lines. To reduce statistical uncertainty in the comparison between nominal and systematic samples, the truth b-tagging CP tool [157] is used to remove the selection on the number of b-tagged jets, and thus all the events are kept and weighted. This weight can be interpreted as the probability of the given event to contain a given number of b-tagged jets. The size of the uncertainty is in percent.

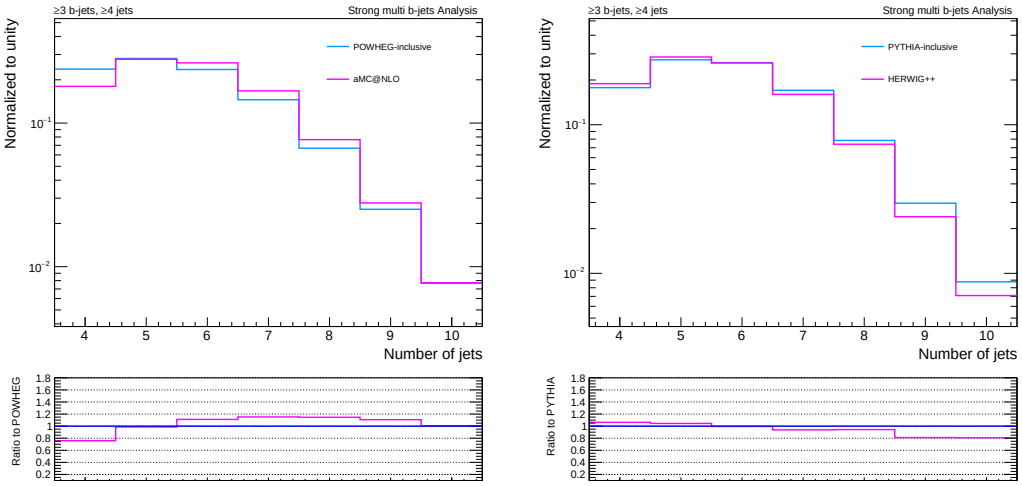

(a)

(b)

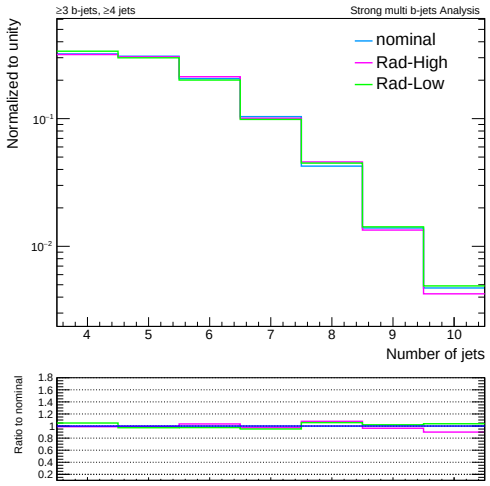

(c)

Figure 6.19: The normalized distributions of the number of signal jets in the single-top quark nominal and systematic-modified samples: (a) generator comparison between the nominal POWHEG+PYTHIA (blue line) and systematic-modified MADGRAPH5+PYTHIA (pink line) samples, (b) showering and hadronization comparison between the nominal POWHEG+PYTHIA (blue line) and systematic-modified POWHEG+HERWIG (pink line) samples, (c) radiation comparison between the nominal POWHEG+PYTHIA (blue line) sample and two samples with systematic variations of the renormalization and the factorization scales (pink and green lines).

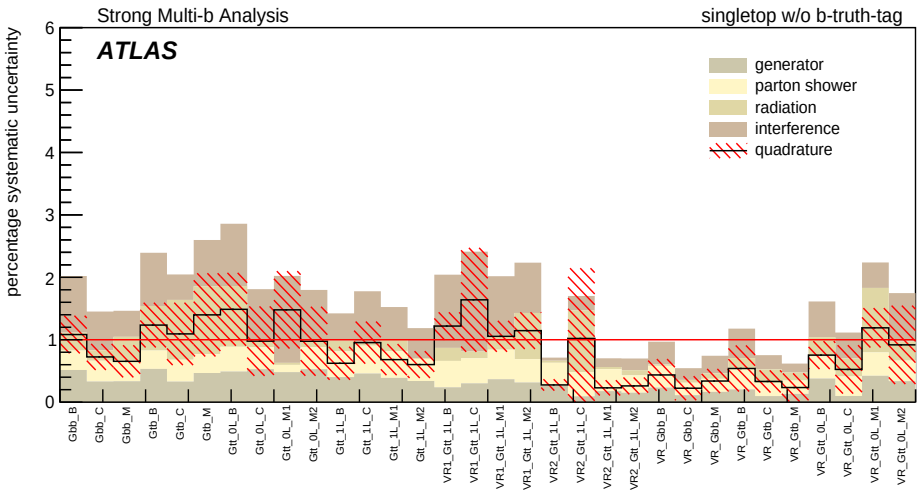

Figure 6.20: Theory systematic components for single-top production background, which are shown as stacked histograms. The quadrature sum of each component and its statistical uncertainty are superimposed as black and shaded red lines. To reduce statistical uncertainty in the comparison between nominal and systematic samples, the truth b-tagging CP tool is used to remove the selection on the number of b-tagged jets, and thus all the events are kept and weighted. This weight can be interpreted as the probability of the given event to contain a given number of b-tagged jets. The size of the uncertainty is in percent.

Chapter 7

Results

This chapter presents the analysis performed to derive and interpret the fit results. A brief introduction to the likelihood used to perform the background-only fit is presented in Section 7.1. Section 7.2 discusses the goal of the background-only fit and the comparison between the observed data and the expected yield of background events in the analysis regions. In the absence of a significant discovery excess, a set of exclusion limits using the CL_s [158] method (see Section 7.3) are derived for the Gtt and Gbb simplified models as a function of the gluino and neutralino masses.

The background-only and exclusion fits are performed within the **HistFitter** program [143]. HistFitter is a statistical framework built on top of the **RooFit** [159] and **HistFactory** [160] packages, and uses the **RooStats** [147] package for statistical fitting and results interpretation.

7.1 Likelihood Function

A central concept in statistics is the probability model, which assigns a probability to each possible experimental outcome. The likelihood function $L(n_{\text{obs}}|H)$ is a function of the probability to observe the data n_{obs} in an experiment for a given hypothesis H. In a composite hypothesis which uses several parameters θ to describe the model, the likelihood function is defined as $L(n_{\text{obs}}|\theta)$. To estimate the values of the model parameters from the data, the maximum likelihood estimation technique [161, 162] is applied.

The likelihood function L considered in this analysis is the product of the Poisson distribution of the number of events in the SRs and CRs, and an

additional term to constrain the systematic uncertainties:

$$L(n, \theta^0 | \mu_{\text{sig}}, b, \theta) = P_{\text{SR}} \times P_{\text{CR}} \times C_{\text{syst}} \quad . \tag{7.1}$$

On the left-hand side of Eq. 7.1, θ represents the nuisance parameters to parametrize the systematic uncertainties, θ^0 is the central value of the auxiliary measurements [1], μ_{sig} is a parameter known as the **signal strength** ($\mu_{\text{sig}} = 0$ is used to denote the background-only hypothesis and $\mu_{\text{sig}} = 1$ corresponds to the signal+background hypothesis), b refers to the number of background events predicted by simulation, and n is the observed number of events within a region. The background prediction (Eq. 7.2) consists of the number of predicted $t\bar{t}$ events normalized by a scale factor $\mu_{t\bar{t}}$, plus the contribution from the remaining backgrounds (i.e., non $t\bar{t}$):

$$b_{\text{pred}} = \mu_{t\bar{t}} b_{t\bar{t}} + b^{\text{pred}}_{\text{other}} \quad . \tag{7.2}$$

On the right-hand side of Eq 7.1, the first two factors describe the Poisson distributions for the numbers of observed events in the signal and control regions:

$$P_{\text{SR}}(n_{\text{obs}} | \lambda_S(\mu_{\text{sig}}, b, \theta)) = \frac{(\lambda_S(\mu_{\text{sig}} s + b_{\text{pred}}, \theta))^{n_{\text{obs}}}}{n_{\text{obs}}!} \times e^{-(\lambda_S(\mu_{\text{sig}} s + b_{\text{pred}}, \theta))} \quad , \tag{7.3}$$

where the Poisson expectation value λ_S depends on the predicted background yield, the signal yield, and the nuisance parameters. As shown in Eq. 7.3, the number of events predicted by simulation in the region (SR or CR), n_{pred}, is the sum of the normalized number of expected signal events $\mu_{\text{sig}} s$ and the predicted background yield b_{pred}.

Systematic uncertainties are estimated using the probability density function $C_{\text{syst}}(\theta^0, \theta)$ within the likelihood function, where θ^0 (the prior value of a calibration constant, divided by its respective uncertainty) can be varied around the analysis-fitted value of that calibration constant, θ. Each one of the systematic uncertainties is described by a Gaussian [2] distribution function with unit width

[1] In a frequentist approach, nuisance parameters (NPs) always must be measured in separate auxiliary measurements (which may be referred to as calibration measurements), rather than marginalizing over expected NP bounds (e.g., from theory, or from other non-purely-experimental sources). For example, in a frequentist approach, luminosity measurements must be made by incorporating additional measured data sensitive to luminosity from the experiment, and/or from other purely-experimental sources, directly within one's fit.

[2] A Gaussian PDF is the default PDF used in HistFitter, however the usage of other probability densities such as a Poisson or a log-normal constraint is also possible.

($\sigma = 1$), and $C_{\text{syst}}(\theta^0, \theta)$ is the product of all of these probability distributions:

$$C_{\text{syst}}(\theta^0, \theta) = \prod_{i \in \text{ all systematics}} \text{Gaussian}(\theta_i^0 - \theta_i) \quad . \tag{7.4}$$

The impact of the variation of each nuisance parameter on its respective expectation value is determined by an interpolation function. There are several interpolation functions defined in HistFactory, such as piecewise linear [3] or piecewise exponential. By default, the 6th-order polynomial interpolation technique is used in HistFitter. More details about interpolation functions can be found in Ref. [160].

7.2 Background-only Fit

Two types of fits (a background-only fit, and a model-dependent signal fit) are used in this dissertation, which differ in their usage of analysis regions (CRs, VRs, and SRs), and their inclusion, or non-inclusion, of a SUSY signal model. In the **background-only fit** [143], only the information from the CRs is used to estimate the background in the VRs and SRs. As discussed in Section 6.6, the CRs are assumed not have any events in common with the SRs and to be free of contributions from any signal processes ($\mu_{\text{sig}} = 0$). The likelihood function [4] is maximized in the fit to derive the parameter of interest (the $t\bar{t}$ normalization factor) and the nuisance parameters. The $t\bar{t}$ normalization factor is then used to obtain the $t\bar{t}$ contribution in the VRs and SRs, while the predictions for other backgrounds (i.e., non $t\bar{t}$) are derived directly from simulation.

Figure 7.1 shows the comparison between the data and background processes in the cut-and-count CRs. The top panel displays the data and SM background yields, and the bottom panel shows the value of the $t\bar{t}$ normalization factor, with its statistical uncertainty, in the corresponding CR. The extrapolation of the background-only fit results to the VRs is shown in Figure 7.2. Similarly, the upper panel of Figure 7.2 presents the data and the events predicted by the fit, and the bottom panel shows the **pull** in each VR. The pull is equal to the difference between the observed, n_{obs}, and expected number of events, n_{pred},

[3] In the piecewise linear interpolation function, the predicted background is a linear function of the nuisance parameter θ, given by: $(b^+ - b^0)\theta$ for $\theta \geq 0$ or $(b^0 - b^-)\theta$ for $\theta < 0$ where b^0 is the nominal background and $b^\pm$ corresponds to $\pm 1\sigma$ background yield.

[4] The likelihood function is given by Eq. 7.1 without the P_{SR} term, since only the CRs are used in the fit.

divided by the total uncertainty, σ_{tot}:

$$\text{pull} = \frac{n_{\text{obs}} - n_{\text{pred}}}{\sigma_{\text{tot}}} \quad , \tag{7.5}$$

where the total uncertainty is the quadrature sum of the total systematic uncertainty σ_{syst} and the statistical uncertainty σ_{stat} (i.e., the Poisson variation on the number of background events). In this case, no significant background mismodelling is observed across the entire set of VRs, and the magnitude of each one of the pulls is less than $2\sigma_{\text{tot}}$.

Following these successful validation results, the background-only fit results are extrapolated to the SRs, to derive the predicted background yield, which is then compared with the observed number of events[5]. The unblinded results in the SRs are presented in Figure 7.3. The dominant background in each one of the SRs and VRs is from $t\bar{t}$ events. In the 0-lepton signal regions, the main subdominant background contribution comes from $\text{Z}(\rightarrow \nu\nu)$+jets. In the 1-lepton signal regions, the main subdominant backgrounds are single-top and $t\bar{t}$+V. The observed and predicted background-only fit results in the cut-and-count SRs are summarized in Tables 7.1, 7.2, and 7.3.

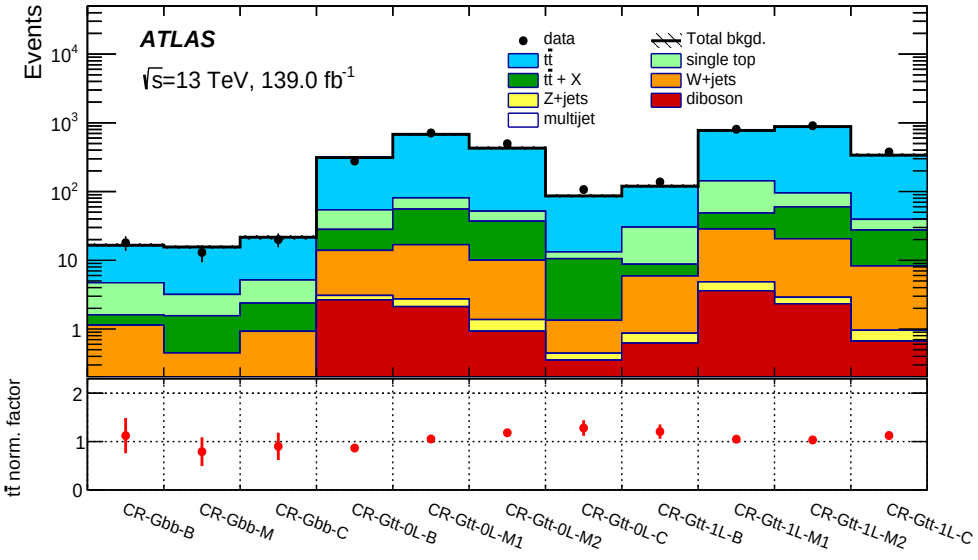

Figure 7.1: Background-only fit result in control regions.

[5] As part of ATLAS data analysis procedures, viewing the results of a fit to the data SRs is known as unblinding, for which permission is granted in an ATLAS approval meeting.

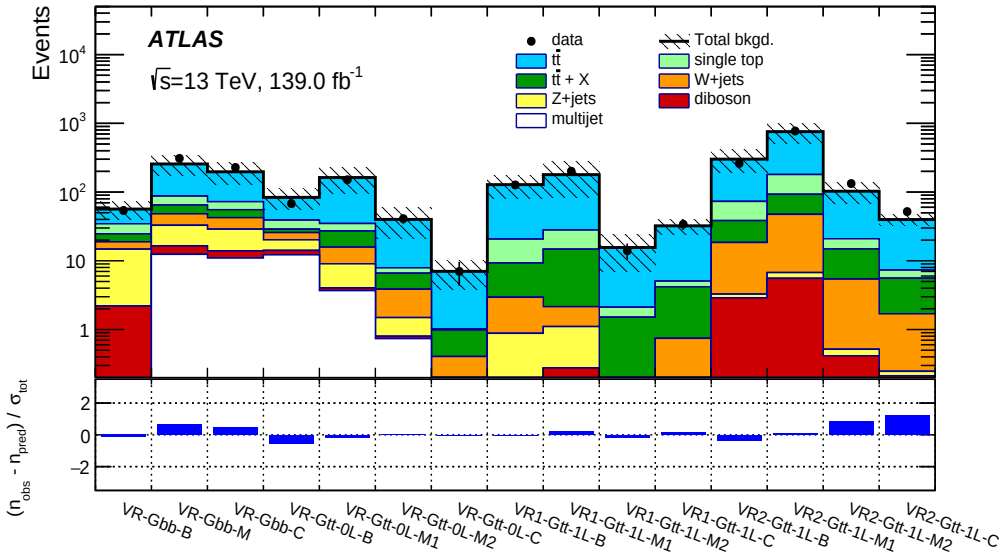

Figure 7.2: Background-only fit result in validation regions.

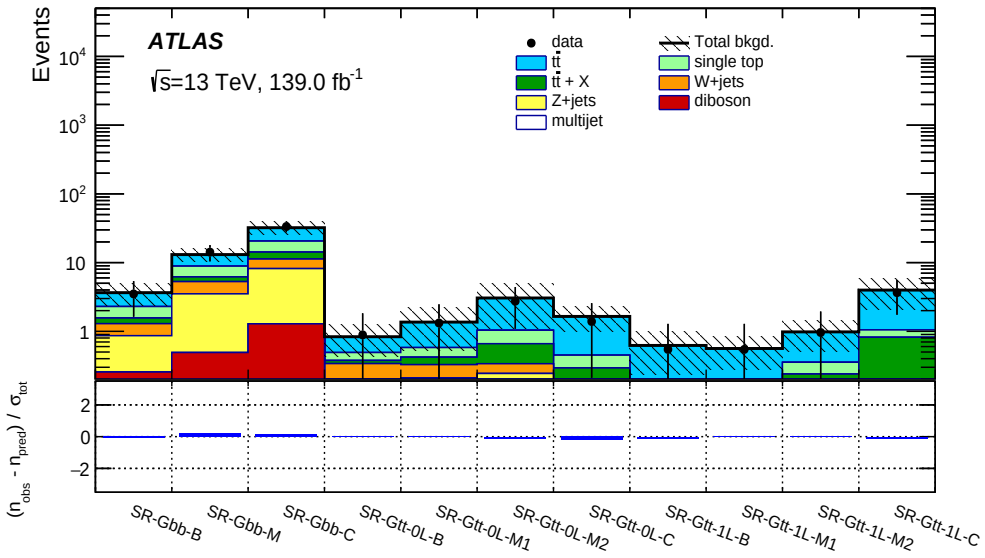

Figure 7.3: Background-only fit result in signal regions.

SR-Gbb			
Targeted kinematics	B	M	C
Observed events	3	14	33
Fitted background	3.65 ± 1.30	13.08 ± 2.75	32.19 ± 6.91
$t\bar{t}$	1.36 ± 0.87	4.20 ± 1.94	11.65 ± 4.67
Single-top	0.73 ± 0.71	2.69 ± 1.79	6.32 ± 4.73
$t\bar{t}$ + X	0.27 ± 0.15	0.90 ± 0.48	2.95 ± 1.52
Z+jets	0.61 ± 0.13	3.02 ± 0.31	6.89 ± 0.65
W+jets	0.43 ± 0.06	1.78 ± 0.25	3.09 ± 0.39
Diboson	0.26 ± 0.24	0.49 ± 0.31	1.29 ± 0.69
Multijet	< 0.01	< 0.01	< 0.01
MC-only background	3.50	14.72	33.46

Table 7.1: Results of the background-only fit extrapolated to the Gbb signal regions in the cut-and-count analysis, for the total background prediction and breakdown of the main backgrounds. The uncertainties shown include all systematic uncertainties. The $t\bar{t}$+X background includes $t\bar{t}W/Z$, $t\bar{t}H$ and $t\bar{t}t\bar{t}$ events. The row "MC-only background" provides pre-fit background prediction. According to Section 6.6, B=boosted, M=moderate, and C=compressed regions.

SR-Gtt-0L				
Targeted kinematics	B	M1	M2	C
Observed events	0	1	2	1
Fitted background	0.83 ± 0.41	1.36 ± 0.84	3.06 ± 1.96	1.65 ± 0.67
$t\bar{t}$	0.34 ± 0.33	0.78 ± 0.71	2.02 ± 1.90	1.20 ± 0.60
Single-top	0.11 ± 0.08	0.16 ± 0.12	0.38 ± 0.31	$0.16^{+0.17}_{-0.16}$
$t\bar{t}$ + X	0.04 ± 0.02	0.09 ± 0.04	0.32 ± 0.20	0.23 ± 0.16
Z+jets	0.17 ± 0.04	0.15 ± 0.07	0.24 ± 0.09	0.03 ± 0.02
W+jets	0.14 ± 0.06	0.12 ± 0.07	0.09 ± 0.06	0.03 ± 0.01
Diboson	< 0.01	< 0.01	< 0.01	< 0.01
Multijet	0.03 ± 0.03	0.06 ± 0.06	< 0.01	< 0.01
MC-only background	0.89	1.32	2.75	1.39

Table 7.2: Results of the background-only fit extrapolated to the Gtt 0-lepton signal regions in the cut-and-count analysis, for the total background prediction and breakdown of the main backgrounds. The uncertainties shown include all systematic uncertainties. The $t\bar{t}$+X background includes $t\bar{t}W/Z$, $t\bar{t}H$ and $t\bar{t}t\bar{t}$ events. The row "MC-only background" provides pre-fit background prediction. According to Section 6.6, B=boosted, M1=moderate1, M2=moderate2, and C=compressed regions.

SR-Gtt-1L				
Targeted kinematics	B	M1	M2	C
Observed events	0	0	1	3
Fitted background	0.62 ± 0.39	0.56 ± 0.29	0.98 ± 0.47	3.98 ± 1.87
$t\bar{t}$	0.46 ± 0.37	0.37 ± 0.26	0.63 ± 0.43	2.93 ± 1.68
Single-top	0.11 ± 0.07	0.08 ± 0.06	0.12 ± 0.08	0.23 ± 0.22
$t\bar{t}$ + X	0.05 ± 0.03	0.10 ± 0.06	0.23 ± 0.14	0.76 ± 0.45
Z+jets	< 0.01	< 0.01	< 0.01	0.01 ± 0.00
W+jets	0.01 ± 0.01	0.01 ± 0.01	0.01 ± 0.00	0.05 ± 0.02
Diboson	< 0.01	< 0.01	< 0.01	< 0.01
Multijet	< 0.01	< 0.01	< 0.01	< 0.01
MC-only background	0.55	0.55	0.96	3.66

Table 7.3: Results of the background-only fit extrapolated to the Gtt 1-lepton signal regions in the cut-and-count analysis, for the total background prediction and breakdown of the main backgrounds. The uncertainties shown include all systematic uncertainties. The $t\bar{t}$+X background includes $t\bar{t}W/Z$, $t\bar{t}H$ and $t\bar{t}t\bar{t}$ events. The row "MC-only background" provides pre-fit background prediction. According to Section 6.6, B=boosted, M=moderate, and C=compressed regions.

7.3 Model-dependent Fit (exclusion)

Since the data and the SM backgrounds in the signal regions are consistent (i.e., no significant excess is observed), the exclusion fit can be used to set limits at 95% confidence level (CL) on new physics theories. To place limits on signal models, the CL_s technique is utilized, by performing a statistical test on the background-only hypothesis likelihood function H_0 and signal plus background hypothesis likelihood function H_1. The first step in utilizing CL_s is to define a test statistic t which can be used to distinguish between the alternate hypothesis (H_1) and the null hypothesis (H_0).

To illustrate how this works: in Figure 7.4a, the H_0 and H_1 distributions are shown in blue and red histograms respectively. In this example, both distributions are generated using a Poisson PDF with mean expectation values $\lambda_b = 3$ and $\lambda_{s+b} = 10$ for H_0 and H_1 respectively. The p_b is the probability to find N greater than or equal to N_{obs} under the assumption of the background-only hypothesis (shown as shaded blue). A low value for p_b means that the observed result is less compatible with the H_0 hypothesis, and can be interpreted as a rejection of H_0 in favour of the H_1. The p-value [163] for the H_1 hypothesis (p_{s+b}) is the probability that one would measure N to be equal or less than N_{obs} under the assumption of this hypothesis (shown as shaded red). These are formulated in Eq. 7.6:

$$\begin{aligned} p_b &= \int_{N_{\text{obs}}}^{\infty} f(N|s=0,b)\ dN \\ p_{s+b} &= \int_{-\infty}^{N_{\text{obs}}} f(N|s+b)\ dN \quad , \end{aligned} \tag{7.6}$$

where $N_{\text{obs}} = 7$, and consequently $p_b = 3.2\%$ and $p_{s+b} = 22.8\%$. In this case, the observed result is more similar to H_1 than H_0. The ATLAS convention [164,165] is to exclude a signal model at a 95% CL if $p_{s+b} < 0.05$. Similarly one can define a confidence interval by finding the upper limit s_{up}, which is the largest signal rate not excluded. In Figure 7.4b, the background-only model (blue) as well as three different signal+background models are shown. The upper limit is $s = 9$ since $p_{s+b} = \int_{-\infty}^{N_{\text{obs}}=4} f(N|s=9,b) = 0.05$, so all signal models with $s > 9$ are excluded at 95% CL. The problem with p_{s+b} is that if the expected number of signal events λ_s is much less than the number of background events λ_b (in other words, if $H_1 \approx H_0$), and the observed data has a downward fluctuation

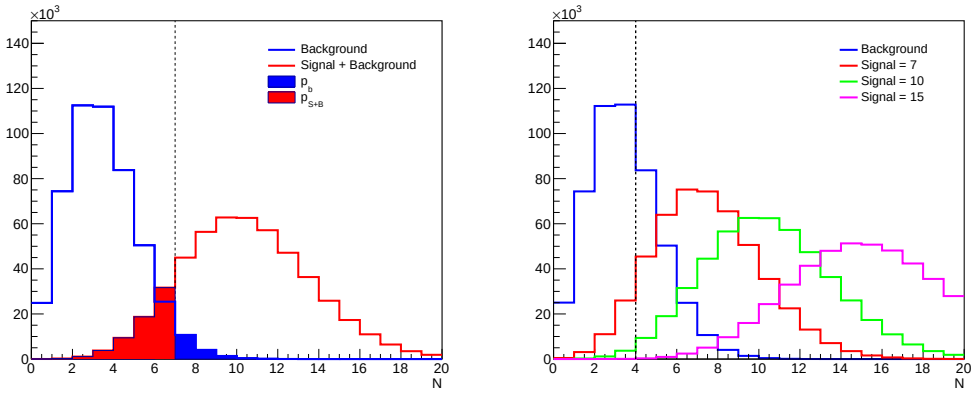

(a) (b)

Figure 7.4: (a) Poisson distributions and p-values for background-only and signal+background hypotheses with $N_{\text{obs}} = 7$. (b) Poisson distributions for background-only and three signal+background hypotheses with $N_{\text{obs}} = 4$.

with respect to the background expectation, one can exclude a signal model to which there is little or no sensitivity (i.e., for which $\lambda_s \approx 0$).

To regulate this issue in ATLAS, the CL_s procedure is used to combine p_{s+b} and p_b as shown in Eq. 7.7:

$$\text{CL}_s = \frac{p_{s+b}}{1 - p_b} = \frac{\text{CL}_{s+b}}{\text{CL}_b} \quad , \tag{7.7}$$

where CL_{s+b} and CL_b are confidence levels for H_1 and H_0. If the two hypotheses have similar likelihoods, and thus there is little sensitivity to the signal model, $1-p_b$ becomes small, and this counteracts small values of p_{s+b}. To set exclusion limits on signal models, the CL_s value is compared to $\alpha = 0.05$, which is the conventional limit set by the ATLAS collaboration. Signal models with $\text{CL}_s < 0.05$ are excluded at 95% CL.

From the Neyman-Pearson lemma [166], the most statistically powerful test statistic is the profile likelihood ratio, defined as:

$$q(\mu_{\text{sig}}) = -2\ln\left(\frac{L(\mu_{\text{sig}}, \hat{\hat{\theta}})}{L(\hat{\mu}_{\text{sig}}, \hat{\theta})}\right) \quad , \tag{7.8}$$

where $\hat{\mu}_{\text{sig}}$ and $\hat{\theta}$ are the maximum likelihood estimators for μ_{sig} and θ, and $\hat{\hat{\theta}}$ is the conditional maximum likelihood estimator for the specific value of μ_{sig}. Signal-like data corresponds to small values of $q(\mu_{\text{sig}})$ (numerator $\approx$ denominator in Eq. 7.8) and, similarly, large values of $q(\mu_{\text{sig}})$ represent background-like

data (denominator $\gg$ numerator). To be able to compute the p-values in Eq. 7.6, one needs to obtain the PDF of the test statistic, for example $f(q|\mu_{\text{sig}})$ and $f(q|\mu_{\text{sig}} = 0)$, given alternate H_1 and null H_0 hypotheses. The PDF of the test statistic can be determined by using toy MC simulation (i.e., pseudo-experiments) where the values of nuisance parameters are randomly generated by sampling their constraint terms. Then, the new expected yields are computed using these generated nuisance parameters, while the observed values are generated from the Poisson fluctuation of the expected yields. In the limit of a large number of events, the PDF of the test statistic can be derived analytically by using an asymptotic approximation. In this technique, the test statistic is distributed according to a non-central chi-square PDF with one degree of freedom. More details about this method can be found in Ref. [167] .

The exclusion fit is performed in the CRs and SRs (see Eq. 7.1), where the signal sample is included in order to correctly account for signal contamination in the CRs. For each signal model, as defined using both the mass of the gluino ($m_{\tilde{g}}$) and the mass of the neutralino ($m_{\tilde{\chi}_1^0}$), the CL$_s$ value is calculated, and if the CL$_s < 0.05$, that signal point is excluded at the 95% CL. The 95% CL expected and observed exclusion limits for the Gbb and Gtt models in the gluino and neutralino mass plane are shown in Figure 7.5. Assuming a massless neutralino, the observed exclusion limit for the gluino is at approximately 2.31 TeV and 2.29 TeV for the Gbb and Gtt models. The comparison between the exclusion limits reported by the ATLAS and CMS collaborations is discussed in Appendix D.

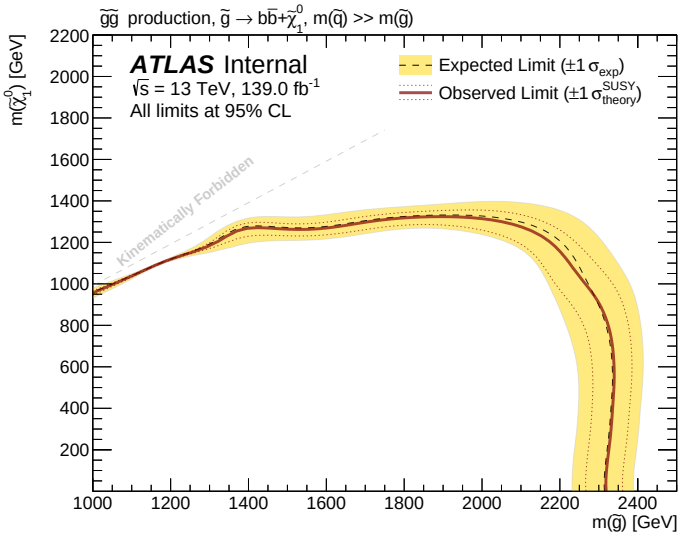

(a)

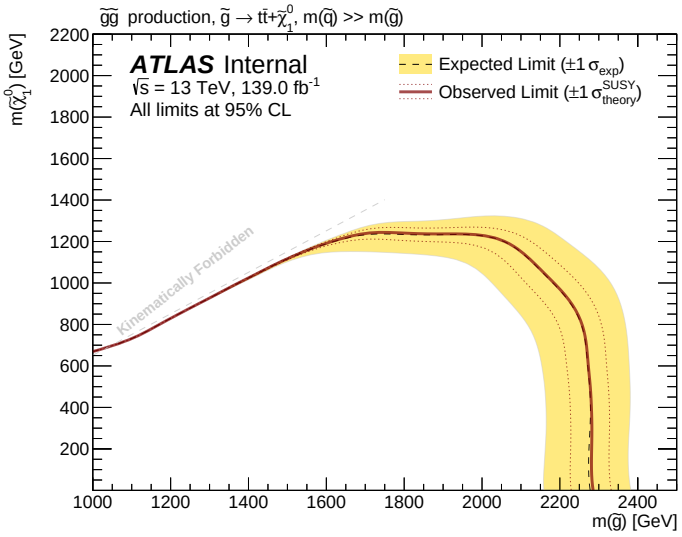

(b)

Figure 7.5: Exclusion limits for the (a) Gbb and (b) Gtt models in the $m_{\tilde{g}}$ and $m_{\tilde{\chi}_1^0}$ mass plane. The 95% expected and observed CL are shown with dashed and solid bold lines. The bands around the expected limit present the impact of experimental and theoretical uncertainties. The signal cross-section variation by $\pm 1\sigma$ of its theoretical uncertainty is shown with dotted lines around the observed limit. Individual exclusion limits for Gbb, Gtt-0L and Gtt-1L are presented in Appendix C.

Chapter 8

Conclusion

This dissertation has presented a search for the pair production of gluinos where each gluino decays via off-shell stop or sbottom to four top or bottom quarks and the LSP, using 139 fb^{-1} data of proton-proton collision collected by the ATLAS detector during 2015-2018 at a center-of-mass energy $\sqrt{s}$ = 13 TeV. These results that were presented in Chapter 7 supersede the previous ATLAS searches, which respectively had been performed using 36 fb^{-1} [131] and 79 fb^{-1} [132] subsets of our present 139 fb^{-1} dataset.

This search was performed by using events which include at least four jets (including at least three b-jets), and large missing transverse momentum ($E_{\mathrm{T}}^{\mathrm{miss}}$) in the final state. The cut-and-count strategy is applied with several signal regions optimized to maximize the significance for individual Gtt and Gbb signal models (see Section 6.6). The control and validation regions are defined for each signal region to derive and validate the $t\bar{t}$+jets normalisation factor. In all signal regions, no significant excess is observed in data above the SM backgrounds. The exclusion limits are then set at 95% confidence level in the $m_{\tilde{g}}$ and $m_{\tilde{\chi}_1^0}$ mass plane for two simplified signal models. The increase in integrated luminosity leads to a 100 GeV and 40 GeV higher exclusion limit (when compared with previous results) in the gluino mass, when assuming a massless LSP, in the Gbb and Gtt models. Gluinos with masses below 2.3 TeV are excluded at 95% confidence level, assuming massless neutralinos in the Gtt and Gbb models.

There are some possibilities for enhancing the sensitivity of this analysis: increasing integrated luminosity, or implementing more sophisticated approaches such as multi-bin or multivariate techniques. Over the past year, major work has been carried out on CERN's entire accelerator and experimental complex,

to be prepared for the next LHC run, and also for high-luminosity operation after 2027. The LHC will restart in 2022 for three years of data taking at $\sqrt{s} = 14$ TeV, providing 300 fb^{-1} integrated luminosity, and will then undergo a 2-year shutdown starting in 2025. This will be a fascinating opportunity for physicists to study SM and beyond-SM mechanisms in more detail, and to hopefully observe rare new particles.

Appendices

Appendix A

Kinematic Reweighting in 1-lepton region

In this appendix, the reweighting strategy designed to fix the effect of mis-modelling in 1-lepton kinematic variables is discussed. Given that the same trend in the data to MC ratio in the $m_{\text{eff}}^{\text{incl}}$ distribution has been observed in $t\bar{t}$, single-top, W+jets, and Z+jets, reweighting factors are derived in a set of orthogonal control regions enriched in these backgrounds. The definition of the control regions is summarized in Table A.1. These regions are orthogonal to the analysis CRs and SRs, via an $N^{\text{b-jet}}$ cut. Firstly, data-MC ratio in the $m_{\text{eff}}^{\text{incl}}$ distribution is fitted using an exponential function, which then provides the actual reweighting functions. The fit is performed in 12 bins of $m_{\text{eff}}^{\text{incl}}$ and in different N_{jet} slices ($= 4$, $= 5$, $= 6$, ≥ 7). As an example, the fit results for $t\bar{t}$ and W+jets (as the dominant backgrounds) are shown in Figures A.1 and A.2.

Criteria common to all regions: $N_{\text{jet}} \geq 4$, $E_{\text{T}}^{\text{miss}} \geq 200$ GeV				
Control-region	N_{lepton}	$N^{\text{b-jet}}$	$m_{\text{T,min}}^{\text{b-jets}}$ (GeV)	M_{Z} (GeV)
$t\bar{t}$-enriched	$= 1$	$= 2$	≤ 350	
single-top-enriched	$= 1$	$= 2$	> 350	
W-enriched	$= 1$	$= 0$		
Z-enriched	$= 2$ (O/S)	$= 0$		$\in$ (60,120)

Table A.1: Definitions of the control regions used to derive the kinematic re-weighting scale-factors. The $N^{\text{b-jet}}$ requirements ensure these control regions are orthogonal to all signal regions of the analysis, and include a $N^{\text{b-jet}} \geq 3$ requirement. The Z-enriched region uses a mass window cut close to the Z boson mass.

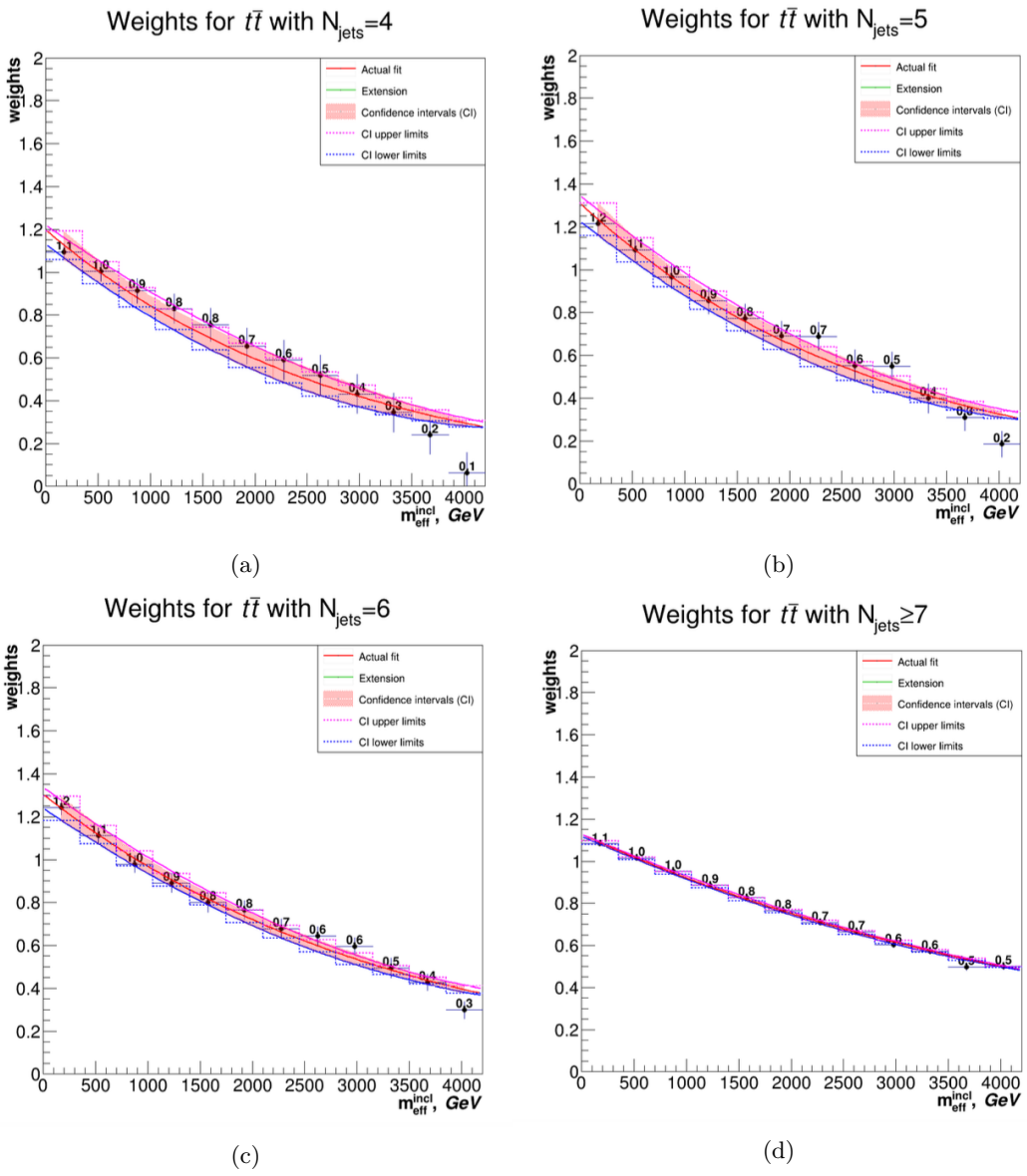

(a) (b)

(c) (d)

Figure A.1: Result of the reweighting for the $t\bar{t}$-enriched region in different N_{jet} slices.

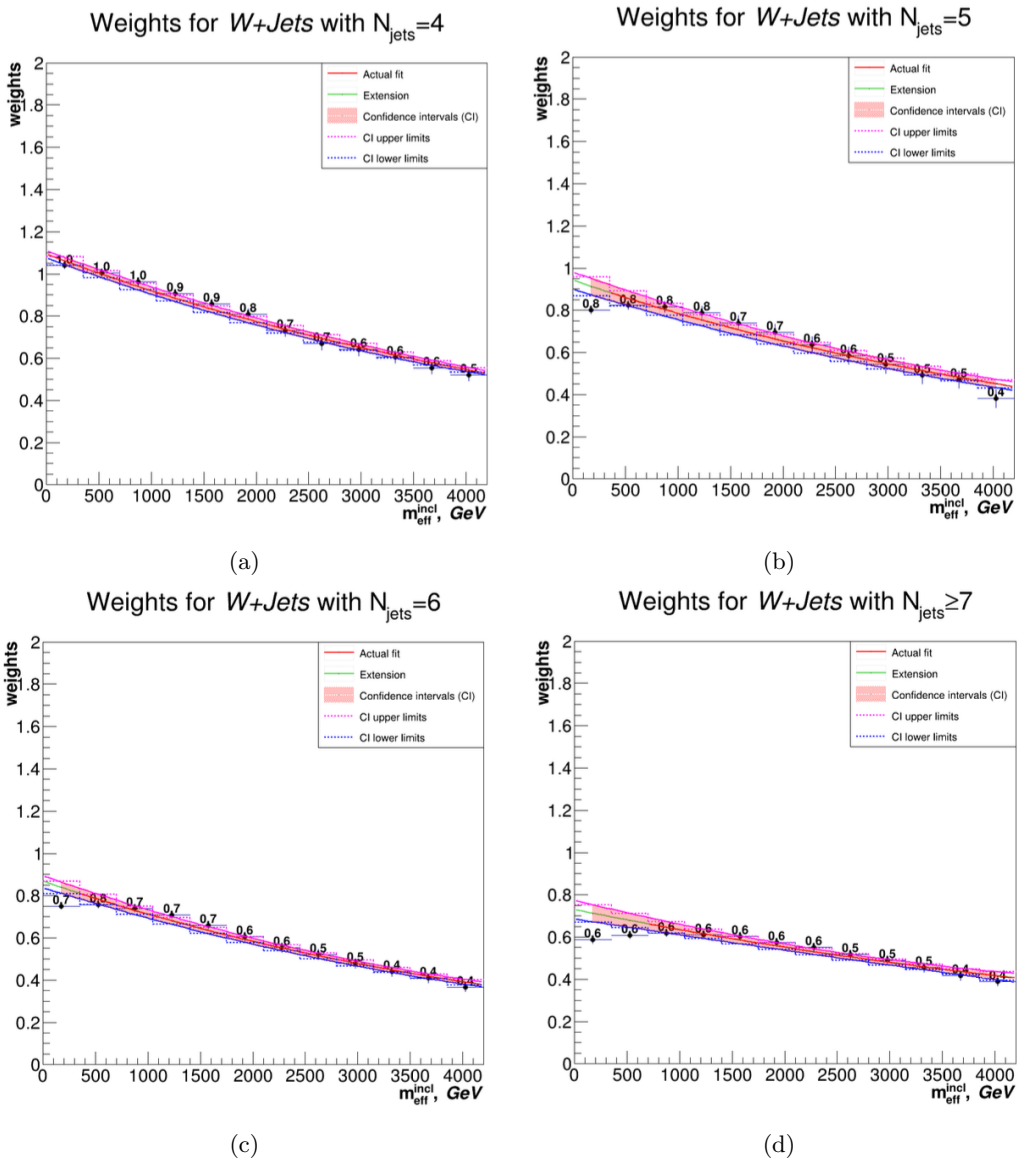

(a) (b)

(c) (d)

Figure A.2: Result of the reweighting for the W-enriched region in different N_{jet} slices.

Appendix B

Region Optimization

The optimization framework github:kratsg/optimization used in this analysis is a Python package to perform a signal grid scan over selected variables to optimize for the greatest significance within a given region of phase space. The optimization process includes two steps: first a supercut (produced as a JSON file) containing the starting point, ending point, and step size of different variables is constructed. Then, the optimization script takes the signal files, background files, and supercut to scan over the signal grid in order to derive the output optimal selections. The Gtt-0L results of scans for $m_{\text{eff}}^{\text{incl}}$, N_{jet}, and $E_{\text{T}}^{\text{miss}}$ are shown in Figure B.1. Variation in optimal cuts across the gluino-neutralino masses has an impact on our choice in the definition of the SRs. The same strategy has been used to optimize Gtt-1L and Gbb regions (Figures B.2 and B.3). An example of a supercut used to optimize Gtt-0L is summarized in Table B.1.

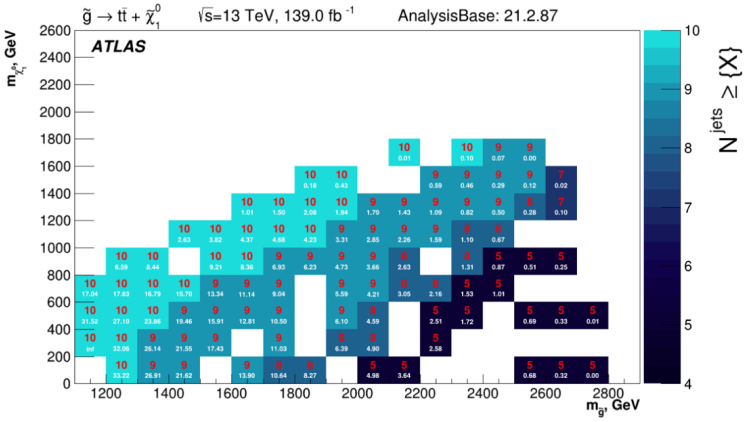

(a)

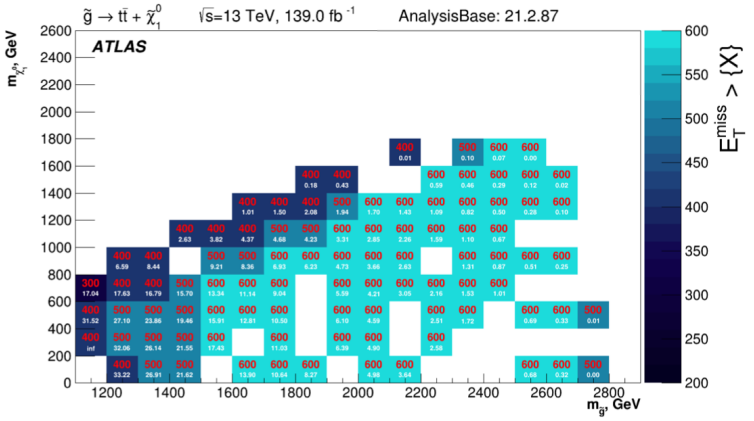

(b)

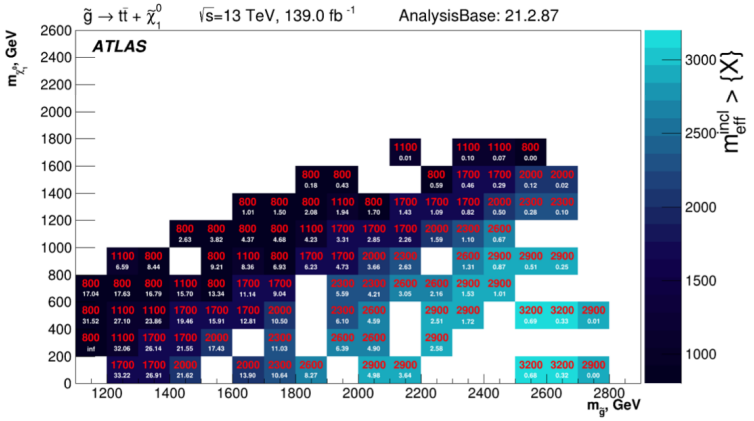

(c)

Figure B.1: The optimal selection values (in red) and expected significance (in white) in the Gtt-0L channel for (a) N_{jet}, (b) $E_{\text{T}}^{\text{miss}}$, and (c) $m_{\text{eff}}^{\text{incl}}$. Each grid point represents a mass point in the gluino-neutralino plane, with the gluino mass on the x-axis and neutralino mass on the y-axis.

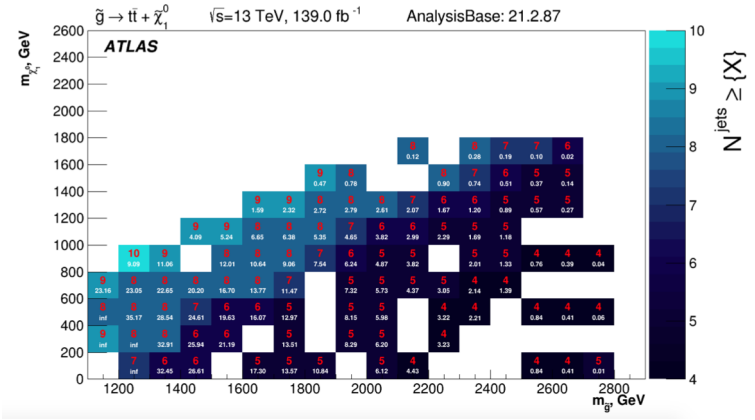

(a)

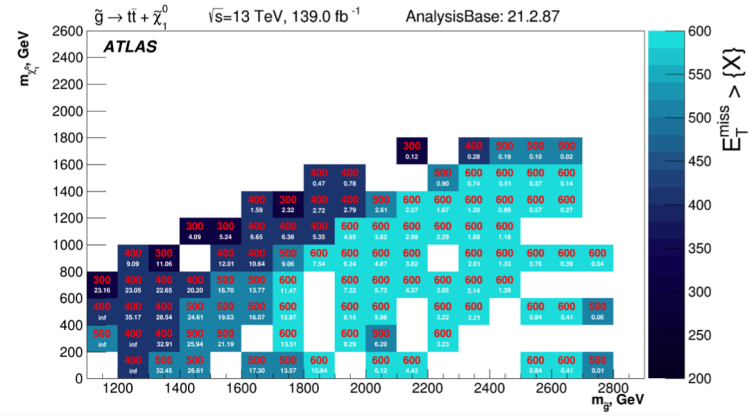

(b)

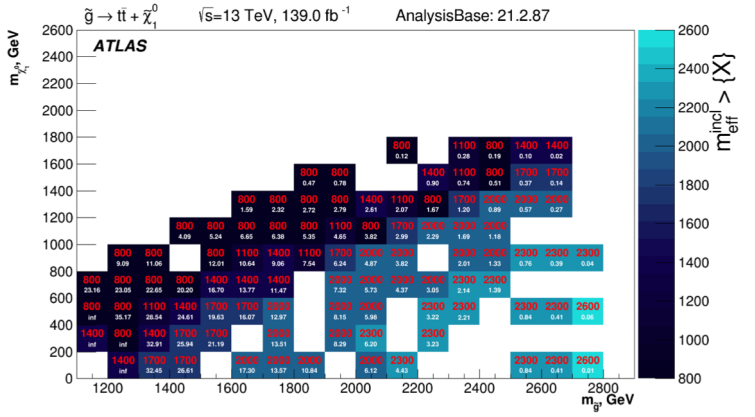

(c)

Figure B.2: The optimal selection values (in red) and expected significance (in white) in the Gtt-1L channel for (a) N_{jet}, (b) $E_{\text{T}}^{\text{miss}}$, and (c) $m_{\text{eff}}^{\text{incl}}$. Each grid point represents a mass point in the gluino-neutralino plane, with the gluino mass on the x-axis and neutralino mass on the y-axis.

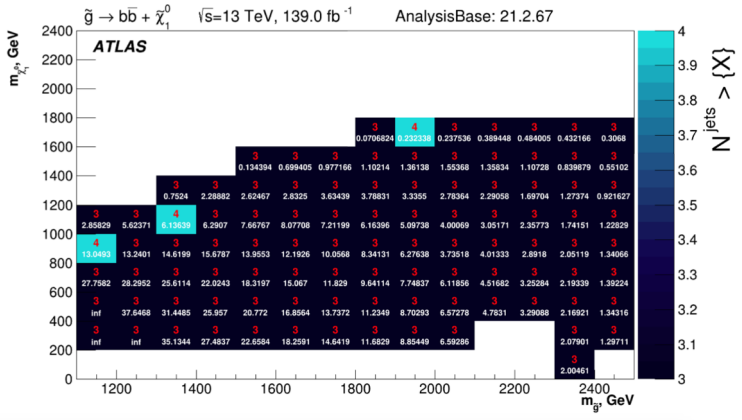

(a)

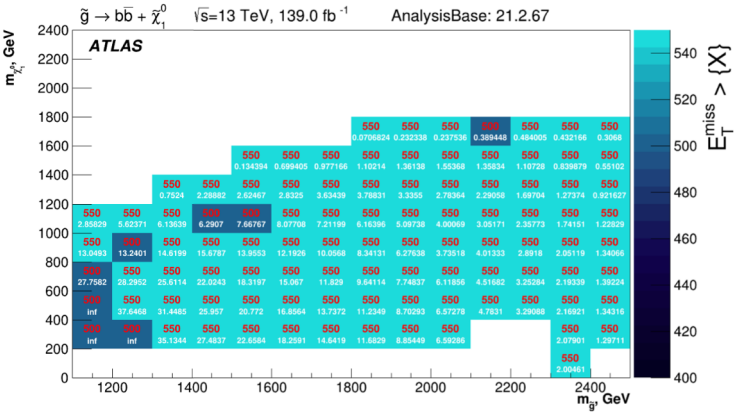

(b)

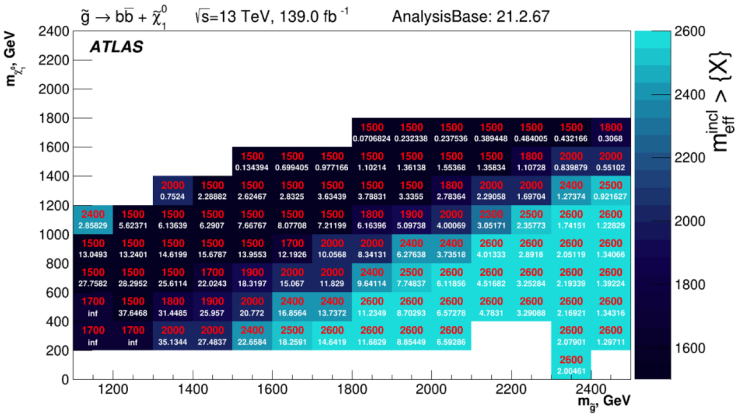

(c)

Figure B.3: The optimal selection values (in red) and expected significance (in white) in the Gbb channel for (a) N_{jet}, (b) $E_{\text{T}}^{\text{miss}}$, and (c) $m_{\text{eff}}^{\text{incl}}$. Each grid point represents a mass point in gluino-neutralino plane, with the gluino mass on the x-axis and neutralino mass on the y-axis.

Gtt 0-lepton								
Parameters:	N_{jet}	$N^{b-\text{jet}}$	$p_{\text{T}^{\text{jet}}}$	$E_{\text{T}}^{\text{miss}}$	$\Delta\phi_{\text{min}}$	$m_{\text{eff}}^{\text{incl}}$	$m_{\text{T,min}}^{\text{b-jets}}$	M_J^{Σ}
Min value:	4	3	30	200	0.4	800	0	0
Max value:	10	4	X	600	X	3200	120	400
Step:	1	1	X	100	X	300	40	100

Table B.1: Ranges of selections in variables used in Gtt 0L SR optimization. All kinematic variables are expressed in Gev except $\Delta\phi_{\text{min}}$ which is in radians.

Appendix C

Additional Analysis Material

C.1 Preselection plots

This appendix includes the data and MC simulation (background + signal) comparison for the analysis variables in the preselection region. The statistical and all experimental systematic uncertainties are applied in the plots.

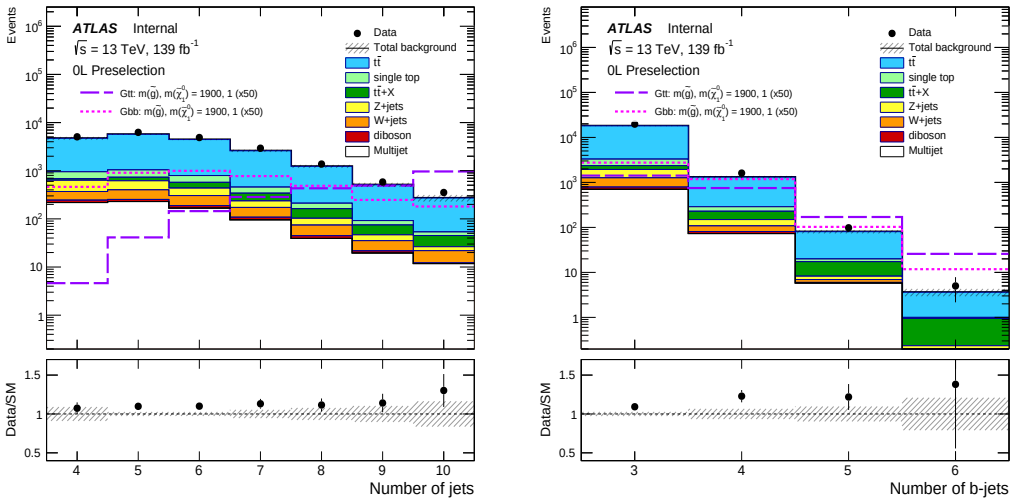

(a) (b)

Figure C.1: Distributions of (a) the number of selected jets and (b) the number of selected b-jets for events passing the 0-lepton preselection criteria. The statistical and experimental systematic uncertainties (as described in Section 6.7) are included in the uncertainty band. The last bin includes overflow events. The lower part of each figure shows the ratio of data to the background prediction. Example signal models with cross-sections enhanced by a factor of 50 are overlaid for comparison.

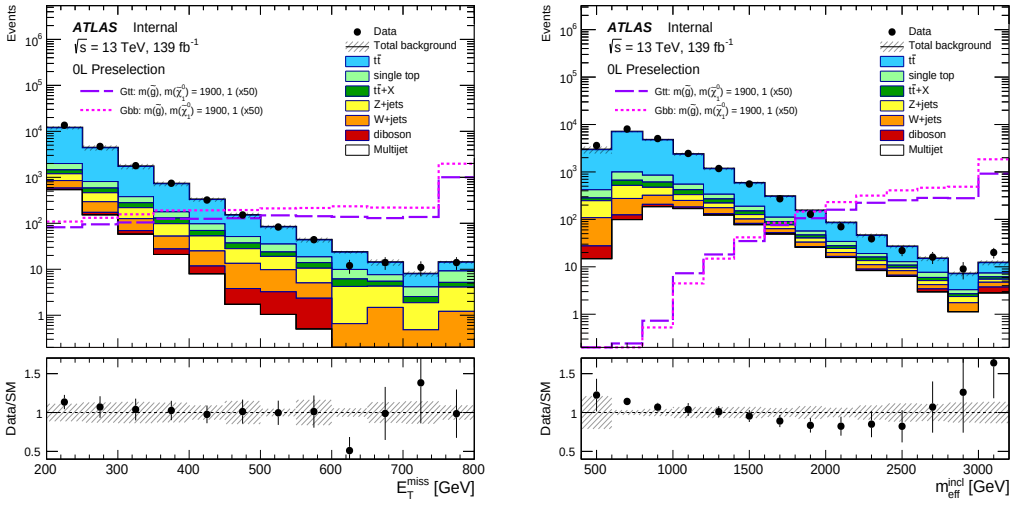

(a) (b)

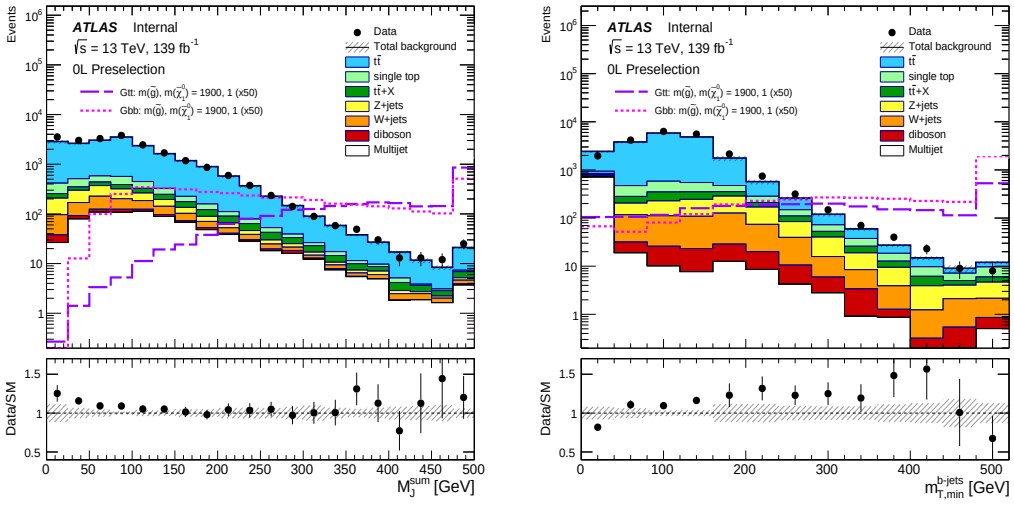

(c) (d)

Figure C.2: Distributions of (a) $E_{\mathrm{T}}^{\mathrm{miss}}$, (b) $m_{\mathrm{eff}}^{\mathrm{incl}}$, (c) M_J^{Σ}, and (d) $m_{\mathrm{T,min}}^{\text{b-jets}}$ for events passing the 0-lepton preselection criteria. The statistical and experimental systematic uncertainties (as described in Section 6.7) are included in the uncertainty band. The last bin includes overflow events. The lower part of each figure shows the ratio of data to the background prediction. Example signal models with cross-sections enhanced by a factor of 50 are overlaid for comparison.

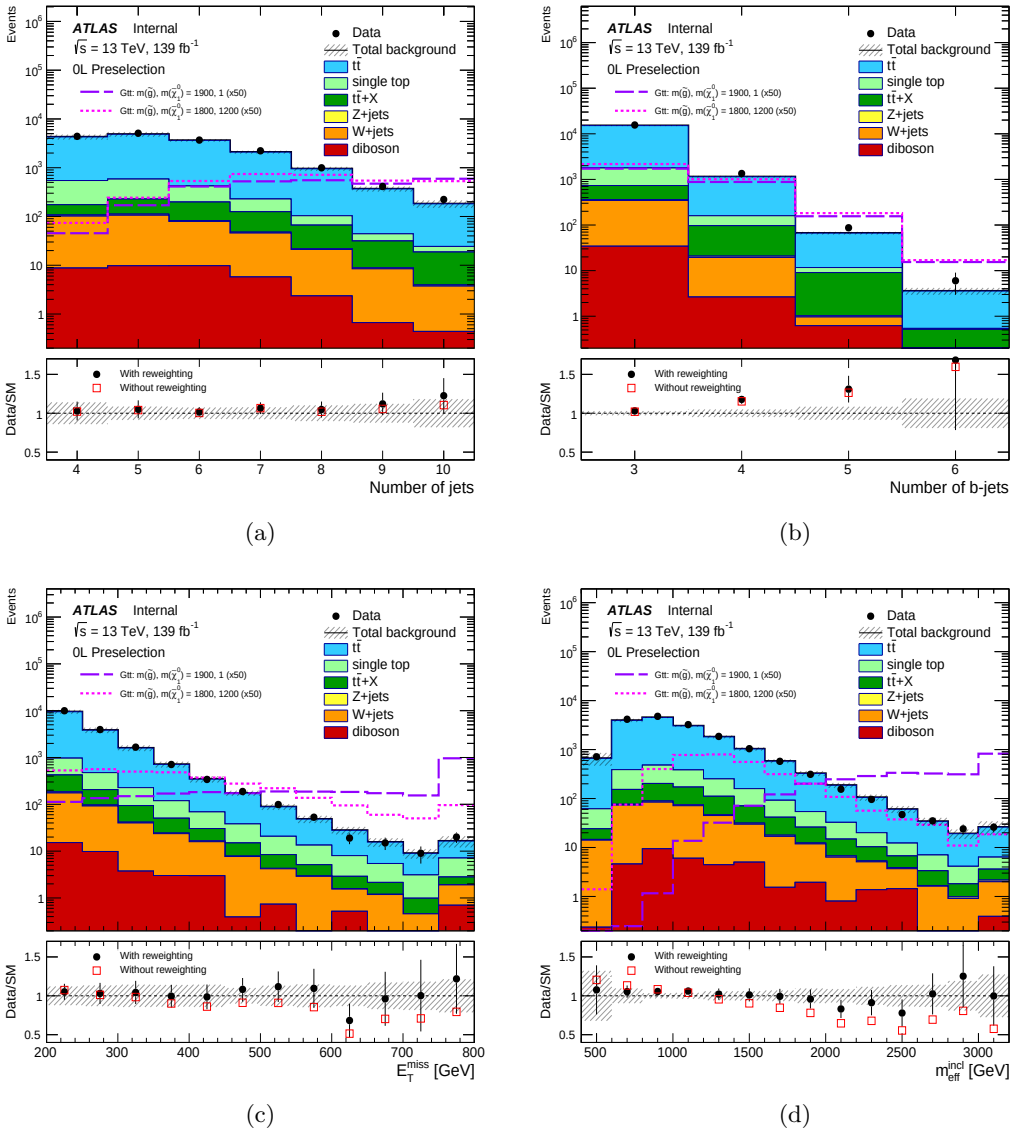

(a) (b)

(c) (d)

Figure C.3: Distributions of (a) the number of selected jets, (b) the number selected b-jets, (c) $E_{\mathrm{T}}^{\mathrm{miss}}$, and (d) $m_{\mathrm{eff}}^{\mathrm{incl}}$ for events passing the 1-lepton preselection criteria. The statistical and experimental systematic uncertainties (as described in Section 6.7) are included in the uncertainty band. The last bin includes overflow events. The lower part of each figure shows the ratio of data to the background prediction. Example signal models with cross-sections enhanced by a factor of 50 are overlaid for comparison.

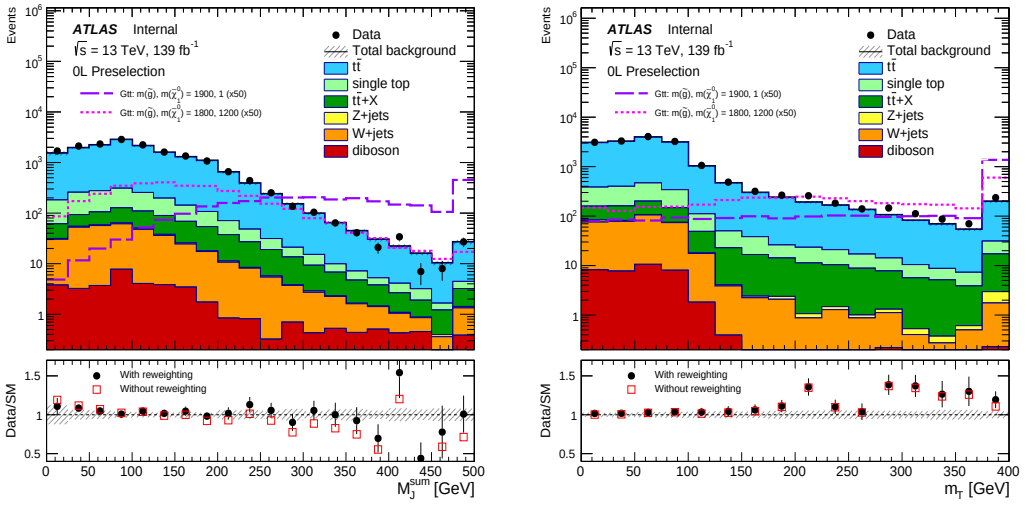

(a) (b)

Figure C.4: Distributions of (a) M_J^{Σ} and (b) m_{T} for events passing the 1-lepton preselection criteria. The statistical and experimental systematic uncertainties (as described in Section 6.7) are included in the uncertainty band. The last bin includes overflow events. The lower part of each figure shows the ratio of data to the background prediction. Example signal models with cross-sections enhanced by a factor of 50 are overlaid for comparison.

C.2 Gbb Signal Region Results

This section includes the post-fit data and MC simulation (background + signal) comparison for the number of jets in the Gbb signal regions (Figure C.5). The statistical and all experimental systematic uncertainties are shown in the plots.

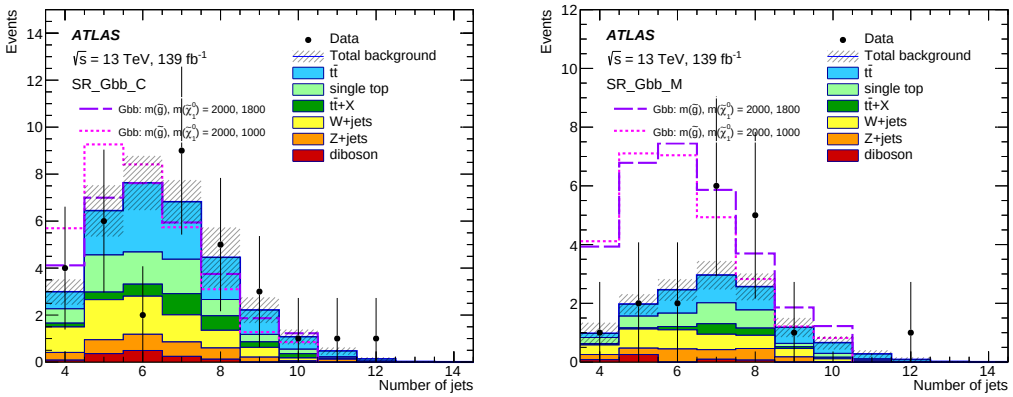

(a)

(b)

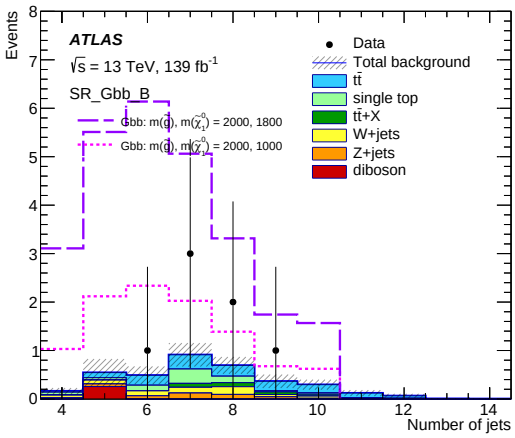

(c)

Figure C.5: Distributions of the number of jets in SR_Gbb_C (a), SR_Gbb_M (b), and SR_Gbb_B (c), post-fit, for events passing the corresponding SR selections. The statistical and experimental systematic uncertainties (as described in Section 6.7) are included in the uncertainty band. Example signal models in the compressed and moderate regions are overlaid for comparison.

C.3 Individual Exclusion Limits

This section presents the individual exclusion limits for the Gbb, Gtt-0L, and Gtt-1L channels in cut-and-count boosted, moderate, and compressed regions as described in subsection 6.6.1. All exclusion limits are shown in Figures C.6, C.7, and C.8.

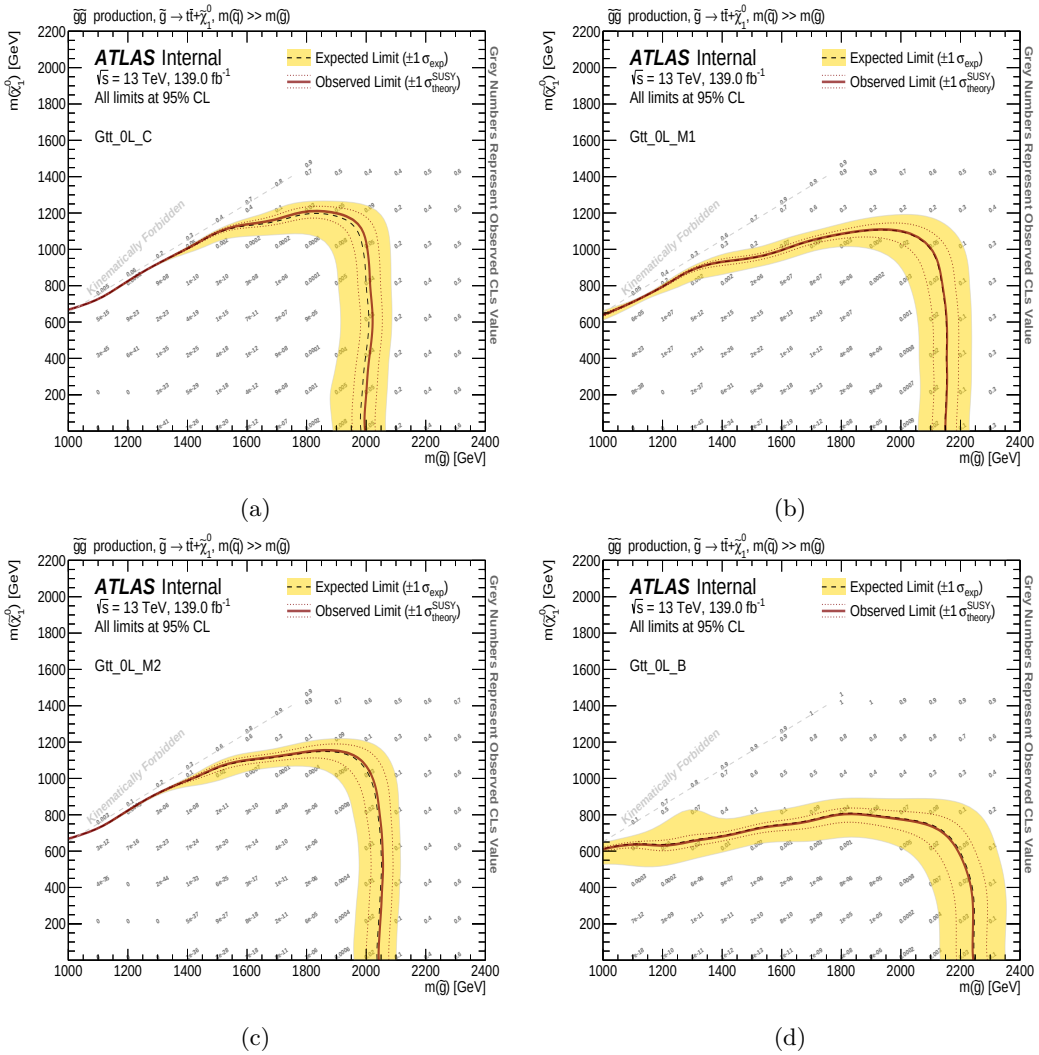

Figure C.6: Exclusion limits for (a) Gtt-0L-C, (b) Gtt-0L-M1, (c) Gtt-0L-M2, and (d) Gtt-0L-B signal regions in the $m_{\tilde{g}}$ and $m_{\tilde{\chi}_1^0}$ mass plane. The 95% expected and observed CL are shown with dashed and solid bold lines. The bands around the expected limit presents the impact of experimental and theoretical uncertainties. The signal cross-section variation by $\pm 1\sigma$ of its theoretical uncertainty is shown with dotted lines around the observed limit. Grey numbers represent observed CL_s values.

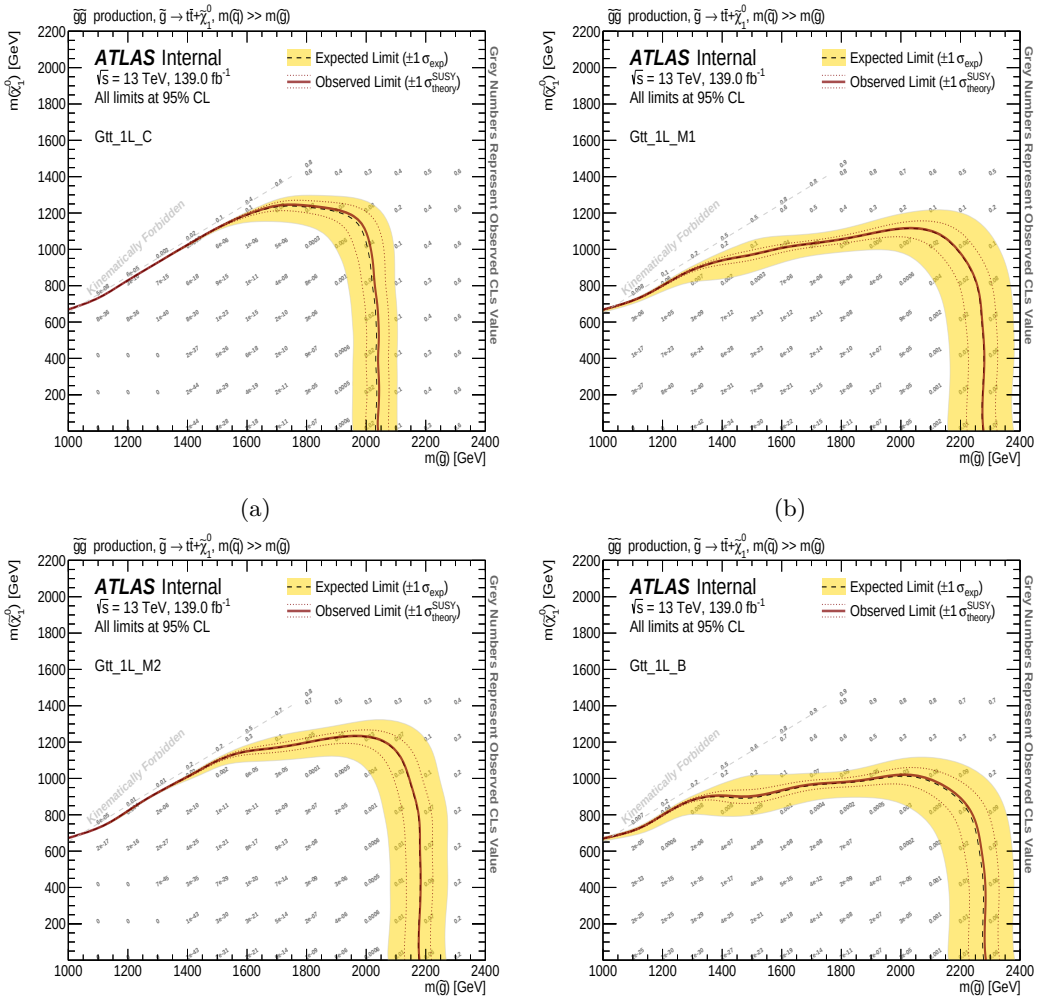

Figure C.7: Exclusion limits for (a) Gtt-1L-C, (b) Gtt-1L-M1, (c) Gtt-1L-M2, and (d) Gtt-1L-B signal regions in the $m_{\tilde{g}}$ and $m_{\tilde{\chi}_1^0}$ mass plane. The 95% expected and observed CL are shown with dashed and solid bold lines. The bands around the expected limit presents the impact of experimental and theoretical uncertainties. The signal cross-section variation by $\pm 1\sigma$ of its theoretical uncertainty is shown with dotted lines around the observed limit. Grey numbers represent observed CL_s values.

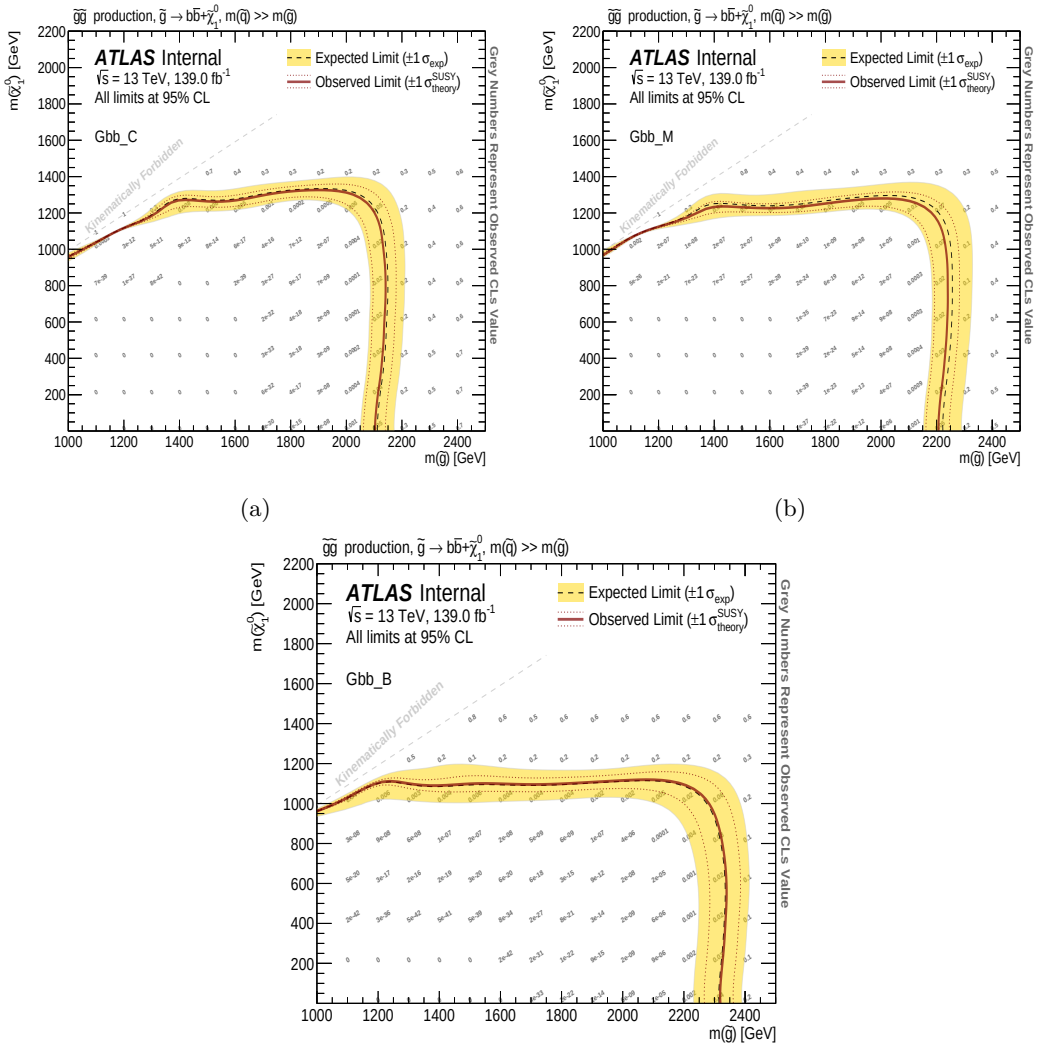

(a) (b)

(c)

Figure C.8: Exclusion limits for (a) Gbb-C, (b) Gbb-M, and (c) Gbb-B signal regions in the $m_{\tilde{g}}$ and $m_{\tilde{\chi}_1^0}$ mass plane. The 95% expected and observed CL are shown with dashed and solid bold lines. The bands around the expected limit presents the impact of experimental and theoretical uncertainties. The signal cross-section variation by $\pm 1\sigma$ of its theoretical uncertainty is shown with dotted lines around the observed limit. Grey numbers represent observed CL_s values.

Appendix D

ATLAS and CMS Exclusion Limits

A summary of all all previous Gtt and Gbb exclusion limits reported by the ATLAS and CMS collaborations is presented in Figure D.1. The exclusion limits described in this analysis have not been included yet in the ATLAS summary plot. Both the ATLAS and CMS experiments provide similar sensitivity in terms of observed Gbb exclusion limits. The Gtt exclusion limit in the ATLAS multi-b analysis (see Figure 7.5) has an approximately 50 GeV higher sensitivity in the boosted region, when compared with the observed limit by the CMS M_{T2} group (as the best observed limit in CMS). This is due to both the 2 fb^{-1} larger integrated luminosity sample recorded by ATLAS, as well as the combination of 0L+1L Gtt exclusion limits which extends the sensitivity in the boosted region.

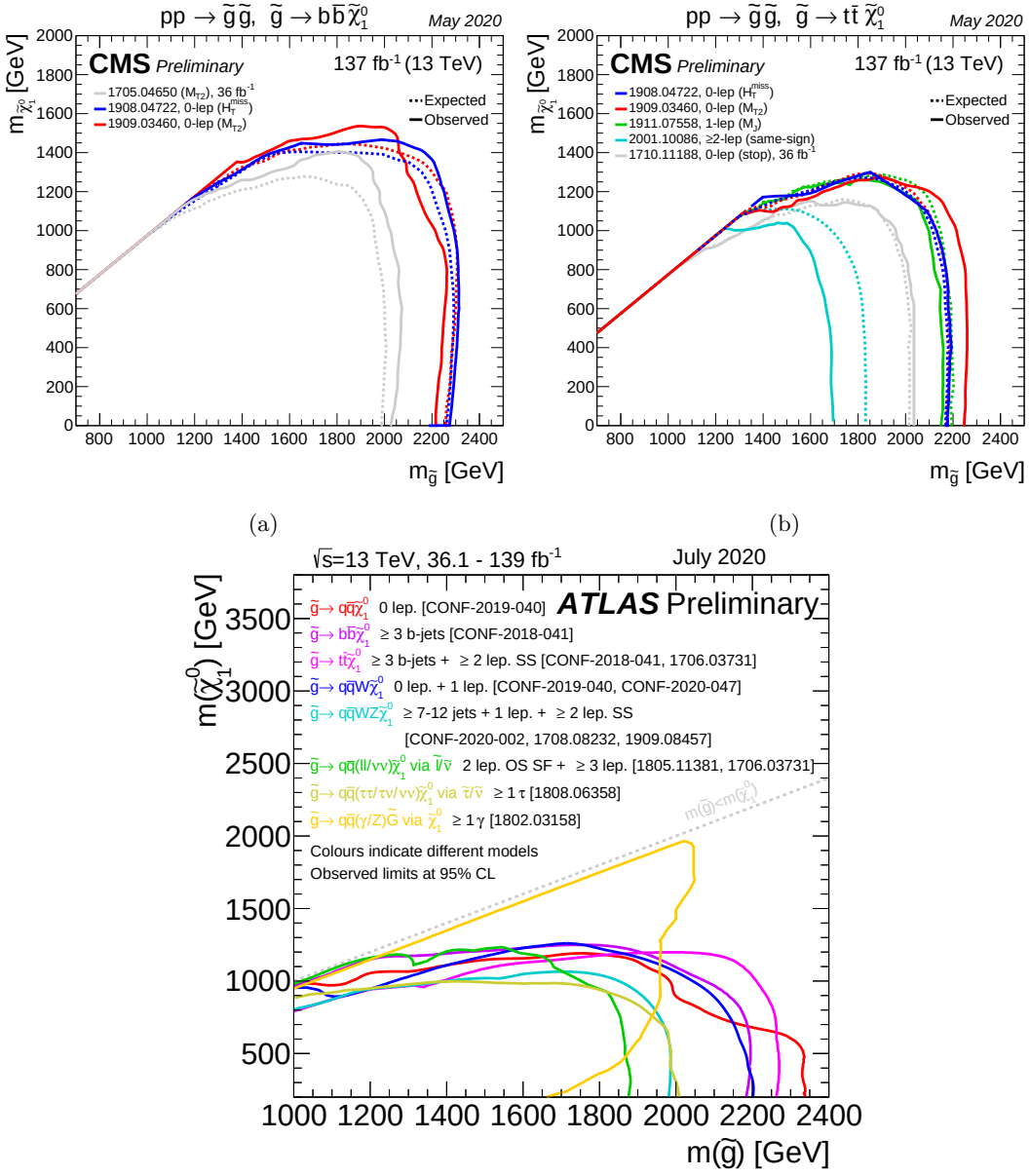

Figure D.1: Mass limits at 95% CL in CMS for simplified models of gluino pair production with gluino decays to (a) pairs of bottom quarks and the LSP and (b) pairs of top quarks and the LSP [168]. (c) Exclusion limits at 95% CL based on 13 TeV data in the (gluino, lightest neutralino) mass plane for different simplified models featuring the decay of the gluino to the lightest supersymmetric particle in ATLAS [169].

Appendix E

LAr Data Quality Monitoring

The ATLAS liquid argon calorimeter (LAr calo) is designed to measure properties of electrons, photons, jets, and missing transverse momentum in a wide pseudorapidity region. To use the best quality LAr calo data, with the lowest possible level of data rejection in physics analyses, an advanced data quality monitoring system is designed.

The ATLAS data is classified into streams such as calibration or physics streams. The calibration streams are used to monitor and calibrate run conditions via instantaneous luminosity and noisy channels, and the physics streams include all information that is directly necessary for physics analysis (and which depends on the trigger menu used to collect physics streams). An overview of the ATLAS data processing system is shown in Figure E.1. At the start of each run, the calibration streams are analysed during what is known as express processing. At this stage, data quality checks are performed, and information on calibration constants and on noisy cells is updated in the database. The express processing is done within 48 hours after the run is finished (which is shown as *calibration loop* in Figure E.1). Typically, after 48 hours, the full dataset (known as the *bulk*) is available, and the final data quality checks are performed on each of the physics streams in order to obtain any remaining noisy cells.

To identify noisy channels, the calibration runs are performed daily or weekly between LHC fills (using events that are triggered during the passage of groups of empty bunches within each LHC fill). Two offline flagging schemes are applied to identify noisy channels:

- **Unconditionally masked (High Noise High Gain)** not operational cells due to large noise or dead readout channel are unconditionally masked

and their energy is evaluated by using the average energy of the neighbouring cells [170].

- **Conditionally masked (Sporadic Burst Noise)** operational cells which are affected by large noise can be conditionally masked. If the cell quality factor [1] is lower than 4000, the cell is not masked (still operational), otherwise the cell is masked and its energy is estimated from the neighbours.

Figure E.2 shows the LAr calo cells which are masked unconditionally or conditionally during calibration loop for few ATLAS runs. In the first databased updating, the information of these channels are saved for further usage. An example of noisy cells flagged during bulk processing is give in Figure E.3. The second condition database updates may be needed to keep information for flagged cell during the bulk. Figure E.4 shows the noisy LAr trigger towers flagged by both online software (LAr trigger tower noise killer) and offline tools during calibration loops. The LAr trigger tower noise killer (LTTNK) is the online software used to disable noisy channels in the hot trigger towers published in trigger monitor list. As described in this reference [171], more than 99.9% of the LAr channels were functional during Run2.

[1] The quality factor $Q = \sum_i (s_i - r_i)^2$ measured the level of agreement between the digitized observed sample (s_i) and reference pulse shape (r_i). This quantity is used to discriminate between the signal from real energy deposit and noise.

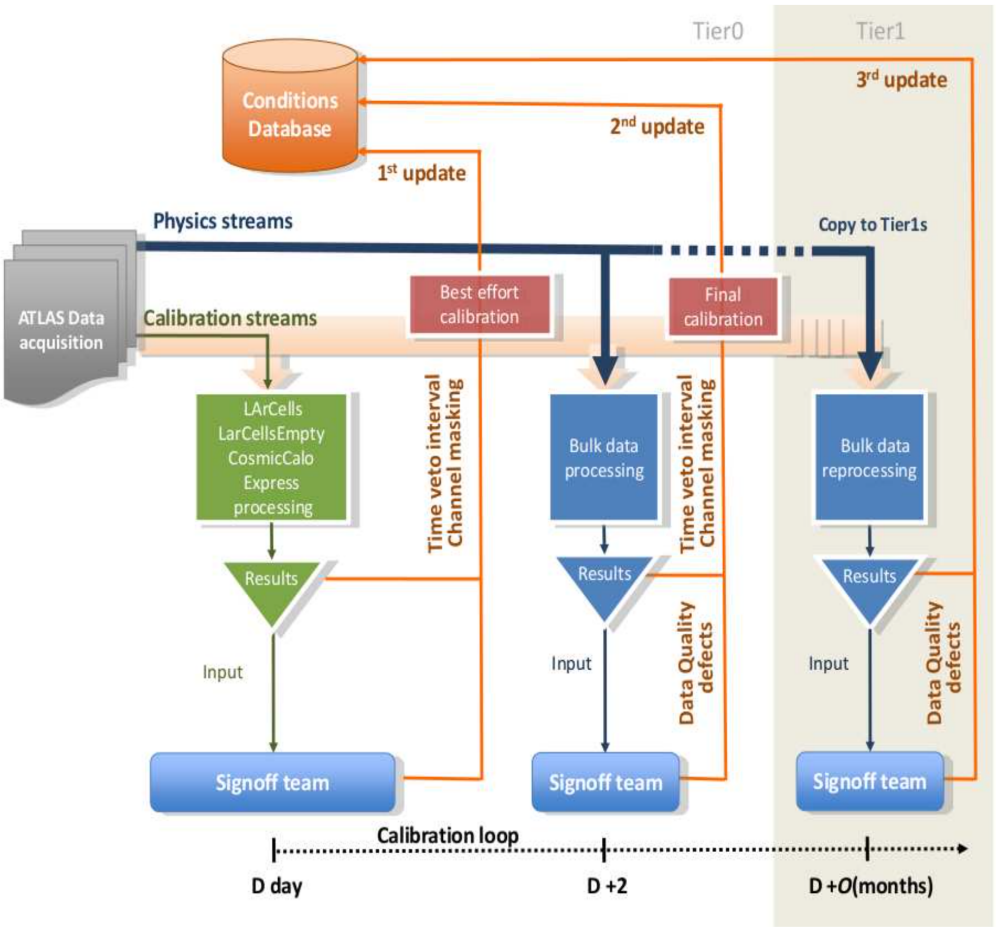

Figure E.1: Graphical view of the ATLAS data monitoring including both the calibration loop and the bulk processing. D corresponds to the starting point in a ATLAS run. Figure from [170].

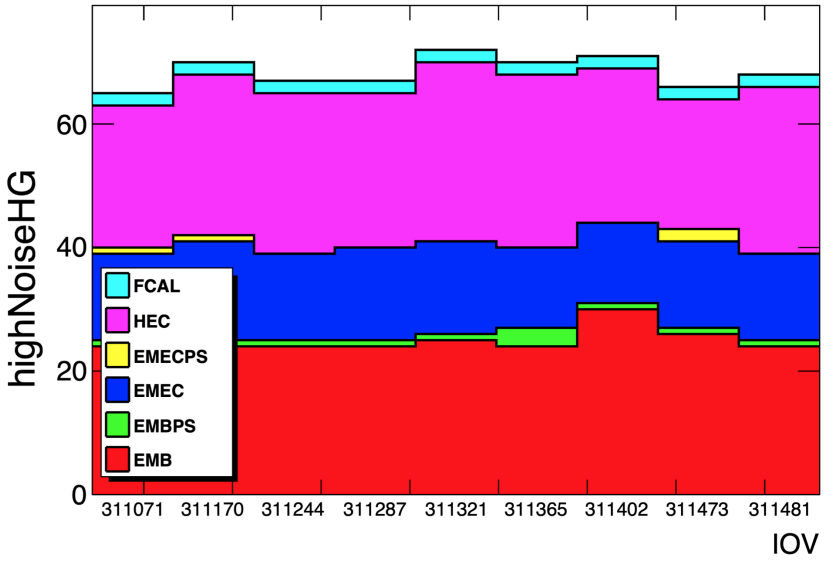

(a)

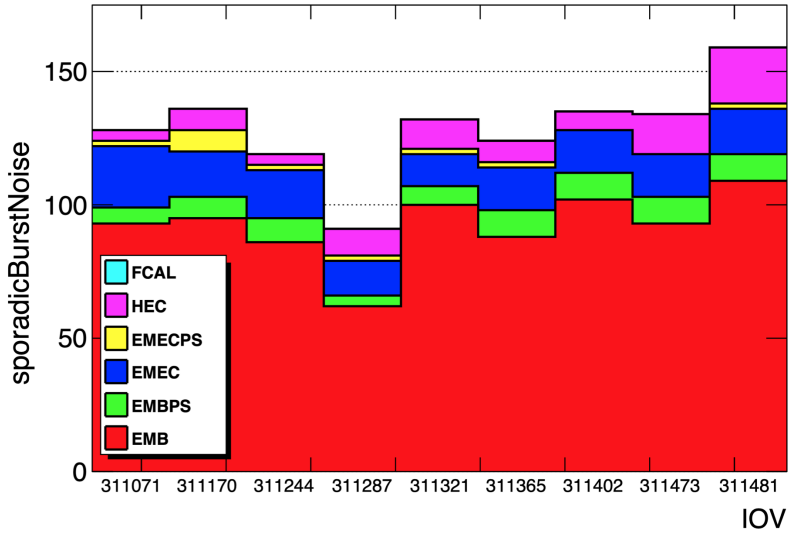

(b)

Figure E.2: A summary of the number of offline unconditional masked (a) and conditional masked channels (b) during calibration loop for several ATLAS runs. The IOV is the interval of validity which, in this context, represents ATLAS data taken during a single LHC fill.

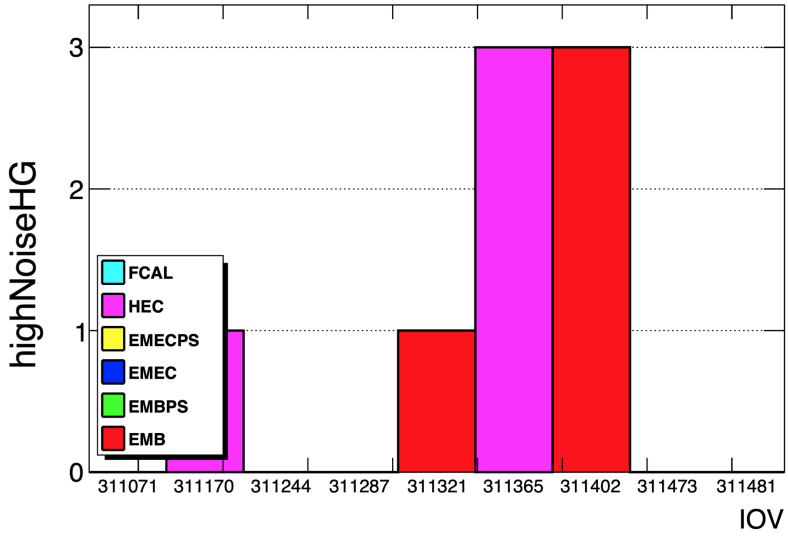

(a)

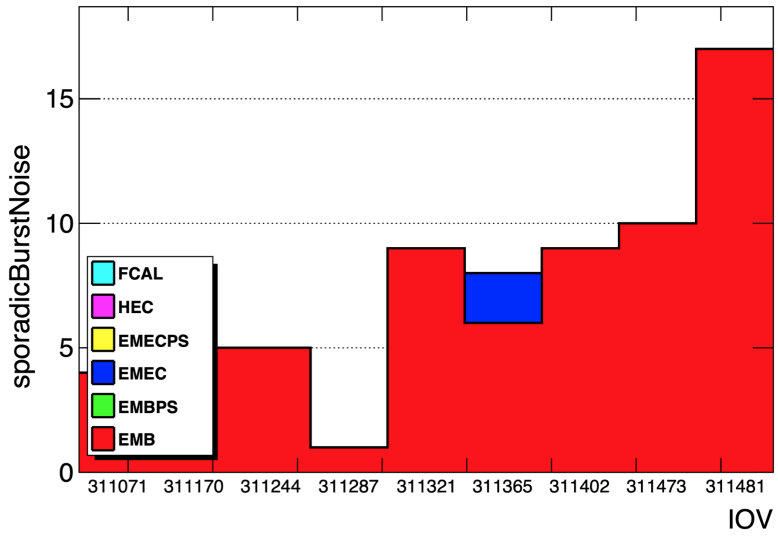

(b)

Figure E.3: A summary of the number of offline unconditional masked (a) and conditional masked channels (b) during the bulk processing for several ATLAS runs. The IOV is the interval of validity which, in this context, represents ATLAS data taken during a single LHC fill.

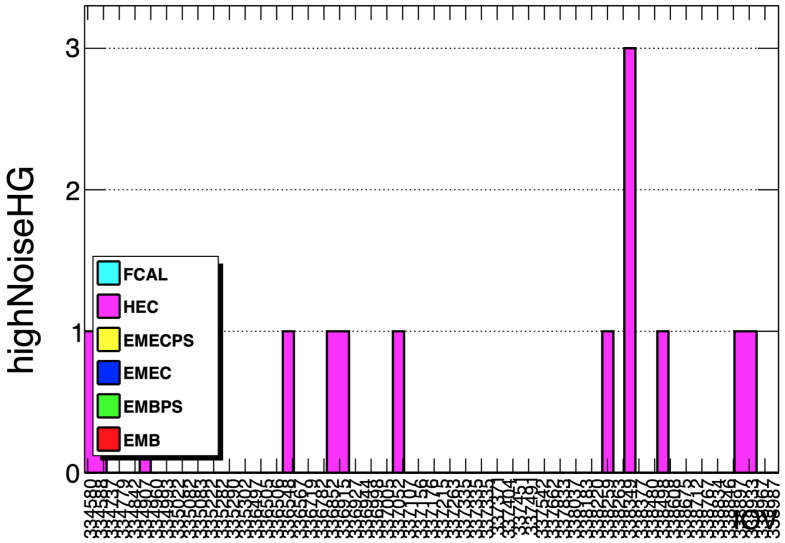

(a)

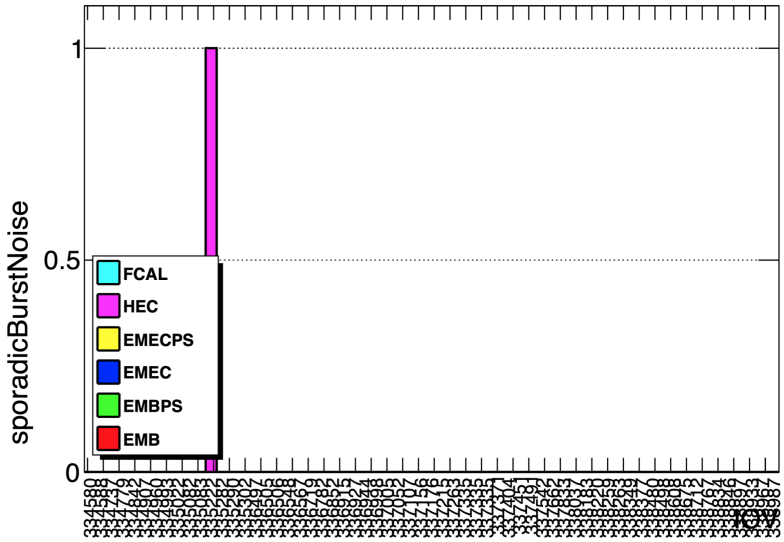

(b)

Figure E.4: A monthly summary of the trigger towers flagged both online and offline during the calibration loop. The x-axis shows the separate LHC fills in September 2017 during which ATLAS data was taken.

Glossary

ATLAS a general purpose detector at the LHC. 32, 38–40, 42–47, 49, 51, 54–60, 64, 65, 68, 71, 73, 79, 80, 85–87, 89–92, 95, 97, 103, 122

BDT boosted decision tree. 86

BSM beyond-Standard Model. 23, 85

CCA Connected component analysis. 74

CERN the European Organization for Nuclear Research. 32–35

CP Cluster processor. 61, 62

CR Control Region. 113–116, 129

CSC Cathode Strip Chambers. 55–57, 89

CST Cluster Soft Term. 92

CTP Central Trigger Processor. 60

DGLAP Dokshitzer-Gribov-Altarelli-Parisi. 66

ECal electromagnetic calorimeter. 39, 40, 48–50, 90, 99

EM Electromagnetic. 52–54, 77, 79, 92, 98

EMB Electromagnetic Barrel. 51, 52

EMEC Electromagnetic End-cap. 51

FCal Forward Calorimeter. 49, 52, 54

GMSB Gauge-mediated SUSY breaking. 25, 30, 31

GRL Good Runs List. 64

GSC Global sequential calibration. 81, 82, 98

GWS Glashow-Weinberg-Salam. 14, 16, 19

HCal Hadronic Calorimeter. 39, 40, 48, 49, 52, 90

HEC Hadronic End-cap. 52–54

HLT High-level Trigger. 60, 61

IBL Insertable B-Layer. 44, 87, 103

ID Inner Detector. 39, 43, 44, 46, 47, 49, 73–76, 87, 88, 90, 91, 99, 100, 124

IP Interaction point. 45, 46, 88

JEP Jet/energy processor. 61–63

JER jet energy resolution. 123, 124

JES jet energy scale. 79–81, 83, 84, 98, 123

JVT jet-vertex-tagger. 98, 99

L1 Level-1. 60, 61

L1A L1 accept. 60

L1Calo Level-1 Calo. 60, 61

L1Muon Level-1 Muon. 60

LAr Liquid-argon. 51, 52, 54, 82, 103

LB luminosity blocks. 64

LEP Large Electron-Positron Collider. 33

LHC Large Hadron Collider, located at CERN. 3, 4, 32–37, 39, 41, 59, 60, 64, 84, 93, 95, 105

Linac2 Linear accelerator. 34, 35

LO Leading order. 68, 96

LSP lightest supersymmetric particle. 28, 30, 91, 101

MC Monte Carlo. 65, 66, 68, 72, 75, 81–83, 93, 96, 105, 111, 113, 122, 129, 130

MDT Monitor Drift Tubes. 55–57, 89

ME Matrix element. 68, 69

MS muon spectrometer. 54, 55, 87, 88, 124

MSSM Minimal Supersymmetric Standard Model. 26–31, 94

MSUGRA minimal supergravity. 30

NLO Next-to-leading order. 96

NP nuisance parameter. 123

OP Operating point. 88–91, 99, 100

PDF Parton distribution function. 65–67

PMSB Planck-scale-mediated SUSY breaking. 29

PMT Photomultiplier Tubes. 53

PS Proton Synchrotron. 34, 35, 96

PSB Proton Synchrotron Booster. 34, 35

PV Primary vertices. 76, 81, 86, 92, 100

QCD Quantum Chromodynamics. 4, 11–14, 67, 69–71

QED Quantum Electrodynamics. 10, 11, 69

RF Radio-frequency. 33, 34

ROI Regions-of-Interest. 61

RPC Resistive Plate Chambers. 55–57, 60

SCT SemiConductor Tracker. 43, 45, 46, 74, 90, 103

SM Standard Model. 3–6, 9, 20–25, 27, 28, 31, 39, 85, 91, 93, 94, 96, 100, 103

SPS Super Proton Synchrotron. 34, 35

SR Signal Region. 113–116, 129, 132

SSB spontaneous symmetry breaking. 17

SUSY Supersymmetry. 4, 23–31, 37, 85, 91, 93, 94, 100, 105

TDAQ Trigger and Data Acquisition. 59–61

TGC Thin Gap Chambers. 55–57, 60

TRT Transition Radiation Tracker. 43, 45–47, 56

TST Track Soft Term. 92, 100

UE underlying event. 67, 96

VEV vacuum expectation value. 17, 29, 31

VR Validation Region. 113, 114, 116

Bibliography

[1] S. Weinberg, *A Model of Leptons*, Phys. Rev. Lett. 19 (1967), 1264.

[2] A. Salam, *Theory of Gauge Unification of Fundamental Forces*, Rev. Mod. Phys. 52 (1980), 525.

[3] S. L. Glashow, *Partial Symmetries of Weak Interactions*, Nucl. Phys. 22 (1961) 579

[4] ATLAS Collaboration, *Observation of a new particle in the search for the Standard Model Higgs boson with the ATLAS detector at the LHC*, Phys. Lett. B (2012), 19.

[5] CMS Collaboration, *Observation of a new boson at a mass of 125 GeV with the CMS experiment at the LHC*, Physics Letters B 716 (2012), 30 – 61.

[6] The Nobel Prize in Physics 2013, Press release.

[7] W.N. Cottingham and D.A. Greenwood, *An Introduction to the Standard Model of Particle Physics (2001).*

[8] D0 Collaboration, *Search for high mass top quark production in pp collisions at* $\sqrt{s}$*=1.8 TeV*, Phys. Rev. Lett. 74 (1995) 2422.

[9] CDF Collaboration, *Observation of Top Quark Production in pp Collisions with the Collider Detector at Fermilab*, Phys. Rev. Lett. 74 (1995) 2626.

[10] I. J. R. Aitchison and A. J. G. Hey, *Gauge theories in particle physics: A practical introduction: From relativistic quantum mechanics to QED*, CRC Press, Bristol, UK, 2012.

[11] P.A. Zyla, *The Review of Particle Physics*, Phys. Rev. D 98, 030001 (2018).

[12] F. Mandl and G. Shaw, *Quantum Field Theory 2nd Edition (2010).*

[13] M. E. Peskin and D. Schroeder , *An Introduction To Quantum Field Theory (1995).*

[14] A. Macfaralane, A. Sudbery, and P. Weisz, *On Gell-Mann's λ-Matrices, d- and f-Tensors, Octets, and Parametrizations of SU/(3),* Commun. math. Phys. 11, 77—90 (1968.

[15] M. Banados and I. Reyes, *A short review on Noether's theorems, gauge symmetries and boundary terms*, arXiv:1601.03616 [hep-th].

[16] A. Salam , *Weak and Electromagnetic Interactions, Conf. Proc. C680519 (1968).*

[17] R. K. Ellis, *QCD and Collider Physics, Cambridge University Press (1996), 9780511628788.*

[18] D. J. Gross and F. Wilczek, *Ultraviolet Behavior of Non-Abelian Gauge Theories*, Phys. Rev. Lett. 30 (1973), 1343.

[19] H. David Politzer, *Reliable Perturbative Results for Strong Interactions*, Phys. Rev. Lett. 30 (1973), 1346

[20] S. Bethke, *World Summary of αs*, arXiv:1210.0325 (2012) [hep-ex].

[21] A. Salam, S. Weinberg and J. Goldstone, *Broken Symmetries*, Phys. Rev. 127 (1962) 965.

[22] P.W.Higgs, *Broken symmetries, massless particles and gauge fields*, Phys. Lett. 12 (1964) 132.

[23] G.F. Giudice, *Naturally Speaking: The Naturalness Criterion and Physics at the LHC*, arXiv:0801.2562 (2008) [hep-ph].

[24] S. P. Martin, *A Supersymmetry primer*, arXiv:hep-ph/9709356 (2016) [hep-ph].

[25] Super-Kamiokande Collaboration, *Evidence for Oscillation of Atmospheric Neutrinos*, Phys. Rev. Lett. 81 (1991), 1562.

[26] C. P. Burgess, *Quantum gravity in everyday life: General relativity as an effective field theory,* arXiv:gr-qc/0311082 (2003).

[27] G. Bertone, D, Hooper, and J. Silk, *Particle dark matter: Evidence, candidates and constraints,* arXiv:hep-ph/0404175 (2004).

[28] D. Clowe, M. Bradac, A. H. Gonzalez, M. Markevitch, S. W. Randall, C. Jones, and D. Zaritsky, *A direct empirical proof of the existence of dark matter,* arXiv:astro-ph/0608407 (2006).

[29] L. Bergstro, *Dark Matter Candidates,* New Journal of Physics 11 (2009).

[30] L. Canetti, M. Drewes, and M. Shaposhnikov, *Matter and Antimatter in the Universe,* New Journal of Physics V.14 (2012).

[31] G. Hooft, *Recent Developments in Gauge Theories,* NATO Sci. Ser. B 59 (1980).

[32] A. Salam and J. A. Strathdee, *Supersymmetry and Nonabelian Gauges*, Phys. Lett. B (1974), 353.

[33] J. Wess and B. Zumino, *Supergauge Transformations in Four-Dimensions,* Nucl. Phys. B 70 (1974) 39.

[34] J. L. GervaisB.Sakita, *Field theory interpretation of supergauges in dual models,* Nucl. Phys. B34 (1971) 632.

[35] B. Howard and T. Xerxes, *Weak scale supersymmetry : from superfields to scattering events,* Cambridge : Cambridge Univ. Press, 2006. - 537 p.

[36] J. Wess and B. Zumino, *A lagrangian model invariant under supergauge transformations,* Phys. Lett. B49 (1974) 52.

[37] S. Ferrara and B. Zumino, *Supergauge invariant Yang-Mills theories,* Nucl. Phys. B 79 (1974), p. 413.

[38] I. J. R Aitchison, *Supersymmetry and the MSSM: An Elementary Introduction,* arXiv:hep-ph/0505105 (2005).

[39] R. N. Mohapatra, *Supersymmetry and R-parity: an Overview,* arXiv:1503.06478 [hep-ph] (2015).

[40] R. Barbieri, S. Ferrara, and C. Savoy, *Gauge models with spontaneously broken local supersymmetry,* Physics Letters B V.119 (1982) 343.

[41] L. Hall, J. Lykken, and S. Weinberg, *Supergravity as the messenger of supersymmetry breaking,* Phys. Rev. D 27, (1983) 2359.

[42] L. ibanez, *The locally supersymmetric SU(5) grand unification,* Phys. Rev. Lett. 49 (1982) 970.

[43] M. Dine and W. Fischler, *A Phenomenological Model of Particle Physics Based on Supersymmetry,* Phys. Lett. B110 (1982) 227.

[44] L. Alvarez-Gaume, M. Claudson, and M. B. Wise, *Low-Energy Supersymmetry,* Nucl. Phys. B 207 (1982) 96.

[45] C. R. Nappi and B. A. Ovrut, *Supersymmetric Extension of the SU(3) × SU(2) × U(1) Model,* Phys. Lett. B 113 (1982) 175.

[46] M. Dine and A. E. Nelson, *Dynamical supersymmetry breaking at low-energies,* arXiv:hep-ph/9303230, Phys. Rev. D48 (1993) 1277–1287.

[47] M. Dine, A. E. Nelson, Y. Nir, and Y. Shirman, *New tools for low-energy dynamical supersymmetry breaking,*
Phys. Rev. D53 2658–2669, arXiv:hep-ph/9507378 (1993).

[48] L. Evans and P. Bryant, *LHC Machine,*
Journal of Instrumentation V.3 (2008).

[49] M, Stephen, *The LEP Collider, from design to approval and commissioning,* CDS record, DOI 10.5170 (1991).

[50] The ATLAS Collaboration, *The ATLAS Experiment at the CERN Large Hadron Collider,* Journal of Instrumentation V.3 (Aug 2008).

[51] The CMS Collaboration, *The CMS experiment at the CERN LHC,* Journal of Instrumentation V.3 (Aug 2008).

[52] The ALICE Collaboration, *The ALICE experiment at the CERN LHC,* Journal of Instrumentation V.3 (Aug 2008).

[53] The LHCB Collaboration, *The LHCb Detector at the LHC,* Journal of Instrumentation V.3 (Aug 2008).

[54] O. S. Brüning, P. Collier, P. Lebrun, S. Myers, R. Ostojic, P. Proudlock, and J. Poole, *LHC Machine,* CERN-2004-003-V-1.

[55] E. A. Mobs, *The CERN accelerator complex,*
CERN, 2016-2020, General Photo.

[56] High Luminosity Large Hadron Collider, *The HL-LHC project,*
https://hilumilhc.web.cern.ch/content/hl-lhc-project.

[57] ATLAS collaboration, *Luminosity determination in pp collisions at $\sqrt{s}$=13 TeV using the ATLAS detector at the LHC,* ATLAS-CONF-2019-021.

[58] Atlas experiment, *Luminosity public results,* https://twiki.cern.ch/twiki/bin/view/AtlasPublic.

[59] J. Pequenao and P. Schaffner, *A computer generated image representing how ATLAS detects particles,* CERN, Jan, 2013, General Photo.

[60] R. Sahoo, *Relativistic Kinematics,* arXiv:1604.02651 [nucl-ex] (2016).

[61] ATLAS Collaboration, *ATLAS inner detector : Technical Design Report, 1,* https://cds.cern.ch/record/331063, CERN-LHCC-199.

[62] ATLAS Collaboration, *ATLAS inner detector : Technical Design Report, 2,* https://cds.cern.ch/record/331064, CERN-LHCC-1997.

[63] ATLAS Collaboration, *ATLAS pixel detector electronics and sensors,* Journal of Instrumentation Vol3, July 2008.

[64] J. N. Jackson, *The ATLAS semiconductor tracker,* Nucl. Instrum. Meth. A.

[65] ATLAS Collaboration, *ATLAS liquid argon calorimeter: Technical design report,* https://cds.cern.ch/record/331061.

[66] ATLAS Collaboration, *ATLAS tile calorimeter: Technical Design Report,* https://cds.cern.ch/record/331062.

[67] C. W. Fabjan and F. Gianotti, *Calorimetry for particle physics,* Rev. Mod. Phys. 75, (2003) 1243.

[68] ATLAS Collaboration, *ATLAS muon spectrometer: Technical design report,* https://cds.cern.ch/record/331068.

[69] A. Yamamotoa, Y.Makidaa, R.Ruberbc, Y.Doia, and T.Haruyama, *The ATLAS central solenoid,* Nucl. Ins in Phys Research Section (2008).

[70] F. Bauer et al, *Construction and test of MDT chambers for the ATLAS muon spectrometer,* Nucl. Ins in Phys Research Section (2001).

[71] T. Argyropoulos, *Cathode strip chambers in ATLAS : Installation, commission- ing and in situ performance,* 2008 IEEE Nuclear Science Symposium Conference Record. Oct. 2008.

[72] G. Aiellia, A.Aloisiob, M.Alviggib, V.Aproduc, and V.Bocci, *The RPC first level muon trigger in the barrel of the ATLAS experiment,* Nuclear Physics B, Vol. 158, August 2006.

[73] S.Majewski, G.Charpak, A.Breskin, and G.Mikenberg, *A thin multiwire chamber operating in the high multiplication mode,* Nucl. Ins in Phys Research Section, Vol. 217, November 1983.

[74] ATLAS Collaboration, *ATLAS Magnetic System,* http://atlas-ma.web.cern.ch/atlas-ma/.

[75] ATLAS Collaboration, *Performance of the ATLAS Trigger System in 2015,* Eur. Phys. J. C 77 (2017) 317.

[76] ATLAS Collaboration, *Performance of the ATLAS Trigger System in 2010,* Phys. J. C 72 (2012) 1849, arXiv:1110.1530 [hep-ex].

[77] ATLAS Collaboration, *ATLAS level-1 trigger: Technical Design Report,* https://cds.cern.ch/record/381429.

[78] ATLAS Collaboration, *ATLAS high-level trigger, data-acquisition and controls: Technical Design Report 2003,* https://cds.cern.ch/record/616089.

[79] Pauly, T, *The ATLAS Level-1 Central Trigger System in Operation,* Journal of Physics: Conference Series, Vol.219, Online Computing.

[80] ATLAS Level-1 Calorimeter Trigger collaboration, *The ATLAS Level-1 Calorimeter Trigger: PreProcessor implementation and performance,* Journal of Instrumentation, Volume 7, December 2012.

[81] E. F. Eisenhandler, *ATLAS Level-1 Calorimeter Trigger Algorithms,* https://cds.cern.ch/record/792528.

[82] ATLAS Collaboration, *ATLAS data quality operations and performance for 2015–2018 data-taking,* arXiv:1911.04632 [physics.ins-det].

[83] ATLAS Collaboration, *Data Quality Monitoring Framework for the ATLAS experiment: Performance achieved with colliding beams at the LHC,* Journal of Physics: Conference Series, Vol. 331.

[84] F. Close, *An Introduction to Quarks and Partons,*, Academic Press, 1979.

[85] J. C. Collins and D. E. Soper, *The Theorems of Perturbative QCD,* Annual Review of Nuclear and Particle Science 37 (1987) 383.

[86] Y. L. Dokshitzer, *Calculation of the Structure Functions for Deep Inelastic Scattering and e+ e- Annihilation by Perturbation Theory in Quantum Chromodynamics,* Sov. Phys. JETP 46 (1977).

[87] V. Gribov and L. Lipatov, *Deep inelastic e p scattering in perturbation theory,* Sov.J.Nucl.Phys. 15 (1972) 438-450, Yad.Fiz. 15 (1972) 781-807 (1972).

[88] G. Altarelli, G. Parisi, *Asymptotic freedom in parton language,* Nuclear Physics B Volume 126, Issue 2, 8 August 1977.

[89] R. P. Feynman, *Very High-Energy Collisions of Hadrons,* Phys. Rev. Lett., 23:1415–1417, 1969.

[90] R. D. Ball et al, *Parton distributions from high-precision collider data,* The European Physical Journal C 77 (2017) 663.

[91] S. Höche, *Introduction to parton-shower event generators,* arXiv:1411.4085 [hep-ph].

[92] J. Alwall et al, *The automated computation of tree-level and next-to-leading order differential cross sections, and their matching to parton shower simulations,* arXiv: 1405.0301 [hep-ph].

[93] J. Alwall, M. Herquet, F. Maltoni, O. Mattelaer, T. Stelzer, *MadGraph 5 : Going Beyond,* arXiv:1106.0522 [hep-ph].

[94] S. Alioli, P. Nason, C. Oleari, Emanuele Re, *A general framework for implementing NLO calculations in shower Monte Carlo programs: the POWHEG BOX,* arXiv:1002.2581 [hep-ph].

[95] T. Gleisberg, S. Hoeche, F. Krauss, M. Schoenherr, S. Schumann, F. Siegert, J. Winter, *Event generation with SHERPA 1.1,* arXiv:0811.4622 [hep-ph].

[96] G. C. Fox, and S. Wolfram, *A model for parton showers in QCD,* Nuclear Physics B Volume 168, Issue 2, 9 June 1980, Pages 285-295.

[97] T. Sjöstrand, S. Ask, J. R. Christiansen, R. Corke, N. Desai, P. Ilten, S. Mrenna, S. Prestel, C. O. Rasmussen, and P. Z. Skands, *An Introduction to PYTHIA 8.2,* arXiv:1410.3012.

[98] T. Sjostrand, S. Mrenna, and P. Z. Skands, *PYTHIA 6.4 Physics and Manual,* arXiv:hep-ph/0603175.

[99] A. Papaefstathiou et al., *Herwig 7.0 / Herwig++ 3.0 Release Note,* arXiv:1512.01178 [hep-ph].

[100] G. Corcella, I. G. Knowles, G. Marchesini, S. Moretti, K. Odagiri, P. Richardson, M. H. Seymour, and B. R. Webber, *HERWIG 6.5: an event generator for Hadron Emission Reactions With Interfering Gluons (including supersymmetric processes)*, arXiv:hep-ph/0011363.

[101] X. Artru and G. Mennessier., *String model and multiproduction*, Nuclear Physics B Volume 70, Issue 1, 18 February 1974, Pages 93-115.

[102] B. Isildak., *Measurement of the differential dijet production cross section in proton-proton collisions at* $\sqrt{s}$ *= 7 TeV*, arXiv:1308.6064 [hep-ex].

[103] GEANT4 Collaboration, S. Agostinelli et al *GEANT4: A Simulation toolkit*, Nucl. Inst. Vol. 506, Issue 3, 1 July 2003.

[104] ATLAS Collaboration, *Early Inner Detector Tracking Performance in the 2015 Data at* $\sqrt{s}$ *= 13 TeV*, https://cds.cern.ch/record/2110140/files.

[105] ATLAS Collaboration, *Performance of the ATLAS Track Reconstruction Algorithms in Dense Environments in LHC Run 2*, arXiv:1704.07983 [hep-ex].

[106] R. E. Kalman, *A New Approach to Linear Filtering and Prediction Problems, Transactions of the ASME*, Journal of Basic Engineering 35 (1960).

[107] R. Fruhwirth, *Application of Kalman filtering to track and vertex fitting*, Nucl. Inst. Vol. 262, Issues 2–3, 15 December 1987.

[108] R. Fruhwirth, W. Waltenberger, and P. Vanlaer, *Adaptive vertex fitting*, Journal of Physics G 34 (2007).

[109] ATLAS Collaboration, *Topological cell clustering in the ATLAS calorimeters and its performance in LHC Run1*, arXiv:1603.02934 [hep-ex].

[110] S. Catani, Yu.L. Dokshitzer, M.H. Seymour, and B.R. Webber, *Longitudinally invariant* K_t *clustering algorithms for hadron hadron collisions*, Nucl.Phys.B 406 (1993) 187-224.

[111] S. D. Ellis, D. E. Soper, *Successive Combination Jet Algorithm For Hadron Collisions*, arXiv:hep-ph/9305266.

[112] Yuri L. Dokshitzer, G. D. Leder, S. Moretti, and B. R. Webber, *Better jet clustering algorithms*, JHEP 08 (1997) 001.

[113] M. Cacciari, G. P. Salam, and G.Soyez, *The anti-kt jet clustering algorithm,* arXiv:0802.1189 [hep-ph], JHEP 0804:063,2008.

[114] M. Cacciari, G. P. Salam, and G.Soyez, *FastJet User Manual,* Eur. Phys. J., C72:1896, 2012.

[115] ATLAS Collaboration, *Jet energy scale measurements and their systematic uncertainties in proton-proton collisions at* $\sqrt{s}$ *= 13 TeV with the ATLAS detector,* Phys. Rev. D 96, 072002 (2017).

[116] M. Cacciari and G. P. Salam, *Pileup subtraction using jet areas,* arXiv:0707.1378 [hep-ph], Phys.Lett.B659:119-126,2008.

[117] ATLAS Collaboration, *Jet energy measurement and its systematic uncertainty in proton–proton collisions at* $\sqrt{s}$ *= 7 TeV with the ATLAS detector* Eur. Phys. J. C 75 (2015).

[118] ATLAS Collaboration, *Performance of jet substructure techniques for large-R jets in proton-proton collisions at* $\sqrt{s}$ *= 7 TeV using the ATLAS detector,* arXiv:1306.4945 [hep-ex], JHEP09 (2013) 076.

[119] D. Krohn, J. Thaler, and L. Wang, *Jet Trimming,* JHEP, 02:084, 2010.

[120] ATLAS Collaboration, *Performance of jet substructure techniques for large-R jets in proton–proton collisions at* $\sqrt{s}$ *= 7 TeV using the ATLAS detector,* arXiv: 1306.4945 [hep-ex], JHEP09 (2013) 076.

[121] ATLAS Collaboration, *Commissioning of the ATLAS high performance b-tagging algorithms in the 7 TeV collision data,* ATLAS-CONF-2011-102, 2011.

[122] G. Piacquadio and C. Weiser, *A new inclusive secondary vertex algorithm for b-jet tagging in ATLAS,* Journal of Physics: Conference Series, Volume 119.

[123] ATLAS Collaboration, *Expected performance of the ATLAS b-tagging algorithms in Run-2,* ATL-PHYS-PUB-2015-022.

[124] ATLAS Collaboration, *Optimisation of the ATLAS b-tagging performance for the 2016 LHC Run,* ATL-PHYS-PUB-2016-012.

[125] ATLAS Collaboration, *Muon reconstruction performance of the ATLAS detector in proton–proton collision data at* $\sqrt{s}$ *=13 TeV,* arXiv:1603.05598 [hep-ex], Eur. Phys. J. C 76 (2016).

[126] ATLAS Collaboration, *Electron efficiency measurements with the ATLAS detector using the 2012 LHC proton–proton collision data,* ATLAS-CONF-2016-024.

[127] ATLAS Collaboration, *Electron and photon energy calibration with the ATLAS detector using LHC Run 1 data,* arXiv:1407.5063 [hep-ex].

[128] ATLAS Collaboration, *Performance of algorithms that reconstruct missing transverse momentum in $\sqrt{s}$ = 8 TeV proton-proton collisions in the ATLAS detector,* arXiv:1609.09324 [hep-ex], Eur. Phys. J. C 77 241 (2017).

[129] ATLAS Collaboration, *Performance of missing transverse momentum reconstruction with the ATLAS detector using proton-proton collisions at $\sqrt{s}$ = 13 TeV,* arXiv:1802.08168 [hep-ex].

[130] ATLAS Collaboration, *Expected performance of missing transverse momentum recon- struction for the ATLAS detector at $\sqrt{s}$ = 13 TeV,* ATL-PHYS-PUB-2015-023.

[131] ATLAS Collaboration, *Search for supersymmetry in final states with missing transverse momentum and multiple b-jets in proton-proton collisions at $\sqrt{s}$ = 13 TeV with the ATLAS detector,* JHEP 06 (2018) 107.

[132] ATLAS Collaboration, *Search for supersymmetry in final states with missing transverse momentum and multiple b-jets in proton-proton collisions at $\sqrt{s}$ = 13 TeV with the ATLAS detector,* ATLAS-CONF-2018-041.

[133] C. Borschensky, M. Kramer, A. Kulesza, M. Mangano, S. Padhi, T. Plehn, X. Portell, *Squark and gluino production cross sections in pp collisions at $\sqrt{(s)}$ = 13, 14, 33 and 100 TeV,* Eur.Phys.J. C74 (2014) 12.

[134] S. van der Meer, *Calibration of the effective beam height in the ISR,* CERN-ISR-PO-68-31. ISR-PO-68-31.

[135] Richard D. Ball et al, *Parton distributions with LHC data,* arXiv:1207.1303 [hep-ph].

[136] ATLAS Collaboration, *The ATLAS Simulation Infrastructure,* arXiv:1005.4568 [physics.ins-det], Eur.Phys.J.C70:823-874,2010.

[137] ATLAS Collaboration, *Tagging and suppression of pileup jets with the ATLAS detector,* ATLAS-CONF-2014-018.

[138] ATLAS Collaboration, *Performance of pile-up mitigation techniques for jets in pp collisions at s = 8 TeV using the ATLAS detector,* arXiv:1510.03823 [hep-ex], Eur. Phys. J. C (2016) 76:581.

[139] ATLAS SUSY Analysis Group, *ATLAS Muon recommended isolation working points,* gitlab.cern.ch/PhysicsAnalysis/SUSYPhys/MuonOP.

[140] ATLAS SUSY Analysis Group, *ATLAS SUSY Analysis Tools,* gitlab.cern.ch/PhysicsAnalysis/SUSYPhys/SUSYTools.

[141] ATLAS Collaboration, *Measurement of multi-jet cross sections at ATLAS,* arXiv:1109.6843 [hep-ex].

[142] ATLAS Collaboration, *Search for pair production of up-type vector-like quarks and for four-top-quark events in final states with multiple b-jets with the ATLAS detector,* arXiv:1803.09678 [hep-ex].

[143] M. Baak, G. J. Besjes, D. Cote, A. Koutsman, J. Lorenz, D. Short, *HistFitter software framework for statistical data analysis,* arXiv:1410.1280 [hep-ex].

[144] ATLAS Collaboration, *Search for supersymmetry in final states with missing transverse momentum and multiple b-jets in proton-proton collisions at $\sqrt{s}$ = 13 TeV with the ATLAS detector,* arXiv:1711.01901 [hep-ex].

[145] ATLAS Collaboration, *Search for supersymmetry in final states with missing transverse momentum and multiple b-jets in proton-proton collisions at $\sqrt{s}$ = 13 TeV with the ATLAS detector,* ATLAS-CONF-2018-041.

[146] ROOT Collaboration, *namespace RooStats::NumberCountingUtils,* https://root.cern.ch/root/RooStatsNumberCountingUtils.html.

[147] L. Moneta, K. Belasco, K. Cranmer, A. Lazzaro, D. Piparo, G. Schott, W. Verkerke, M. Wolf, K. Belasco, K. Cranmer, A. Lazzaro, D. Piparo, G. Schott, W. Verkerke, and M. Wolf, *The RooStats Project,* arXiv:1009.1003 [physics.data-an].

[148] ATLAS Collaboration, *Jet energy measurement and its systematic uncertainty in proton–proton collisions at $\sqrt{s}$ = 7 TeV with the ATLAS detector,* Eur. Phys. J. C 75 (2015) 17, arXiv: 1406.0076 [hep-ex].

[149] ATLAS Collaboration, *Determination of the jet energy scale and resolution at ATLAS using Z/γ-jet events in data at* $\sqrt{s}$ *= 8 TeV*, cds, 15 Oct 2015.50.

[150] ATLAS Collaboration, *Measurement of the muon reconstruction performance of the ATLAS detector using 2011 and 2012 LHC proton-proton collision data*, Eur.Phys.J. C74 (2014) 3130, arXiv:1407.3935 [hep-ex].

[151] LUCID Collaboration, *LUCID: The ATLAS Luminosity Detector*, PoS ICHEP2018 (2019) 280.

[152] ATLAS Collaboration, *Luminosity determination in pp collisions at* $\sqrt{s}$ *= 8 TeV using the ATLAS detector at the LHC*, Eur. Phys. J. C 76 (2016) 653, arXiv:1608.03953 [hep-ex].

[153] ATLAS Collaboration, *Expected performance of missing transverse momentum reconstruction for the ATLAS detector at* $\sqrt{s}$ *= 13 TeV*, ATL-PHYS-PUB-2015-023.

[154] ATLAS Collaboration, *SUSY Theoretical Uncertainties options*, https://twiki.cern.ch/twiki/bin/viewauth/SUSYTheoreticalUncertainties.

[155] ATLAS Collaboration, *Measurements of fiducial cross-sections for* $t\bar{t}$ *production with one or two additional b-jets in pp collisions at* $\sqrt{s}$ *= 8 TeV using the ATLAS detector*, Eur. Phys. J. C (2016) 76:11, arXiv:1508.06868 [hep-ex].

[156] P. Kant, O.M. Kind, T. Kintscher, T. Lohse, T. Martini, S. Mölbitz, P. Rieck, P. Uwer, *HATHOR for single top-quark production: Updated predictions and uncertainty estimates for single top-quark production in hadronic collisions*, Comput.Phys.Commun. 191 (2015) 74-89, arXiv:1406.4403 [hep-ph].

[157] ATLAS Collaboration, *BTagging Truth Tagging Tool*, https://twiki.cern.ch/twiki/bin/viewauth/BtaggingTRFandRW.

[158] A. L. Read, *Presentation of search results: the* CL_s *technique*, Journal of Physics G: Nuclear and Particle Physics, Vol. 28, (2002).

[159] W. Verkerke, D. Kirkby, *RooFit Users Manual v2.91*, https://root.cern.ch/RooFit_Users_Manual_2.91-33.pdf.

[160] ROOT Collaboration, K. Cranmer et al, *HistFactory: A tool for creating statistical models for use with RooFit and RooStats,* CERN-OPEN-2012-016, https://cds.cern.ch/record/1456844.

[161] F. James, *Statistical Methods in Experimental Physics,* World Scientific, 2nd ed. 2006.

[162] J. Aldrich, *R.A. Fisher and the making of maximum likelihood 1912-1922,* Statist. Sci. 12 (1997) 162.

[163] ATLAS Statistics Forum, *The CL_s method: information for conference speakers,* https://twiki.cern.ch/twiki/NotesOnStatistics/CLsInfo.pdf.

[164] E, Gross, *LHC Statistics for Pedestrians,* https://cds.cern.ch/record/1099994/files/p205.pdf.

[165] ATLAS Statistics Forum, *Frequentist Limit Recommendation,* https://indico.cern.ch/event/126652/Frequentist_Limit.pdf.

[166] J. Neyman and E. S. Pearson, *On the Problem of the Most Efficient Tests of Statistical Hypotheses,* Philosophical Transactions of the Royal Society of London. Series A, Containing Papers of a Mathematical or Physical Character Vol. 231 (1933), https://www.jstor.org/stable/91247.

[167] K. Cranmer, E. Gross, G. Cowan, O. Vitells, *Asymptotic formulae for likelihood-based tests of new physics,* arXiv:1007.1727 [physics.data-an], Eur. Phys. J. C 73, 2501 (2013).

[168] The CMS Collaboration, *Summary plots from the CMS Supersymmetry physics group,* https://twiki.cern.ch/twiki/CMSPublic/PhysicsResults.

[169] The ATLAS Collaboration, *Summary plots from the ATLAS Supersymmetry physics group,* https://atlas.web.cern.ch/Atlas/ATL-PHYS-PUB-2020-020/.

[170] The ATLAS Collaboration, *Monitoring and data quality assessment of the ATLAS liquid argon calorimeter,* Journal of Instrumentation, Vol. 9, July 2014.

[171] The ATLAS Collaboration, *ATLAS data quality operations and performance for 2015-2018 data-taking,* arXiv:1911.04632 [physics.ins-det].